U. PORTO

DOUTORAMENTO

BIOLOGIA MOLECULAR E CELULAR

Functional analysis of novel cargo adaptors for the microtubule motor cytoplasmic dynein-1

Vanessa Alves Teixeira

D
2025

U. PORTO

Vanessa Alves Teixeira. Functional analysis of novel cargo adaptors for the microtubule motor cytoplasmic dynein-1

D.ICBAS **2025**

Functional analysis of novel cargo adaptors for the microtubule motor cytoplasmic dynein-1

Vanessa Alves Teixeira

INSTITUTO DE CIÊNCIAS BIOMÉDICAS ABEL SALAZAR
FACULDADE DE CIÊNCIAS

VANESSA MARIA ALVES TEIXEIRA

Functional analysis of novel cargo adaptors for the microtubule motor cytoplasmic dynein-1

Tese de Candidatura ao grau de Doutor em Biologia Molecular e Celular;

Programa Doutoral da Universidade do Porto (Instituto de Ciências Biomédicas Abel Salazar e Faculdade de Ciências da Universidade do Porto)

Orientador – Doutor Reto Gassmann

Categoria – Investigador Principal

Afiliação – i3S – Instituto de Investigação e Inovação em Saúde; IBMC - Instituto de Biologia Molecular e Celular, Universidade do Porto.

Coorientador – Doutor Tiago Jorge Oliveira Gonçalves de Almeida Dantas

Categoria – Investigador Auxiliar

Afiliação – i3S – Instituto de Investigação e Inovação em Saúde; IBMC - Instituto de Biologia Molecular e Celular, Universidade do Porto.

Coorientador – Doutor Ricardo dos Santos Celestino

Categoria – Investigador Auxiliar

Afiliação – i3S – Instituto de Investigação e Inovação em Saúde; IBMC - Instituto de Biologia Molecular e Celular, Universidade do Porto.

The PhD program and institutions involved in the development of this thesis work are:

IBMC – Instituto de Biologia Molecular e Celular

i3S – Instituto de Investigação e Inovação em Saúde, Universidade do Porto

Cell Division Mechanisms Group

Rua Alfredo Allen, 208

4200-135 Porto, Portugal

www.i3s.up.pt

Funding Institutions

Funding to develop this work was provided by European Research Council under the European Union's Seventh Framework Programme (FP7/2007-2013)/ERC grant agreement no. ERC-2013-StG-338410-DYNEINOME, and by National Funds through FCT – Fundação para a Ciência e a Tecnologia/Ministério da Ciência, Tecnologia e Ensino Superior (PTDC/BIA-CEL/1321/2021 and CEECIND/00333/2017 to Reto Gassmann; and CEECIND/00771/2017 to Tiago Dantas). Vanessa Teixeira was supported by a PhD Fellowship provided by FCT, co-financed by FSE – Fundo Social Europeu, through the Norte Portugal Regional Operational Programme (SFRH/BD/147283/2019). Support from tuition fees was also provided by the academic institution ICBAS – Instituto de Ciências Biomédicas Abel Salazar da Universidade do Porto.

Declaração de Honra

Declaro que a presente tese é de minha autoria e não foi utilizada previamente noutro curso ou unidade curricular, desta ou de outra instituição. As referências a outros autores (afirmações, ideias, pensamentos) respeitam escrupulosamente as regras da atribuição e encontram-se devidamente indicadas no texto e nas referências bibliográficas, de acordo com as normas de referenciação. Tenho consciência de que a prática de plágio e autoplágio constitui um ilícito académico.

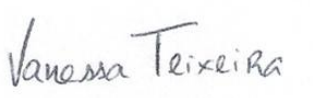

Porto, Maio de 2025

“As a scientist, you imagine something nobody tried before, otherwise you wouldn’t be a scientist, and you just imagine things that maybe are doable, and keep trying. And when it fails, you have already come up with many, many other solutions. But as a scientist, there is always a lot of failure, and you have to be a champion of failure.”

Katalin Karikó, UZH News, 2024

ACKNOWLEDGMENTS/AGRADECIMENTOS

The work behind this PhD thesis would not have been possible without the collaboration and support of many people, to whom I express my most sincere gratitude. If I forgot to mention anyone, please know that I am equally grateful for your support.

I want to thank my supervisor, Reto Gassmann, for welcoming me into his lab and giving me the opportunity to pursue a PhD. I was lucky to be guided by a true scientist, and it was a privilege to learn alongside someone with such exceptional scientific knowledge and curiosity for the subject. I am grateful for his creative ideas, understanding, and the confidence he placed in me throughout this journey.

I want to thank my co-supervisors, Tiago Dantas and Ricardo Celestino, for all the extra push, ideas, advice, and support throughout these years.

A special thank you to Daniel Barbosa, who was not officially my supervisor, but could easily have been. Thank you for guiding me since my first day in the lab and always believe in me. He is a true example of both an outstanding scientist and a remarkable person.

I am grateful to all i3S members who, in one way or another, contributed and helped me during this time.

Thanks to all current and former members of Cell Division Mechanisms and Cytoskeleton Dynamics groups who crossed my path. I would like to thank Ana X. Carvalho for all the ideas and support. I am grateful to Helder Rocha, Elaine (Fung-Yi Chan), Marta Silva, Matilde Moreira, Artur Rodrigues, Mafalda Cautela, Daniel Osório, Vanessa Ferreira, Mariana Sousa, Filipa Sobral, Inês Santos, Joana Leite, and Felix Kapler for all the help in the lab, the advice, the conversations, and the fun. They made the daily rush feel lighter. A special thank you to Bernardo Gama for introducing me to the world of biochemistry.

To the members of the Dantas Lab: Carla Abreu, Diogo Rodrigues, Ana Castro, Maria João Castro, and Tiago Ribeiro, I am thankful for their support, enthusiasm and joy.

Thanks to Beatriz Dias for her friendship and inspiring example. The days in the lab were never the same without her. Thank you for being someone who bravely pursues her dreams and for showing me that even long-distance friendships can endure.

Thanks to Cátia Carvalho, who was my rock in the lab. I was truly lucky to share this journey with such an amazing person. Thank you for always knowing the rules and deadlines, for keeping me on track, and for all the lighthearted and meaningful conversations. My coffee was definitely less bitter with you. Thanks, Cátia!

Quero agradecer à Ana Rita Ferreira, talvez a minha amiga mais antiga, por todas as vezes em que me perguntava o que eu estudava, pelas longas conversas depois dos ensaios da banda. que me ajudavam a desligar dos desafios de ser estudante de doutoramento, e por todo o apoio e amizade ao longo destes anos.

Agradeço à minha Família por me ter apoiado em todas as minhas escolhas, por me ter ensinado a querer ser melhor, por desculpar o meu mau humor e por sempre estar presente. Muito obrigada!

Finalmente, agradeço ao Carlos Vieira. Obrigada pelas vezes em que me foste buscar a horas tardias ao i3S, em que foste contar células comigo ao fim-de-semana, em que me ouviste reclamar nos momentos menos bons, em que me abriste os olhos para os momentos bons, em que me deste a força que eu não tinha. Obrigada pela compreensão e entrega que tornam a minha vida mais fácil. Obrigada, Carlos, por teres feito este Caminho comigo e continuares a caminhar a meu lado!

Thank you all! Obrigada a todos!

LIST OF PUBLICATIONS/LISTA DE PUBLICAÇÕES

The present doctoral thesis is a compilation of research data, part of which has already been published in an international peer-reviewed journal. The author declares an active role in the conception and execution of the experiments that led to the published work, as well as in the analysis, interpretation, discussion of the data, and in the preparation of the manuscript.

The following published article has been included in this thesis:

Vanessa Teixeira, Kashish Singh, José Gama, Matilde Moreira, Ricardo Celestino, Ana Xavier Carvalho, Paulo Pereira, Carla Abreu, Tiago Dantas, Andrew Carter, and Reto Gassmann. (2025). CDR2 is a dynein adaptor recruited by kinectin to regulate ER sheets organization. *Journal of Cell Biology, 224*(9). https://doi.org/10.1083/jcb.202411034.

A presente tese de doutoramento é uma compilação de resultados de investigação, parte dos quais já se encontra publicada numa revista internacional indexada. O autor declara ter tido uma participação ativa na conceção e execução dos trabalhos que deram origem à publicação referida, bem como na análise, interpretação, discussão dos resultados e preparação do manuscrito.

Faz parte integrante desta tese o seguinte artigo já publicado:

Vanessa Teixeira, Kashish Singh, José Gama, Matilde Moreira, Ricardo Celestino, Ana Xavier Carvalho, Paulo Pereira, Carla Abreu, Tiago Dantas, Andrew Carter, and Reto Gassmann. (2025). CDR2 is a dynein adaptor recruited by kinectin to regulate ER sheets organization. *Journal of Cell Biology, 224*(9). https://doi.org/10.1083/jcb.202411034.

ABSTRACT

Cytoplasmic dynein-1 (dynein) is the primary minus end-directed microtubule motor responsible for transporting a wide range of cargos, from small proteins to large organelles. For motility, dynein requires the cofactor dynactin and cargo-specific adaptors that assemble the active transport complex. However, the full repertoire of dynein adaptors and their mechanisms of action remain incompletely understood.

The endoplasmic reticulum (ER) plays numerous vital roles within the cell, including protein synthesis, folding and secretion. It is a highly dynamic organelle that extends throughout the cytoplasm, forming an interconnected network of tubules and sheets. ER morphology is continually remodeled in response to various intracellular and environmental signals, emphasizing the close link between ER organization and function. Its structure is tightly regulated by the cytoskeleton, particularly by microtubule-based motors such as dynein and kinesin-1.

In this work, Cerebellar degeneration-related protein 2 (CDR2) and its paralog CDR2-like (CDR2L) were identified as novel dynein adaptors on the ER. Although known as onconeural antigens associated with paraneoplastic cerebellar degeneration (PCD), the cellular functions of CDR2 and CDR2L have remained poorly characterized. Both proteins contain sequence motifs characteristic of known dynein adaptors, including a predicted CC1 box motif. Biochemical assays, demonstrated that CDR2 and CDR2L directly bind dynein and dynactin in a CC1 box-dependent manner. Furthermore, CDR2L is able to activate dynein motility *in vitro*.

To identify potential dynein cargos mediated by CDR2 and CDR2L, immunoprecipitations were performed using extracts from human cancer cells stably expressing GFP::3xFLAG-tagged CDR2 or CDR2L in a CDR2/L double knockout (KO) background. Quantitative mass spectrometry identified kinectin (KTN1), an ER sheet component, as the most enriched interactor for both proteins. Co-localization between CDR2 and KTN1 was confirmed by immunofluorescence, and the respective interaction domains were mapped.

CDR2/L double KO cells exhibit increased ER sheet stacking, as observed by transmission electron microscopy. Loss of CDR2/L was found to enhance KTN1-dependent ER sheet stacking, which is reversed by exogenous CDR2 in a CC1 box-dependent manner. CDR2 expression additionally promotes ER sheet clustering near centrosomes.

CDR2 was shown to compete with the eEF1Bβ subunit of translation elongation factor-1B (eEF1B) for KTN1 binding, and knockdown of eEF1Bβ increases endogenous CDR2 levels on ER sheets, inducing their centrosome-proximal clustering.

In summary, this work identifies two new dynein adaptors and describes a novel dynein-dependent pathway for ER sheet organization, with potential implications for the pathogenesis of PCD.

Keywords: dynein, CDR2, CDR2L, endoplasmic reticulum, KTN1, p180, eEF1Bβ, paraneoplastic cerebellar degeneration.

RESUMO

A dineína citoplasmática 1 (dineína) é o principal motor que se move na direção da extremidade negativa dos microtúbulos, responsável pelo transporte de diversos tipos de cargas, desde pequenas proteínas até organelos de grandes dimensões. De forma a ter motilidade, a dineína depende do cofator dinactina e de adaptadores específicos de carga. No entanto, o repertório de adaptadores da dineína e os respetivos mecanismos de ação ainda não são completamente compreendidos.

O retículo endoplasmático (RE) desempenha múltiplas funções essenciais na célula, incluindo a síntese e o processamento de proteínas. Trata-se de um organelo altamente dinâmico que se estende por todo o citoplasma, formando uma rede contínua de túbulos e cisternas. A morfologia do RE é continuamente remodelada em resposta a diversos sinais intracelulares e externos, refletindo a estreita relação entre a sua organização e função. A sua estrutura é fortemente regulada pelo citoesqueleto, nomeadamente por motores dependentes de microtúbulos, como a dineína e a cinesina-1.

Neste trabalho, a Proteína associada à degeneração cerebelar 2 (CDR2) e a sua paráloga CDR2-*like* (CDR2L) foram identificadas como novos adaptadores da dineína no RE. Embora sejam conhecidos como antigénios onconeuronais associados à degeneração cerebelar paraneoplásica, as funções das proteínas CDR2 e CDR2L permanecem pouco esclarecidas. Ambas as proteínas contêm na sua sequência motivos característicos dos adaptadores conhecidos da dineína, incluindo um motivo CC1 *box*. Ensaios bioquímicos demonstraram que CDR2 e CDR2L se ligam diretamente à dineína e à dinactina de forma dependente do seu motivo CC1 *box*. Adicionalmente, CDR2L é capaz de ativar a motilidade da dineína *in vitro*.

De forma a identificar possíveis cargas transportadas pela dineína mediadas por CDR2 e CDR2L, foram realizadas imunoprecipitações a partir de extratos de células humanas cancerígenas a expressar de forma estável CDR2 ou CDR2L marcadas com GFP::3xFLAG, no contexto de dupla deleção (KO) de CDR2/L. Espectrometria de massa quantitativa identificou a kinectina (KTN1), um componente das cisternas do RE, como a proteína associada mais enriquecida para ambas as proteínas. A co-localização entre CDR2 e KTN1 foi confirmada por ensaios de imunofluorescência, e os respetivos domínios de interação foram mapeados.

As células duplo KO para CDR2/L apresentam um aumento na sobreposição de cisternas do RE, conforme observado por microscopia eletrónica de transmissão. Foi mostrado que a perda de CDR2/L potencia a sobreposição das cisternas do RE de forma dependente da KTN1, um efeito revertido pela expressão exógena de CDR2 de forma

dependente do seu motivo CC1 *box*. A expressão de CDR2 também promove a acumulação das cisternas do RE na proximidade dos centrossomas.

Foi mostrado ainda que CDR2 compete com a subunidade eEF1Bβ do fator de elongação de tradução-1B (eEF1B) pela ligação à KTN1, e a depleção de eEF1Bβ aumenta os níveis endógenos de CDR2 nas cisternas do RE, induzindo a sua acumulação perto dos centrossomas.

Em suma, este trabalho identifica dois novos adaptadores da dineína e descreve uma nova via dependente da dineína para a organização das cisternas do RE, com potenciais implicações para a patogénese da degeneração cerebelar paraneoplásica.

Palavras-chave: dineína, CDR2, CDR2L, retículo endoplasmático, KTN1, p180, eEF1Bβ, degeneração cerebelar paraneoplásica.

TABLE OF CONTENTS

ABSTRACT ..... **I**

RESUMO ..... **III**

TABLE OF CONTENTS ..... **V**

LIST OF FIGURES ..... **IX**

LIST OF TABLES ..... **XI**

LIST OF SYMBOLS AND ABBREVIATIONS ..... **XIII**

THESIS OUTLINE ..... **XVII**

CHAPTER I. GENERAL INTRODUCTION **1**

1 THE MICROTUBULE CYTOSKELETON **3**

1.1 Microtubules 3

1.2 Microtubule-associated proteins 4

2 THE DYNEIN MOTOR COMPLEX **6**

2.1 Cytoplasmic dynein-1 composition and structure 6

2.2 Mechanochemical cycle 7

2.3 Dynein autoinhibition and regulation by dynactin 8

2.4 Activating cargo adaptors 11

3 ENDOPLASMIC RETICULUM **16**

3.1 ER morphology and function 16

3.2 ER shaping and remodeling 18

3.2.1 Formation of ER tubules 18

3.2.2 Formation of ER sheets 19

3.3 Regulation of ER dynamics by the microtubule cytoskeleton 21

3.3.1 Regulation of ER dynamics by microtubule motors 22

3.4 Protein translation and the role of translation elongation factor-1 25

4 CEREBELLAR DEGENERATION-RELATED PROTEINS **27**

4.1 Paraneoplastic cerebellar degeneration 27

4.2 CDR2 and CDR2L: molecular characteristics and subcellular localization 27

4.3 CDR2 and CDR2L: Potential functions 29

4.3.1 Gene expression and regulation 29

4.3.2 Calcium homeostasis 31

4.3.3 mRNA Transport 32

CHAPTER II. AIMS **35**

1 Dissection of the dynein-dynactin-CDR2/CDR2L transport machine 37

2 Identification of dynein cargo transported by CDR2/CDR2L 37
3 Address the functional role of CDR2/CDR2L in cells 37
CHAPTER III. MATERIALS AND METHODS 39
DNA constructs 41
General cloning 41
Protein expression 45
Protein purification 45
GST pull-downs 47
Strep-Tag II pull-downs from porcine brain lysate 48
Size exclusion chromatography to assess protein complex formation 49
Production of CDR2 and CDR2L antibodies 49
Cell culture 52
Lentivirus production 52
CRISPR/Cas9-mediated genome editing and transgenic cell lines 53
PCR-based validation of genome editing 53
Cell cycle profile 54
Time-lapse live-cell microscopy 55
Transient expression 55
RNA interference 56
Immunofluorescence 56
Immunoblotting 57
Immunoprecipitation and mass spectrometry 58
Transmission electron microscopy 59
Correlative light–electron microscopy 59
Structure prediction 60
Cell cycle synchronization 60
Graphs and statistical analysis 61
In vitro TIRF motility assays 61
CHAPTER IV. RESULTS 63
CDR2 and CDR2L are novel adaptors for cytoplasmic dynein-1 65
CDR2 and CDR2L interact and co-localize with the integral ER membrane protein KTN1 67
A C-terminal helix in CDR2 is necessary and sufficient for binding to KTN1 and recruitment to ER sheets 68
Double KO of CDR2 and CDR2L promotes organization of ER sheets into stacks 70

CDR2 overexpression results in CC1 box-dependent clustering of ER sheets near centrosomes....72
Overexpression of KTN1 lacking CDR2 binding site mimics the CDR2/L double KO phenotype in U2OS cells....73
CDR2 competes with eEF1Bβ, but not KIF5C, for binding to KTN1....74
eEF1Bβ knockdown enhances recruitment of endogenous CDR2 to ER sheets and promotes ER sheet clustering near centrosomes....76
CDR2/L KO cells show normal proliferation rates....78
CHAPTER V. DISCUSSION....81
CDR2 and CDR2L as new dynein adaptors....83
CDR2 and ER sheets: a role mediated by KTN1....86
CDR2 competes with eEF1Bβ for KTN1 binding....88
CDR2 and CDR2L in neuronal cells and PCD....90
CHAPTER VI. CONCLUDING REMARKS AND PERSPECTIVES....93
CHAPTER VII. LIST OF REFERENCES....97
CHAPTER VIII. SUPPLEMENTARY MATERIAL....121

LIST OF FIGURES

Figure 1 – Structural organization of dynein. 7

Figure 2 – Structural organization of dynactin. 9

Figure 3 – Assembly of the dynein-dynactin-adaptor complex. 11

Figure 4 – Morphology of the ER 17

Figure 5 – Determinants for ER shaping and remodeling. 20

Figure 6 – Regulation of ER dynamics by ER-microtubule interactions. 22

Figure 7 – CDR2 and CDR2L are novel adaptors for cytoplasmic dynein-1. 66

Figure 8 – CDR2 and CDR2L interact and co-localize with the integral ER membrane protein KTN1. 69

Figure 9 – CDR2 regulates the organization of ER sheets. 71

Figure 10 – KTN1 lacking CDR2 binding site mimics CDR2/L double KO phenotype in U2OS cells. 73

Figure 11 – CDR2 competes with eEF1Bβ for binding to KTN1 and localization to ER sheets. 75

Figure 12 – eEF1Bβ knockdown enhances CDR2 recruitment to ER sheets and promotes ER sheet clustering near centrosomes. 77

Figure 13 – CDR2/L double KO cells show normal proliferation rates. 79

Figure S1 – Related to Figure 7 (CDR2's interaction with dynein). 123

Figure S2 – Related to Figure 8 (generation of KO cell lines, CDR2L localization, sequence alignments of CDR2/CDR2L's C-terminal helix and its binding site in KTN1/p180, and decreased stability of CDR2 after KTN1 knockdown). 125

Figure S3 – Related to Figure 9 (characterization of ER organization in CDR2/L double KO cells). 127

Figure S4 – Related to Figures 11 and 12 (eEF1Bβ's interaction with KTN1). 129

Figure S5 – Full-length CDR2 and CDR2L constructs are less efficient at pulling down DHC, and CDR2/L are more highly expressed in mitosis (related to *Discussion* section). 130

LIST OF TABLES

Table 1 – Dynein complex activating and candidate adaptors with respective DLIC binding domains and cargos.....14

Table 2 – CDR2 and CEN potential functions and interactors reported in literature. 33

Table 3 – Plasmids constructed and used in the course of this work. 44

Table 4 – List of proteins expressed and purified in the course of this work.....47

Table 5 – sgRNAs used to generate CDR2 and CDR2L single and double KO cell lines.53

Table 6 – Combination of primers used to screen CDR2/L single and double KO cell lines. 54

Table S1 – Dynein, dynactin, and kinesin-1 subunits co-purifying with CDR2(1–146)::StTgII from pig brain lysates (Related to *Discussion* section). 131

Table S2 – Most enriched proteins in immunoprecipitations from cells expressing GFP::3xFLAG::CDR2 or GFP::3xFLAG::CDR2L, identified by mass spectrometry in two experimental replicates (related to *Discussion* section).....132

LIST OF SYMBOLS AND ABBREVIATIONS

%	Percentage
µL, mL, L	Microliter, mililiter, liter
AC	Affinity chromatography
ADP	Adenosine diphosphate
AOS	Anaphase onset
APC/C	Anaphase-promoting complex/cyclosome
APH	Amphipathic helix
ARP1	Actin-related protein 1
ATP	Adenosine triphosphate
BICD2	Protein bicaudal D homolog 2
bp	Base pair
BSA	Bovine serum albumin
CAP-Gly	Cytoskeleton-associated proteins, Glycine rich domain
CB	Calbindin D28K
CC	Coiled-coil
cDNA	Complementary deoxyribonucleic acid
CDR2	Cerebellar degeneration related protein 2
CDR2L	Cerebellar degeneration related protein 2-like
CEN	Centrocortin
CLIMP63	Cytoskeletal linker of the endoplasmic reticulum membrane 63-kDa
CNN	Centrosomin
cOTSC	Cerebellar organotypic slice cultures
CRACR2	Calcium release-activated calcium regulator 2
CRISPR	Clustered regularly interspaced short palindromic repeats
Cryo-EM	Cryogenic electron microscopy
DDA	Dynein-dynactin-adaptor
DHC	Dynein heavy chain
DIC	Dynein intermediate chain
DLC	Dynein light chain
DLIC	Dynein light intermediate chain
DMEM	Dulbecco's modified eagle medium
DMSO	Dimethyl sulfoxide
DNA	Deoxyribonucleic acid
DNAJB14	DNAJ homolog subfamily B
dNTP	Deoxynucleotide triphosphate
dTAC	Depolymerizing tip attachment complex
DTT	Dithiothreitol
EB	End-binding
ECL	Enhanced chemiluminescence

EDTA	Ethylenediaminetetraacetic acid
eEF	Eukaryotic elongation factor
eEF1Bβ	Subunit β elongation factor-1B
eIF4A3	Eukaryotic initiation factor 4A-III
EM	Electron microscopy
ER	Endoplasmic reticulum
FHF	FTS/Hook/FHIP complex
FHIP	FHF complex subunit HOOK-interacting protein
FMRP	Fragile-X mental retardation protein
FSC-A	Forward scatter area
FSC-H	Forward scatter high
FXS	Fragile X syndrome
GAPDH	Glyceraldehyde-3-phosphate dehydrogenase
gDNA	Genomic deoxyribonucleic acid
GDP	Guanosine-5’-diphosphate
GEF	Guanine nucleotide exchange factor
GST	Glutathione S-transferase
GTA	Glutaraldehyde
GTP	Guanosine-5’-triphosphate
HAP1	Huntingtin-associated protein 1
HBS1	Heavy chain binding domain
HEPES	4-(2-hydroxyethyl)-1-piperazineethanesulfonic acid
HIF	Hypoxia-inducible factor
HRP	Horseradish peroxidase
ICD	Intercoiled domain
Ig	Immunoglobulin
IPTG	Isopropyl β-D-1-thiogalactopyranoside
IRB	Isothermal reaction buffer
JIP	JNK-interacting protein
kb	Kilobase
kDa, MDa	Kilodalton, megadalton
KIF5	Kinesin heavy chain
KO	Knockout
KTN1	Kinectin
L7/Pcp-2	Purkinje cell-specific protein-2
LB	Lysogenic broth
LC-MS	Liquid chromatography-mass spectrometry
LFQ	Label-free quantification
LIS1	Lissencephaly 1
LZ	Leucine zipper
MAP	Microtubule associated protein

MBP	Maltose-binding protein
ME	Nuclear envelope
MORF4	Mortality factor 4
MRG	Mortality factor 4-related gene
MRG15	Mortality factor 4-like protein 1
MRGX	Mortality factor 4-like protein 2
mRNA	Messenger ribonucleic acid
ms, s, min, h	Milisecond, second, minute, hour
MT	Microtubule
MTBD	Microtubule-binding domain
MTOC	Microtubule organizing center
NAD	Nicotinamide adenine dinucleotide
NDD	N-terminal dimerization domain
Nde1	Nuclear distribution protein nudE homolog 1
Ndel1	Nuclear distribution protein nudE-like 1
NEBD	Nuclear envelope breakdown
ng, µg, mg	Nanogram, microgram, miligram
NIN	Ninein
NINL	Ninein-Like
nm, µm, mm	Nanometer, micrometer, milimeter
NuMA	Nuclear mitotic apparatus protein
ºC	Degree Celsius
Opti-MEM	Optimized minimal essential medium
PBS	Phosphate-buffered saline
PCD	Paraneoplastic cerebellar degeneration
PCM	Pericentriolar material
PCR	Polymerase chain reaction
PD	Pull-down
PEG	Polyethylene Glycol
PFA	Paraformaldehyde
PHD1	Prolyl hydroxylase domain-containing protein 1
PIPES	Piperazine-N,N′-bis(2-ethanesulfonic acid)
pmol, nmol	Picomol, nanomol
PMSF	Phenylmethanesulfonyl fluoride
pRCC	Papillary renal cell carcinoma
pTAC	polymerizing tip attachment complex
Rab11-FIP3	Rab11 family-interacting protein 3
Ran	Ras-like nuclear G protein
Ras	Rat sarcoma small GTPase
Rb	Retinoblastoma protein
rcf	Relative centrifugal force

REEP	Receptor expression-enhancing protein
RHD	Reticulon-homology domain
RILP	Rab-interacting lysosomal protein
RNA	Ribonucleic acid
RNAi	Ribonucleic acid interference
RNP	Ribonucleiprotein
ROS	Reactive oxygen species
RpS6	Small ribosomal subunit protein eS6
RRBBP1 / p180	Ribosome-binding protein 1 homolog 180-kDa
Rtn	Reticulon
SD	Standard deviation
SDS-PAGE	Sodium dodecyl sulfate – polyacrylamide gel electrophoresis
sgRNA	Single guide ribonucleic acid
SigmaR1	Sigma-1 receptor
siRNA	Small interference ribonucleic acid
SOC	Super optimal broth with catabolite repression
S-pt	S-peptide sequence
SSC-A	Side scatter area
STIM1	Stromal interaction molecule 1
StTgII	Strep-tag II
TAE	Tris-Acetate-EDTA
TBS	Tris-buffered saline
TIRF	Total internal reflection fluorescence
TMH	Transmembrane hairpins
TMR	Tetramethylrhodamine
TRAK	Trafficking kinesin-binding protein
TRIS	Tris(hydroxymethyl)aminomethane
tRNA	Transfer ribonucleic acid
U	Unit
UTR	Untranslated region
UV	Ultraviolet
v	Volume
VGCC	Voltage-gated calcium channel
vs.	versus
w	Weight
α	Alpha
β	Beta
γ	Gama
γ-TuRC	Gama-tubulin ring complex
δ	Delta

THESIS OUTLINE

Dynein plays a key role in organelle positioning and is responsible for the majority of retrograde transport of RNA-protein complexes and organelles within cells. Dynein's diverse functions rely on precise regulation by cofactors and cargo adaptors. This thesis reveals two novel dynein adaptors involved in the organization of ER sheets. The thesis is composed of eight chapters:

CHAPTER I. GENERAL INTRODUCTION: provides an overview of the main topics of this study: (1) the microtubule cytoskeleton; (2) the dynein-1 motor complex and its regulators; (3) the ER, including the mechanisms regulating its morphology; and (4) CDR2 and CDR2L and their proposed cellular roles.

CHAPTER II. AIMS: outlines the objectives of the thesis.

CHAPTER III. MATERIALS AND METHODS: describes all experimental methods used throughout the thesis.

CHAPTER IV. RESULTS: presents both unpublished and published results identifying CDR2 and CDR2L as novel dynein cargo adaptors. These adaptors are capable of recruiting dynein to the ER through the ER-sheet protein KTN1, playing a crucial role in the organization of ER sheets. The chapter also contains unpublished data regarding the characterization of CDR2/L double KO HeLa cell lines.

CHAPTER V. DISCUSSION: presents the interpretation of the results in the context of current knowledge, discusses their biological significance, and proposes experiments to address unresolved questions.

CHAPTER VI. CONCLUSIONS AND FUTURE PERSPECTIVES: summarizes the key findings and scientific contributions of the thesis and proposes future directions for research.

CHAPTER VII. LIST OF REFERENCES: contains all references cited in the thesis.

CHAPTER VIII. SUPPLEMENTARY MATERIAL: presents additional figures and tables that support the data shown in *Chapter IV* and discussion in *Chapter V*, providing further detail and context to the main findings.

CHAPTER I.

GENERAL INTRODUCTION

GENERAL INTRODUCTION

1 THE MICROTUBULE CYTOSKELETON

The cytoskeleton is an intricate and dynamic network of protein filaments that extends throughout the cytoplasm of the cells. This filamentous network provides mechanical support for cells to maintain their overall integrity and perform their functions. Together with actin and intermediate filaments, microtubules constitute the three main classes of cytoskeleton filaments in eukaryotic cells (Pollard & Goldman, 2018). Microtubules play a crucial role in a variety of cellular functions, including providing structural support for the cell, assembly of mitotic spindle and, alongside with actin filaments, they work as tracks for intracellular transport and organelle movement (Barlan & Gelfand, 2017; Pollard & Goldman, 2018).

1.1 Microtubules

Microtubules are composed of α- and β-tubulin heterodimers, which assemble into hollow cylindrical structures with approximately 25 nanometers (nm) in diameter. Each microtubule typically consists of 13 laterally associated protofilaments (Goodson & Jonasson, 2018). Since α-/β-tubulin heterodimers are intrinsically asymmetric, microtubules are polarized structures with two distinct ends: slowly dynamic minus ends with α-tubulin monomer being exposed and highly dynamic plus ends with exposed β-tubulin monomer that grow and shrink through a process designated as dynamic instability (Goodson & Jonasson, 2018).

Dynamic instability is the process by which microtubules undergo successive and stochastic cycles of assembly (rescue) and disassembly (catastrophe). Tubulin monomers have similar structures and both bind guanosine triphosphate (GTP), however only the β-tubulin monomer hydrolyzes its GTP to guanosine diphosphate (GDP) during microtubule polymerization. This hydrolysis induces a conformational change that destabilizes the microtubule lattice, driving the characteristic dynamic behavior of microtubules (Goodson & Jonasson, 2018; Pollard & Goldman, 2018). Under conditions that favor polymerization, it is thought that a cap of GTP tubulin is maintained at the growing plus end tip stabilizing the microtubule (Goodson & Jonasson, 2018). Microtubules are nucleated from a structure known as the γ-tubulin ring complex (γTuRC), which specifically interacts with the microtubule minus end through its γ-tubulin subunits. The γTuRC functions as both a template for microtubule assembly and a stabilizing cap for the microtubule minus end (Goodson & Jonasson, 2018; Thawani & Petry, 2021). This nucleation machinery is found in specialized locations called microtubule organizing centers (MTOCs), which include

structures such as centrosomes, the Golgi apparatus, chromatin and pre-existing microtubules (Thawani & Petry, 2021). In radially organized cells, the microtubule cytoskeleton extends outward from the perinuclear MTOC, where the minus ends of microtubules are embedded, and the plus ends are directed toward the cell periphery (Goodson & Jonasson, 2018; Pollard & Goldman, 2018; Thawani & Petry, 2021). Although this radial microtubule organization is common, the distribution of the microtubule cytoskeleton can vary depending on the cell type (Goodson & Jonasson, 2018). *In vitro*, microtubules can nucleate spontaneously from high concentrations of α-/β-tubulin subunits, though this process is highly energy-consuming and rarely occurs in cells (Thawani & Petry, 2021).

1.2 Microtubule-associated proteins

Microtubule-associated proteins (MAPs) are, by definition, proteins that bind to microtubules and co-purify with tubulin *in vitro* (Goodson & Jonasson, 2018). MAPs fulfil diverse roles within the microtubule network and can be grouped based on their function—such as stabilizing, destabilizing, capping, bundling, or acting as molecular motors—or by their position on the microtubule, whether they bind along the lattice or at the ends (Goodson & Jonasson, 2018).

One major category of MAPs includes motor proteins. These nanomachines use adenosine triphosphate (ATP) hydrolysis to drive movement along microtubule tracks and transport a variety of cellular cargos, ranging from small membranous vesicles to large organelles. There are two major classes of microtubule-associated motors: kinesins and dyneins (Sweeney & Holzbaur, 2018).

Kinesins are a large and diverse superfamily of microtubule-based motors with up to 45 members in humans (Miki *et al.*, 2001; Sweeney & Holzbaur, 2018). These motors are evolutionary conserved and are characterized by their anterograde movement, *i.e.*, toward the plus end of microtubules (with exception of the kinesin-14 family that moves in the opposite way) (Endow *et al.*, 2010; Reck-Peterson *et al.*, 2018; Sweeney & Holzbaur, 2018). Kinesins possess two distinct functional domains: a conserved motor domain (also known as ‘head’) which hydrolysis ATP and generates force and motility on microtubules, and a divergent tail domain that facilitates oligomerization and cargo recognition. With a relatively small and conserved head fused to a diverse array of tail domains, kinesins are able to bind to various types of cargo. Despite the significant sequence similarity found among motor domains, not every kinesin acts as a molecular motor. For instance, kinesin-13 specifically targets the plus ends of microtubules, where it acts to destabilize or depolymerize them (Endow *et al.*, 2010; Sweeney & Holzbaur, 2018). This model of structural and functional

diversification contrasts with that of the second major group of microtubule motors – dyneins.

2 THE DYNEIN MOTOR COMPLEX

Originally identified in 1963 as an ATPase in *Tetrahymena pyriformis* cilia (Gibbons, 1963), dynein was named by Gibbons and Rowe after the unit of force, the dyne (*dyne*, force; *-in*, protein) (Gibbons & Rowe, 1965). This ATPase was an axonemal-specific dynein whose function is to power the motion of motile cilia and flagella (now known as axonemal dynein). A cytoplasmic form of dynein was later isolated from bovine brain by Paschal and colleagues in 1987, when they identified MAP1C as a microtubule-activated ATPase capable of driving intracellular transport towards the minus ends of microtubules (Paschal *et al.*, 1987). Subsequently two cytoplasmic dynein isoforms were designated: cytoplasmic dynein-1, executing numerous roles in cells, and cytoplasmic dynein-2 which specifically transports cargo inside cilia and flagella. The human genome comprises 16 different dynein heavy chain genes, 14 of which encode axonemal dyneins and two of which encode for cytoplasmic dyneins (Roberts, 2018; Roberts *et al.*, 2013). Cytoplasmic dyneins are present in nearly all eukaryotes, except for red algae, flowering plants, and anaerobic parasites of the genus *Entamoeba* (Wickstead & Gull, 2007).

2.1 Cytoplasmic dynein-1 composition and structure

Human cytoplasmic dynein-1 (hereafter referred to as “dynein”) is a 1.4 megadalton (MDa) complex composed of six different subunits, all present in two copies (dimers): dynein heavy chain (DHC), intermediate chain (DIC), light intermediate chain (DLIC), and light chains (DLC: LC7 or Roadblock (Robl), LC8 and Tctex) (Reck-Peterson *et al.*, 2018). DHC is the largest polypeptide (~500 kilodaltons (kDa)) and contains two functional regions: an N-terminal tail and a C-terminal motor domain. The N-terminal tail contains an initial dimerization domain (NDD) followed by a long stretch holding nine helical bundles, with the last bundle joining the motor domain. The tail is required for dimerization and binds the DIC and DLIC subunits. The motor domain generates movement and consists of a helical linker followed by a ring of six AAA+ domains responsible for ATP hydrolysis. The motor binds to the microtubule track through a small globular microtubule-binding domain (MTBD) located at the end of an anti-parallel coiled-coil stalk (Figure 1) (Cianfrocco *et al.*, 2015; Reck-Peterson *et al.*, 2018).

The DIC contains a WD40 domain which folds into a β-propeller that interacts with DHC helical bundles. The extended N-termini of DIC dimers are held together by dimers of DLC (Reck-Peterson *et al.*, 2018). DLC help stabilize the complex and may play a role in regulating specific dynein functions (Figure 1) (Olenick & Holzbaur, 2019; Reck-Peterson *et al.*, 2018).

DLIC is structurally divided into two parts: a conserved Ras-like domain that contacts DHC helical bundles and a C-terminal region which comprises a conserved helix responsible to bind dynein adaptors, and that in some cases may also directly interact with cargo (Figure 1) (Celestino *et al.*, 2019; Lee *et al.*, 2018; Reck-Peterson *et al.*, 2018).

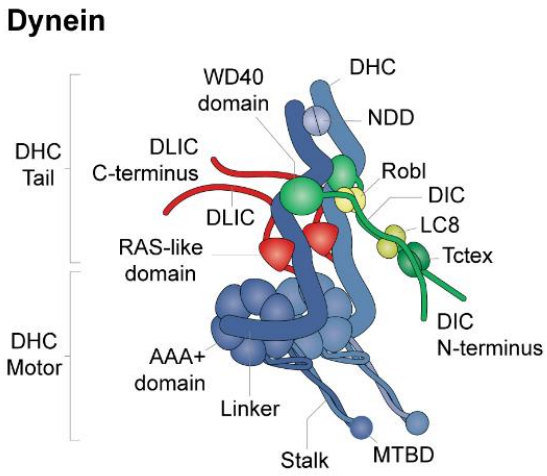

Figure 1 – Structural organization of dynein.

Dynein is composed of two DHCs, which dimerize via an N-terminal dimerization domain (NDD). Each DHC contains a C-terminal motor domain that includes a MTBD at the end of a long antiparallel coiled-coil stalk. DICs have extended N-termini that interact with dimers of DLC (Robl, LC8, and Tctex). DLIC contains an extended C-terminus. Adapted from Reck-Peterson *et al.*, 2018.

2.2 Mechanochemical cycle

The motor domain in DHC contains an AAA+ ring composed of six ATPase domains that convert chemical energy (ATP) into mechanical work. The main site for ATP hydrolysis is the AAA1, although AAA3 and AAA4 are also able to hydrolyse ATP. There is evidence suggesting that dynein only hydrolysis one ATP per step, implying that AAA3 and AAA4 do not hydrolyse ATP in each round of the mechanochemical cycle (Cianfrocco *et al.*, 2015). AAA2, as well as AAA5 and AAA6, lack ATP hydrolysis activity. However, AAA5 and AAA6 play a structural role by transmitting conformational shifts through the AAA+ ring. AAA4 includes a stalk, with a globular tip that has microtubule-binding affinity, allowing dynein to attach to and detach from microtubules. Finally, the linker domain connects the motor and tail domains, facilitating conformational changes and motility in response to the nucleotide state of AAA1 (Cianfrocco *et al.*, 2015).

In summary, dynein binds to microtubules when ATP is absent. ATP binding at AAA1 reduces this affinity, detaching dynein from the microtubule track, as the linker coupled to AAA4 bends into a pre-power conformation. Dynein then rebinds further along the

microtubule toward the minus end. Subsequent phosphate release at AAA1 triggers the power stroke, straightening the linker and pulling the tail forward, along with the other dynein's head and attached cargo. All these conformational changes linked to nucleotide hydrolysis are referred to as dynein's mechanochemical cycle (Cianfrocco *et al.*, 2015).

2.3 Dynein autoinhibition and regulation by dynactin

Dynein is regulated by multiple mechanisms to ensure the motor is fully activated at the right time and place in the cell. Dynein's affinity to microtubules, its capacity for processive movement, and its ability to bind cargos are all modulated by dynein-binding proteins (Cianfrocco *et al.*, 2015; Garrott *et al.*, 2022). In cells, dynein commonly moves at speeds between 0.5 and 2 micrometers/second (µm/s) (Roberts, 2018). However, when isolated, purified mammalian dynein is only weakly processive (Trokter *et al.*, 2012) and requires additional factors to support sustained movement along microtubules (McKenney *et al.*, 2014; Schlager *et al.*, 2014). These include the multi-subunit dynactin complex and any of various cargo adaptor proteins, which mediate the interaction between dynein, dynactin, and cargo, resulting in the formation of a motile dynein-dynactin-adaptor (DDA) complex (Reck-Peterson *et al.*, 2018).

Dynactin was initially identified as an activator of dynein's long-range minus end-directed transport of vesicles along microtubules *in vitro*. This functional role inspired its name, which stands for "dynein activator" (Gill *et al.*, 1991; Schroer & Sheetz, 1991). Dynactin is a 1.1 MDa complex composed of 23 subunits (11 different polypeptides) (Figure 2) (Reck-Peterson *et al.*, 2018). The complex is built around an actin-like filament which contains eight copies of the actin-related protein 1 (ARP1) and one copy of β-actin. The filament has a barbed end and a pointed end, each capped by different protein complexes. The barbed end is capped by the actin capping protein heterodimer CapZαβ and the pointed end by another actin-related protein, Arp11. Three other proteins complement the pointed end, p62, p27 and p25, which bind to Arp11 (Figure 2) (Canty & Yildiz, 2020; Reck-Peterson *et al.*, 2018). The pointed end is central for binding dynein-dynactin to cargo adaptors (Gama *et al.*, 2017; Lau *et al.*, 2021; Yeh *et al.*, 2012). On top of the ARP1 filament, near the barbed end, sits a large bundle of α-helices named the shoulder. It is composed by four copies of p50/dynamitin, two copies of p24, and two copies of $p150^{Glued}$ (p150; Figure 2). The p150 corresponds to dynactin's largest subunit and its N-terminus forms a long and flexible extension (Schroer, 2004). At the very N-terminus of p150 are two microtubule binding domains: the basic domain and the CAP-Gly domain, the latter of which is responsible for recruiting dynactin to microtubules (Figure 2) (Carter *et al.*, 2016; Reck-Peterson *et al.*, 2018). The elongated extension comprises two stretches of coiled coil (CC1 and CC2)

interrupted by a globular intercoiled domain (ICD). The CC1 contains two subdomains, CC1A and CC1B, which form a hairpin structure (Figure 2) (Reck-Peterson *et al.*, 2018).

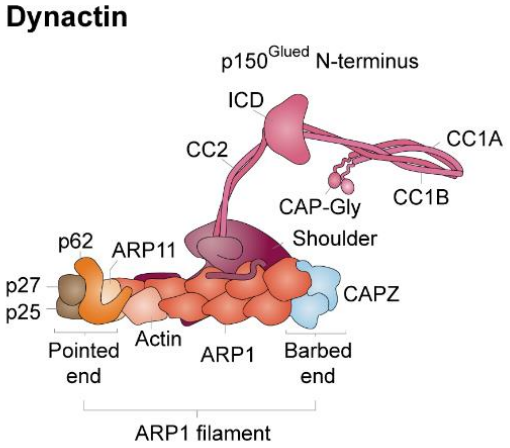

Figure 2 – Structural organization of dynactin.

Dynactin is built around a filament of eight ARP1 proteins. The barbed end of the filament is capped by CAPZ proteins. At the pointed end is an actin monomer, an ARP11 protein and a complex of three proteins (p62, p27, and p25). The shoulder domain binds the filament via extended N-terminal peptides of p50 dynamitin. Extending from the shoulder is the $p150^{Glued}$ subunit, which contains coiled-coil regions (CC2, CC1B, CC1A). At its N-terminus, $p150^{Glued}$ harbors the basic and CAP-Gly domains that interact with microtubules. Adapted from Reck-Peterson *et al.*, 2018.

In cells, dynein dimers are thought to exist primarily in an autoinhibited conformational state (called the phi-particle or phi-dynein, due to its resemblance to the Greek letter Φ), which results from the self-dimerization of DHCs (Amos, 1989; Zhang *et al.*, 2017). This conformational state decreases dynein's affinity for microtubules and restricts its ability to interact with dynactin and adaptor proteins (Zhang *et al.*, 2017). Dynactin can also adopt an autoinhibited conformation in which the CC1A and CC1B of the p150 subunit fold back on each other and dock against the dynactin pointed end complex (Carter *et al.*, 2016). When dynactin adopts this folded-back conformation, the positioning of the p150 arm against the pointed end physically obstructs adaptor proteins from engaging with dynactin. (Lau *et al.*, 2021).

Research in live cells connected lissencephaly-1 protein (LIS1), the nuclear distribution protein nudE homolog 1 (Nde1), and its paralog Nde-like 1 (Ndel1) to the dynein pathway, demonstrating their roles in regulating dynein's activity (Canty & Yildiz, 2020; Garrott *et al.*, 2022; Markus *et al.*, 2020). The prevailing model of dynein regulation by LIS1 suggests that LIS1 stabilizes the motor's open conformation by binding directly to AAA3 of DHC, thereby promoting DDA complex assembly and motility (Markus *et al.*, 2020; Singh *et al.*, 2024).

Nevertheless, LIS1 is still able to promote DDA assembly in a dynein mutant with a constitutively open conformation (Elshenawy *et al.*, 2020; Htet *et al.*, 2020; Singh *et al.*, 2024). At the molecular level there is evidence that Nde1/Ndel1 bind LIS1 and dynein simultaneously and coordinate dynein-LIS1 interaction (Markus *et al.*, 2020). However, the exact mechanism by which they regulate dynein's function remains controversial. Recent work has shown that LIS1 is not able to bind Nde1/Ndel1 and dynein at the same time, suggesting that Nde1/Ndel1 may have a role tethering LIS1 to dynein (Okada *et al.*, 2023).

Recently, Singh and colleagues resolved the cryogenic electron microscopy (cryo-EM) structure of DDA and LIS1 complex bound to microtubules, uncovering novel interaction sites among its components (Singh *et al.*, 2024). According to their model, dynactin autoinhibition is relieved when DIC binds to CC2. This interaction allows LIS1, which is associated with dynein, to engage with the CC1B domain of p150. Through its simultaneous interaction with both dynein and p150, LIS1 facilitates the docking of p150 along DHC engaging both the dynein tail and motor domains (Figure 3). Moreover, LIS1 stabilizes the association between dynein and p150, preventing the p150 arm from reverting to its folded, autoinhibited conformation (Singh *et al.*, 2024). As a result, dynein becomes positioned beneath the p150 arm with its tail next to the dynactin filament, restricting the spatial freedom of both dynein and dynactin and priming the complex for efficient activation by a cargo adaptor protein (Figure 3) (Singh *et al.*, 2024).

In the presence of an activating adaptor, the dynein tail directly binds to dynactin's ARP1 filament, with the two dynein tails positioned in adjacent grooves between ARP1 subunits (Carter *et al.*, 2016; Urnavicius *et al.*, 2015). This interaction stabilizes the dynein tails in a parallel configuration, which in turn aligns their motor domains, allowing both MTBDs to engage microtubules simultaneously (Carter *et al.*, 2016; Urnavicius *et al.*, 2015; Zhang *et al.*, 2017).

In summary, transforming dynein into an ultra-processive motor—capable of traveling several micrometers (µm) along microtubules before detaching (Fellows *et al.*, 2024)—requires multiple layers of regulation. These include the release of dynein from its autoinhibited conformation and the formation of a stable interaction with dynactin, processes that depend on LIS1 and the presence of an activating adaptor (McKenney *et al.*, 2014; Reck-Peterson *et al.*, 2018; Singh *et al.*, 2024; Urnavicius *et al.*, 2015).

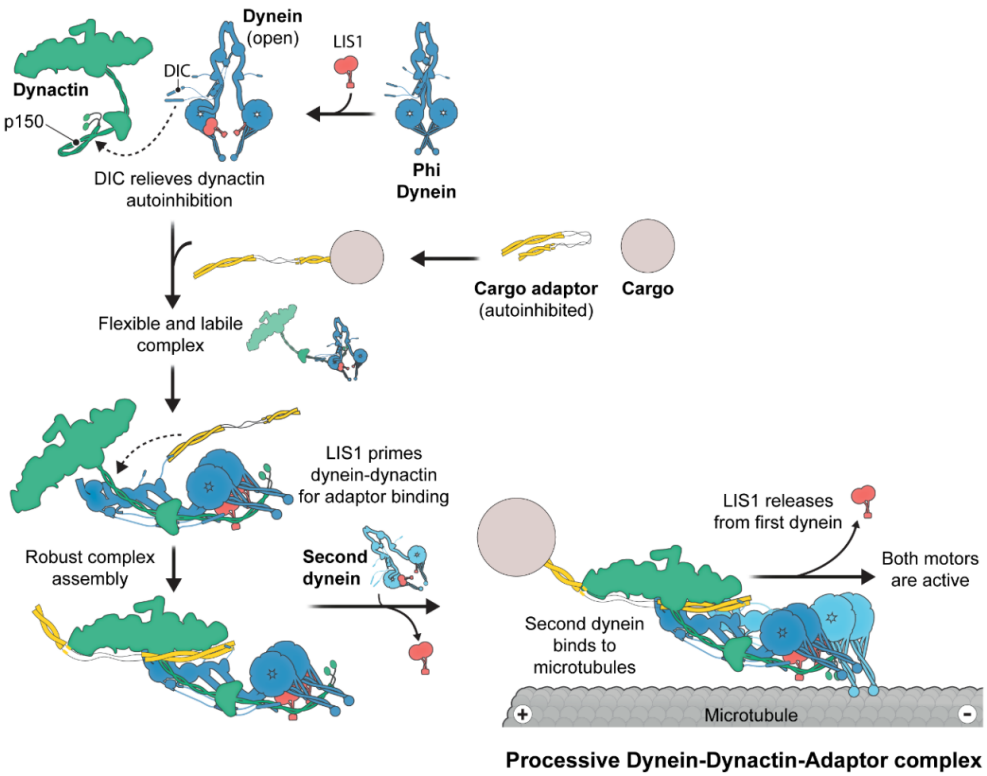

Figure 3 – Assembly of the dynein-dynactin-adaptor complex.

Isolated dynein adopts an autoinhibited Phi conformation, which is relieved by LIS1. DIC binds to p150, releasing dynactin autoinhibition. This enables LIS1-bound dynein to interact with p150, priming dynein-dynactin for adaptor binding. Adaptor can also adopt an autoinhibited conformation that can be relieved by cargo binding. In the assembled complex, LIS1 prevents dynein-A from engaging with microtubules, while a second dynein is recruited to the complex and binds to microtubules. Upon initiation of movement, LIS1 disengages from dynein-A, leading to a fully processive DDA complex. Adapted from Singh *et al.*, 2024 and Yildiz & Zhao, 2023.

2.4 Activating cargo adaptors

Dynactin has been reported to enhance dynein processivity on its own (Ayloo *et al.*, 2014; Cianfrocco *et al.*, 2015; Kardon *et al.*, 2009; King & Schroer, 2000; Ross *et al.*, 2006; Tripathy *et al.*, 2014). However, studies have demonstrated that the combined presence of dynactin and an activating cargo adaptor transforms mammalian dynein from a diffusive into a highly processive motor *in vitro* (Cianfrocco *et al.*, 2015; McKenney *et al.*, 2014; Schlager *et al.*, 2014).

Dynein activating adaptors share a common structural organization, with a long, dimeric N-terminal coiled-coil (>200 residues) that stabilizes dynein-dynactin complex through defined interactions conserved among different adaptors. In opposition, the divergent C-terminal regions of adaptors link the transport machinery to specific cargo (Olenick & Holzbaur, 2019; Reck-Peterson *et al.*, 2018). In all identified activating adaptors, the N-

terminus interacts with a conserved C-terminal helix in DLIC, playing a crucial role in dynein motility *in vitro* and dynein functions in cells (Celestino *et al.*, 2019; Lee *et al.*, 2018; Schroeder & Vale, 2016).

To date, four distinct classes of DLIC-binding motifs have been characterized in activating cargo adaptors: the CC1 box, Hook domain, EF-hand motif, and RH1 domain (Table 1) (Celestino *et al.*, 2022; Lee *et al.*, 2020; Reck-Peterson *et al.*, 2018; Singh *et al.*, 2024).

The CC1 box, present in adaptors such as Protein bicaudal D homolog 2 (BICD2) and Spindly, is a conserved coiled-coil motif defined by an AAxxG sequence, where “x” denotes any amino acid (Table 1) (Gama *et al.*, 2017; Reck-Peterson *et al.*, 2018). Mutation of two conserved alanine residues to valine residues within the CC1-box motif was shown to impair the interaction between adaptor and dynein-dynactin (Gama *et al.*, 2017; Olenick & Holzbaur, 2019; Schlager Serra-Marques, *et al.*, 2014). The Hook domains of Hook homologue 1 (Hook1) and Hook3 proteins have been demonstrated to interact with the C-terminus of DLIC (Table 1) (Lee *et al.*, 2018; Reck-Peterson *et al.*, 2018; Schroeder & Vale, 2016). The Hook domain is typically followed by a central coiled-coil region, important for protein dimerization, along with a less conserved C-terminal cargo-binding domain (Olenick & Holzbaur, 2019). The calcium-binding EF-hand motif is present in the N-terminus of dynein activating adaptors like RAB11 family-interacting protein 3 (RFIP3), Calcium release-activated calcium regulator 2 (CRACR2a), KASH5, Ninein (NIN), and Ninein-like (NINL) (Table 1) (Agrawal *et al.*, 2022; Garner *et al.*, 2023; McKenney *et al.*, 2014; Reck-Peterson *et al.*, 2018; Redwine *et al.*, 2017; Sweeney & Holzbaur, 2018; Wang *et al.*, 2019). More recently, the RH1 domain has been identified as a mediator of the interaction between DLIC and the adaptors C-Jun-amino-terminal kinase-interacting protein 3 (JIP3), JIP4 and Rab-interacting lysosomal protein (RILP) (Table 1) (Arimoto *et al.*, 2011; Cantalupo *et al.*, 2001; Celestino *et al.*, 2022).

Interestingly, the nuclear mitotic apparatus protein (NuMA) is an activating adaptor, containing both a Hook domain and a CC1 box-like motif, distinguishing it from other known adaptors (Table 1) (Colombo *et al.*, 2025; Renna *et al.*, 2020). Although both Hook domain and CC1-box-like motif bind to DLIC, recent work proposed the Hook domain as the main mediator of this interaction, based on cryo-EM studies of NuMA-dynein-dynactin-LIS1 complexes (Aslan *et al.*, 2024).

Further C-terminal to the CC1 box motif, some adaptors contain the Spindly motif (LΦxEΦ, where “Φ” represents an aliphatic or aromatic side chain), which plays a crucial role in interacting with dynactin’s pointed-end (Chaaban & Carter, 2022; Gama *et al.*, 2017; Gassmann *et al.*, 2010; Olenick & Holzbaur, 2019). This motif was initially identified in the

activating adaptor Spindly, and specific mutations were shown to compromise dynein-dynactin-Spindly complex assembly (Gama *et al.*, 2017; Gassmann *et al.*, 2010).

Additional contact between adaptor and dynein occurs through the heavy chain binding site 1 (HBS1) of the adaptor, located approximately 30 residues downstream of the CC1 box (Chaaban & Carter, 2022; Sacristan *et al.*, 2018).

There are adaptors capable of recruiting two dynein motors to a single dynactin, leading to a motor complex exhibiting increased speed and force production (Chaaban & Carter, 2022; Grotjahn *et al.*, 2018; Urnavicius *et al.*, 2018). Moreover, studies suggest that dynactin can bind a second copy of the adaptor, a feature that is likely to enhance the stability of the transport machinery (Chaaban & Carter, 2022).

Certain dynein adaptors are proposed to function as bidirectional adaptors, as they can directly interact with both dynein and kinesin (Abid Ali *et al.*, 2025; Canty *et al.*, 2023; Cason & Holzbaur, 2022; Celestino *et al.*, 2022; Cmentowski *et al.*, 2023; Kendrick *et al.*, 2019; Splinter *et al.*, 2010). In some instances, the dynein and kinesin interaction regions overlap, suggesting that the adaptor may function as a bidirectional switch. For example, Huntingtin-associated protein 1 (HAP1) have been reported to interact with dynein and kinesin via its N-terminus (Cason *et al.*, 2021; Cason & Holzbaur, 2022) . In contrast, some adaptors contain distinct binding motifs for each motor, enabling their simultaneous interaction with both, as in the case of JIP3 (Arimoto *et al.*, 2011; Celestino *et al.*, 2022).

The C-terminal region of activating dynein adaptors is highly variable, reflecting the wide range of cargos they interact with. Dynein typically transports large complexes, including organelles, ribonucleiproteins (RNP) and protein complexes. For instance, BICD2 mediates the transport of Golgi-derived vesicles (Hoogenraad, 2001), while JIP3 is involved in lysosome transport (Celestino *et al.*, 2022). The Hook family participates in endosome motility (Bielska *et al.*, 2014), whereas TRAK proteins specialize in mitochondria trafficking (Canty *et al.*, 2023). In mitosis, Spindly facilitates chromosome alignment by recruiting dynein to kinetochores (Gassmann *et al.*, 2010), while NuMA is crucial for spindle organization and positioning (Renna *et al.*, 2020).

In summary, activating cargo adaptors are essential for converting dynein into a processive motor. By simultaneously binding dynein, dynactin, and cargo, these adaptors relieve dynein autoinhibition and stabilize the formation of a tripartite transport complex. Conserved N-terminal motifs mediate motor activation, while variable C-terminal regions confer cargo specificity (Reck-Peterson *et al.*, 2018).

A number of activating adaptors have been well characterized, and several additional candidates have been proposed (Table 1). These proteins typically contain coiled-coil domains and, based on sequence analysis, feature regions predicted to interact with the

DLIC. However, their ability to directly bind dynein and dynactin, and to activate motility, remains to be experimentally validated (Reck-Peterson *et al.*, 2018).

Despite growing progress in adaptor discovery, some cargos still lack an identified dynein adaptor. It is therefore likely that additional activating adaptors remain to be discovered, underscoring the need for continued functional and biochemical characterization.

Table 1 – Dynein complex activating and candidate adaptors with respective DLIC binding domains and cargos.

Other binding partners (excluding dynein and dynactin) are represented. MT stands for microtubule; "N/A" indicates Not applicable.

Adaptor	DLIC binding domain	Cargo	Other binding partners	References
Activating				
BICD2	CC1-box domain	Golgi vesicles, nuclear pore complex, cytoplasmic vesicles	Rab6a, KIF5B	(Hoogenraad, 2001; Matanis *et al.*, 2002; McKenney *et al.*, 2014; Schlager, Hoang, *et al.*, 2014; Splinter *et al.*, 2010)
BICDR1/ BICDL1	CC1-box domain	Secretory vesicles	Rab6a, Rab6b, KIF1C	(Schlager *et al.*, 2010; Urnavicius *et al.*, 2018)
TRAK1	CC1-box domain	Mitochondria	Miro, KIF5B	(Canty *et al.*, 2023; van Spronsen *et al.*, 2013)
TRAK2	CC1-box domain	Mitochondria, peroxisomes	KIF5A, KIF5C Miro1/2	(Canty *et al.*, 2023; Gama *et al.*, 2017; Gassmann *et al.*, 2010; Griffis *et al.*, 2007; van Spronsen *et al.*, 2013)
Spindly	CC1-box domain	Kinetochores	KNTC1, ZW10	(Gama *et al.*, 2017; Gassmann *et al.*, 2010; Griffis *et al.*, 2007)
HAP1	CC1-box domain	Autophagosomes, BDNF-containing vesicles	HTT, KIF5B	(Cason *et al.*, 2021; Caviston *et al.*, 2007; Li & Li, 2005)
Hook1	Hook domain	Rab5 early endosomes, Clatherin-independent cargos	Rab5, FTS, AKTIP	(Guo *et al.*, 2016; Lee *et al.*, 2018; Olenick *et al.*, 2016)
Hook3	Hook domain	Rab5 early endosomes, Golgi-derived vesicles	Rab5, KIF1C	(Guo *et al.*, 2016; McKenney *et al.*, 2014; Schroeder & Vale, 2016; Walenta *et al.*, 2001)
NuMA	Hook domain & CC1-box-like	Minus ends of MTs, cortical anchor	LGN, RAE1, SPAG5	(Colombo *et al.*, 2025; Hueschen *et al.*, 2017; Merdes *et al.*, 2000; Radulescu

				& Cleveland, 2010; Renna *et al.*, 2020; Walenta *et al.*, 2001)
NIN	EF-hand	Centrosomes	GSK3β	(Redwine *et al.*, 2017)
NINL	EF-hand	Centrosomes, melanosomes, MICAL3A-Rab8a vesicles	APC, MICAL3A, Rab8a	(Bachmann-Gagescu *et al.*, 2015; Redwine *et al.*, 2017)
KASH5	EF-hand	Meiotic chromosomes	SUN1/2	(Agrawal *et al.*, 2022; Garner *et al.*, 2023)
CRACR2a	EF-hand	Different endosomal populations	ORAI1, STIM1	(Wang *et al.*, 2019)
Rab45	EF-hand	N/A	N/A	(Wang *et al.*, 2019)
Rab11-FIP3	EF-hand	Recycling endosomes	Rab11a	(Horgan *et al.*, 2010; McKenney *et al.*, 2014)
JIP3	RH1 domain	Activated JNK and lysosomes	APP	(Arimoto *et al.*, 2011; Cavalli *et al.*, 2005; Celestino *et al.*, 2022; Singh *et al.*, 2024)
JIP4	RH1 domain	Mature autophagic vacuoles, recycling endosomes, lysosomes	Kinesin-1, ARF6, PIP4PI	(Celestino *et al.*, 2022; Montagnac *et al.*, 2009, 2011)
RILP	RH1 domain	Late endosomes, lysosomes	Rab7, Rab36	(Celestino *et al.*, 2022; Scherer *et al.*, 2014)
Candidates				
BICD1	CC1-box domain	COP1-independent Golgi-ER vesicles, MT's arrays	Rab6a, Rab6b, KIFC2	(Fumoto *et al.*, 2006; Matanis *et al.*, 2002; Redwine *et al.*, 2017)
BICDR2/ BICDL2	CC1-box domain	Rab13 vesicles	Rab13	(Schlager *et al.*, 2010)
HOOK2	Hook domain	Golgi-derived vesicles, centrosomes, spermatid intramanchette trafficking;	FTS, AKTIP	(Lee *et al.*, 2018; Okuda *et al.*, 2017; Olenick *et al.*, 2016; Szebenyi *et al.*, 2007)
Girdin/ CCDC88A	Hook domain	Endosomes	DISC, AKT1	(Canty & Yildiz, 2020; Redwine *et al.*, 2017)
CCDC88B	Hook domain	Lytic granules	DOCK8, HSPA5	(Canty & Yildiz, 2020; Ham *et al.*, 2015; Redwine *et al.*, 2017)
Daple/ CCDC88C	Hook domain	N/A	DVL1	(Canty & Yildiz, 2020; Redwine *et al.*, 2017)

3 ENDOPLASMIC RETICULUM

The endoplasmic reticulum (ER) is the largest membrane-bound compartment, with its membranes comprising around half of the total cell membrane, and its lumen enclosing about 10% of the volume of a typical eukaryotic cell (Goyal & Blackstone, 2013). The ER was named by Keith Porter, in 1953, based on observations he made on tissue culture cells using an electron microscope. Porter described this organelle as a fine network of interconnected tubules (a reticulum) present in the endoplasm (perinuclear region of the cytoplasm), therefore the name “endoplasmic reticulum” (Obara *et al.*, 2023; Porter, 1953; Porter *et al.*, 1945). The complex and highly dynamic structure of the ER allows it to play numerous vital roles within the cells, including calcium homeostasis maintenance, protein synthesis, folding and secretion, and lipid synthesis. Moreover, the ER forms extensive contacts with various organelles, coordinating and synchronizing biochemical processes across different cellular locations (Obara *et al.*, 2023). Understanding the dynamics and mechanisms regulating the ER is essential, as dysfunction in this organelle can result in a variety of diseases, including neurodegenerative disorders and metabolic syndromes (Arruda & Parlakgül, 2023; Goyal & Blackstone, 2013).

3.1 ER morphology and function

The ER is a single, continuous, membrane-bound compartment that extends throughout the cell (Obara *et al.*, 2023; Perkins *et al.*, 2021). The ER membrane system consists of morphologically distinct subdomains: the nuclear envelope (NE), ER tubules and ER sheets (Figure 4) (Obara *et al.*, 2023; Zhang & Hu, 2016). However, recent advancements in super-resolution light microscopy and three-dimensional electron microscopy (EM) have uncovered a remarkable diversity of nanoscale ER structures, significantly broadening our understanding of ER organization (Obara *et al.*, 2023; Perkins & Allan, 2021; Zucker & Kozlov, 2022).

The NE, composed of the nuclear inner and outer membranes, establishes a unique environment to safeguard genetic material and regulates exchanges between the nucleus and cytoplasm. The ER is physically connected to the nucleus by junctions with the outer membrane of the nuclear envelope (ER-NE junctions). These ER-NE junctions are important to supply the NE with lipids and proteins synthesized in the ER (Bragulat-Teixidor *et al.*, 2024). While the NE appears spherical in cells, its substantial diameter of around 6–10 µm gives the inner and outer nuclear membranes a flattened, sheet-like appearance, with high-curvature regions mostly restricted to the edges of nuclear pores (Figure 4) (Goyal & Blackstone, 2013).

ER tubules are narrow and highly curved structures that are connected by three-way junctions, forming a reticular network that reaches the farthest edge of the cell (Figure 4) (Obara *et al.*, 2023; Shibata *et al.*, 2009; Voeltz *et al.*, 2006). Functionally, ER tubules play a role in lipid synthesis and delivery, carbohydrates metabolism, Ca^{2+} storage, and in the establishment of contacts with other organelles (Arruda & Parlakgül, 2023; Goyal & Blackstone, 2013).

ER sheets are mainly located in the perinuclear region, whereas ER tubules form a reticular network that is found in both the perinuclear and peripheral regions of the cell's cytoplasm (Zhang & Hu, 2016). ER sheets are cisternal structures formed by two closely apposed membranes with a uniform luminal space between them and bordered at the edges by curved membranes (Figure 4). In mammalian cells, the distance between membranes is approximately 50–100 nm, similar to the diameter of a tubule (30–100 nm) (Goyal & Blackstone, 2013; Shibata *et al.*, 2010). ER sheets are the primary site for protein synthesis, folding, and post-translational modifications (Figure 4) (Arruda & Parlakgül, 2023).

The proportion of sheets and tubules varies across different cell types and is associated with the number of membrane-bound ribosomes involved in synthesizing secretory proteins. For instance, cells with high protein secretory capacity (*e.g.*, pancreatic and salivary cells) are predominantly enriched in rough ER sheets that are studded with ribosomes and polysomes. Whereas smooth tubules devoid of membrane-bound ribosomes are prominent in adrenal cortex cell, which have lower capacity for protein secretion (Goyal & Blackstone, 2013; Schwarz & Blower, 2016; Shibata *et al.*, 2010; Terasaki *et al.*, 2013).

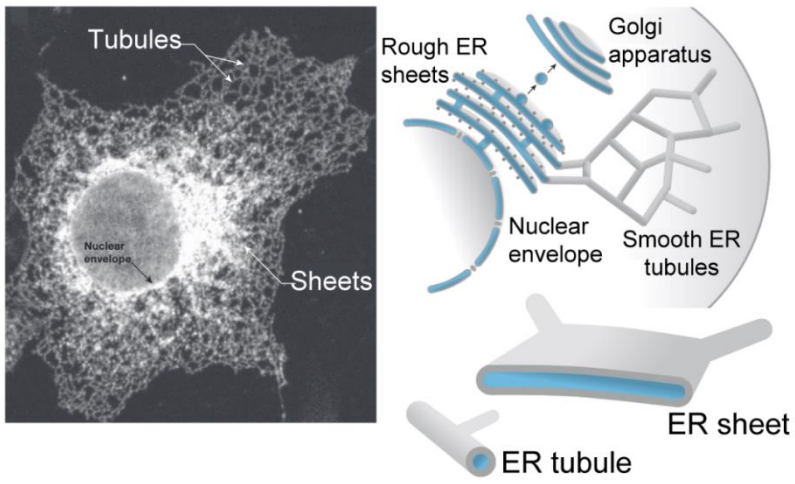

Figure 4 – Morphology of the ER.

(left) COS7 cell immunostained with ER markers Sec61b and DP1/REEP5, showing distinct ER domains, as labelled. *(right)* Schematic representation of ER domains, emphasizing the morphological differences between tubules and sheets. Adapted from Park & Blackstone, 2010.

3.2 ER shaping and remodeling

The morphology of the ER is supported by ER shaping proteins and interactions with the cytoskeleton and other organelles (Schwarz & Blower, 2016). These interactions are dynamic and reflect cellular changes driven by the cell cycle, developmental stage, differentiation processes, intracellular signaling or protein interactions (Obara *et al.*, 2023; Schwarz & Blower, 2016). ER diverse morphologies are mainly determined by variations in membrane curvature, enabling ER domains to adopt distinct shapes and functions while remaining part of a continuous membrane. Although the basic shapes of ER tubules and sheets are generally understood, both arising from shared mechanisms involving common protein modules, the regulation of shape changes or the ratio of tubules to sheets in response to specific cellular signals are still unclear (Goyal & Blackstone, 2013; Schwarz & Blower, 2016).

3.2.1 Formation of ER tubules

ER tubules are cylindrical structures and are therefore characterized by high membrane curvature. Several proteins have been identified as key regulators of membrane curvature, with the most prominent being the canonical reticulons (Rtns) and the receptor expression-enhancing protein 5 (REEP5 or DP1; Yop1 in yeast) (Figure 5) (Obara *et al.*, 2023; Schwarz & Blower, 2016; Zhang & Hu, 2016). For instance, overexpression of these proteins promotes the formation of ER tubules, whereas their depletion or deletion results in a reduction of tubule formation (Shibata *et al.*, 2010; Zhang & Hu, 2016). Both protein families possess a conserved reticulon-homology domain (RHD), consisting of two long hydrophobic segments that appear to form a wedge-shaped hairpin configuration. It is thought that the bulk of this hydrophobic segments resides in the outer leaflet of the ER membrane, thereby inducing membrane curvature (Figure 5) (Obara *et al.*, 2023; Park & Blackstone, 2010; Shibata *et al.*, 2010; Zhang & Hu, 2016). Although hydrophobic hairpins are important for ER tubule assembly, cytoplasmic domain interactions may also play a role, as these proteins can be crosslinked by hydrophilic, membrane-impermeable crosslinkers (Obara *et al.*, 2023; Park & Blackstone, 2010).

Generating ER tubules is only one part of the process, as an interconnected tubular ER network also relies on tubule fusion. Consequently, ER tubules constantly fuse and branch, leading to the formation of three-way junctions that create the ER's characteristic polygonal peripheral structure (Goyal & Blackstone, 2013; Obara *et al.*, 2023; Schwarz & Blower, 2016). The precise mechanisms leading to tethering and fusion of three-way junctions remain unclear, partly because ER tubules tethered to one another cannot be easily distinguished from fused tubules by light microscopy. Nevertheless, in mammalian cells,

Atlastin proteins, Lunapark, AAA ATPase spastin, and various GTPases have been implicated in this process (Obara *et al.*, 2023).

3.2.2 Formation of ER sheets

ER sheets are flattened cisternal structures that maintain a constant distance between two apposed membranes (Obara *et al.*, 2023; Zhang & Hu, 2016). Compared to ER tubule formation, the mechanisms responsible for flattening ER membranes into ER sheets remain less understood. Given that the edges of ER sheets are highly curved, resembling the curvature of ER tubules, it is conceivable that the same proteins generate the curvature in both structures (Figure 5) (Shibata *et al.*, 2010; Zhang & Hu, 2016). Indeed, tubule-forming proteins localize to the edges of ER sheets, and their abundance influences the balance between sheets and tubules within cells (Shibata *et al.*, 2010; Zhang & Hu, 2016). In mammalian cells, the conserved luminal spacing of ER sheets is maintained through various mechanisms, with proteins like cytoskeleton-linking membrane protein 63-kDa (CLIMP63), ribosome-binding protein 1 homolog 180-kDa (RRBP1 or p180), kinectin (KTN1), and sigma-1 receptor (SigmaR1) playing key roles. These proteins are enriched in ER sheets and their overexpression enhances sheet formation (Goyal & Blackstone, 2013; Obara *et al.*, 2023; Sawyer *et al.*, 2024; Shibata *et al.*, 2010). CLIMP63, p180 and KTN1 are the best well studied ER-resident proteins. All three contain long dimerizing coiled-coil domains, which are believed to be essential for their function in stabilizing ER sheets. For example, the coiled-coil domains of CLIMP63 are positioned in the ER lumen, where they may form intraluminal bridges that help stabilize the sheet's width. In contrast, the coiled-coil domains of p180 and KTN1 are cytoplasmic and are believed to form rod-like scaffolds that contribute to maintaining the flatness of the sheets (Figure 5) (Goyal & Blackstone, 2013; Obara *et al.*, 2023; Zhang & Hu, 2016).

Additional factors affecting ER sheet thickness include polyribosome complexes, which are bound to the cytoplasmic face of the ER. As an example, removal of ribosomes from the ER surface transforms sheets into tubules, supporting the idea that polyribosomes help stabilize ER sheets (Perkins & Allan, 2021; Puhka *et al.*, 2007; Shibata *et al.*, 2006).

ER sheets are typically tightly packed on top of one another with consistent spacing between them (Obara *et al.*, 2023; Porter *et al.*, 1945; Porter & Palade, 1957). Reconstructions of serial electron microscopy (EM) sections have shown that stacked ER sheets form a continuous membrane system, where sheets are interconnected by twisted membrane surfaces with helical edges of either right- or left-handed orientation, similar to the spiraling ramps that connect different levels in a parking garage (Obara *et al.*, 2023; Terasaki *et al.*, 2013). A theoretical model suggests that these helicoidal structures alleviate

elastic stress within the stacked ER sheets while enabling their compact organization in the confined space of the cell (Obara *et al.*, 2023; Shemesh *et al.*, 2014; Terasaki *et al.*, 2013). Stacked helicoidal sheets are typically covered with ribosomes (Obara *et al.*, 2023).

Although most cells contain at least some stacked ER sheets, not all sheets are organized in this manner. Three-dimensional EM studies have described the presence of isolated sheets in the perinuclear and transitional regions of various cell types, with a particularly high prevalence in cultured cells (Obara *et al.*, 2023). Similar to stacked sheets, these structures also exhibit a degree of curvature, frequently appearing as twisted layers resembling a single layer of a helicoidal stack (Obara *et al.*, 2023).

ER sheets can also form large, continuous structures that lack the characteristic constant luminal spacing, giving rise to ER cisternae or to fenestrated sheets (Obara *et al.*, 2023). ER cisternae are predominantly found in the perinuclear region and are frequently coated with polyribosomes, indicating their potential involvement in protein translation (Heinrich *et al.*, 2021; Obara *et al.*, 2023). Fenestrated ER sheets, on the other hand, are characterized by numerous pores (fenestrations) of varying sizes. Unlike stacked or twisted sheets, fenestrated sheets remain essentially planar and are found in both perinuclear and peripheral ER regions (Nixon-Abell *et al.*, 2016; Obara *et al.*, 2023; Schroeder *et al.*, 2019). Identifying these structures has been challenging due to their similarity to other ER domains, but recent studies have classified them as a distinct and abundant ER component. The mechanisms underlying fenestrated sheet formation remain unclear (Obara *et al.*, 2023).

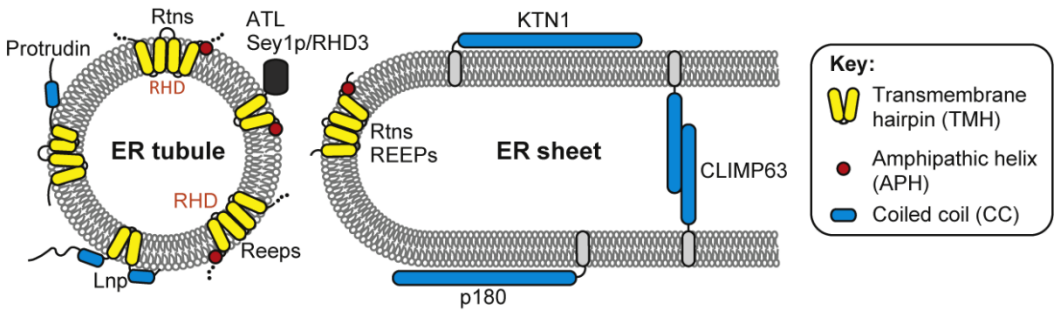

Figure 5 – Determinants for ER shaping and remodeling.

ER-shaping proteins are shown in tubules and sheets. Rtns and REEPs are key regulators of membrane curvature in both tubules and sheets. CLIMP63, p180 and KTN1 are important for ER sheets formation. Highlighted are common protein modules, such as transmembrane hairpins (TMH), amphipathic helices (APH), and coiled-coils (CC). Dotted lines indicate variable regions within protein families. The reticulon-homology domain (RHD) consists of two TMHs connected by a loop. Adapted from Zhang & Hu, 2016.

3.3 Regulation of ER dynamics by the microtubule cytoskeleton

The shape and distribution of the ER network within the cell undergo continuous remodeling and reorganization in response to numerous intracellular and external signals. The dynamics and stability of the ER network are heavily influenced by interactions with other cellular structures, particularly microtubules (Perkins & Allan, 2021; Schwarz & Blower, 2016). Early studies revealed that ER tubules in the cell periphery closely align with microtubules and that microtubule depolymerization leads to ER collapse, characterized by retraction of ER tubules from the cell periphery and its transformation into extended sheet-like structures (Goyal & Blackstone, 2013; Perkins & Allan, 2021).

The processes that govern the dynamics of the ER network are complex, especially when considering the denser perinuclear ER, which remains less explored compared to peripheral tubular ER (Zheng *et al.*, 2022). Five different types of ER-microtubule interactions have been purposed to regulate the dynamic nature of the ER (Figure 6). (1) Static interactions occur when the ER is anchored to microtubules through direct interactions between ER-resident proteins and the microtubule network. For example, CLIMP63, p180 and KTN1 contain microtubule-binding domains, that enable their direct association with microtubules. (2) ER tubules associate with growing microtubule tips through interactions with the polymerizing tip attachment complex (pTAC), allowing the ER membrane to extend alongside the elongating microtubule. This process is mediated by the association of plus-end binding proteins (EB), such as EB1, with specific ER-resident proteins, including stromal interaction molecule 1 (STIM1). (3) Conversely, the ER can also associate with depolymerizing microtubule tips undergoing catastrophe (dTAC). However, the molecular components responsible for this interaction remain unidentified. (4) ER tubules can also extend by hitchhiking on motile organelles, such as lysosomes, which serve as carriers to facilitate ER network remodeling. Finally, (5) ER tubules can extend by sliding along pre-existing microtubules through the activity of molecular motors, which transport the ER along microtubule tracks (see section *3.3.1*; Figure 6) (Goyal & Blackstone, 2013; Guo *et al.*, 2018; Obara *et al.*, 2023; Perkins & Allan, 2021; Schwarz & Blower, 2016). A recent work, reported that in mammalian COS7 cells, approximately 20% to 40% of tubule extension events occur through pTAC or dTAC-mediated motion, with the remaining events being linked to sliding or organelle hitchhiking (Guo *et al.*, 2018; Obara *et al.*, 2023).

Regarding ER sheet morphology regulation, recent research has shed light on how ER-resident proteins interact with specific microtubule populations to regulate ER sheet morphology. Zheng and colleagues demonstrated that CLIMP63, p180 and KTN1 preferentially bind distinct subsets of microtubules, ensuring the proper distribution of perinuclear ER (Zheng *et al.*, 2022). This selective binding explains the differing phenotypes

observed upon depletion of these proteins and highlights the role of microtubule-binding specificity in maintaining ER sheet organization (Zheng *et al.*, 2022). Specifically, CLIMP63 associates with centrosomal microtubules, p180 preferentially binds glutamylated microtubules, and KTN1 interacts with perinuclear polyglutamylated microtubules with extended glutamate chains (Zheng *et al.*, 2022). Therefore, deletion of these proteins or alteration in microtubule populations and glutamylation status result in significant changes in ER positioning, subsequently causing similar redistributions of other organelles (Zheng *et al.*, 2022).

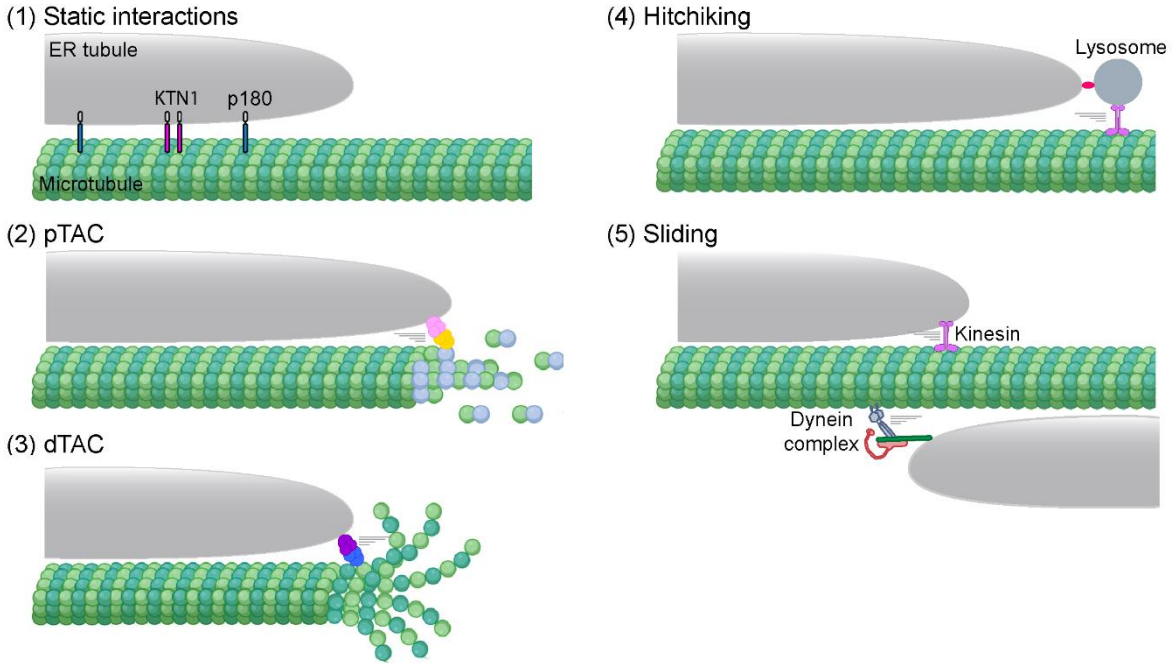

Figure 6 – Regulation of ER dynamics by ER-microtubule interactions.
Cartoon representing different mechanisms of ER tubulation/extension. (1) Static interactions anchor ER to microtubules; (2) ER tubules extend alongside microtubules via association with growing microtubule tips through interactions with the pTAC; (3) ER tubules associate with depolymerizing microtubule tips via dTAC; (4) ER tubules extend by hitchhiking on motile organelles such as lysosomes; (5) ER tubules move by sliding along pre-existing microtubules, driven by molecular motors such as kinesins and dynein. Adapted from Obara *et al.*, 2023

3.3.1 Regulation of ER dynamics by microtubule motors

Microtubule motors, such as kinesin-1 and dynein, drive the movement of ER tubules along the microtubule tracks, enabling the rapid repositioning and extension of the ER network within the cell.

More than three decades ago, the anterograde motor kinesin-1 was proposed as the motor responsible for driving ER tubule extension, a role later confirmed through *in vitro* motility assays (Dabora & Sheetz, 1988; Lane & Allan, 1999; Woźniak & Allan, 2006). However, in living cells, the role of kinesin-1 in ER motility has remained a topic of debate, with studies presenting conflicting results regarding its impact on ER morphology. Evidence supporting kinesin-1 involvement in ER motility includes studies showing that in astrocytes, downregulation of kinesin-1, using an antisense approach, results in ER clustering around the nucleus, resembling the changes seen upon microtubule depolymerization (Feiguin *et al.*, 1994). In contrast, work in mammalian Vero cells, showed that inhibition of kinesin-1, achieved by overexpressing kinesin-1-inhibitory fragments, blocked outward ER tubule movement and increased the proportion of ER sheets in the cell periphery (Woźniak *et al.*, 2009). Nevertheless, other studies have questioned the critical role of kinesin-1 in ER motility within cells. For instance, the KO of the gene encoding the kinesin-1 motor subunit KIF5B in mice did not result in significant changes in ER morphology (Tanaka *et al.*, 1998). Similarly, the inhibition of kinesin-1 activity by function-blocking antibodies in sea urchin eggs had no apparent effect on ER structure (Wright *et al.*, 1993). These contrasting findings suggest that while kinesin-1 may play a role in certain contexts or specific cell types, its contribution to overall ER morphology in cells remains unclear.

While kinesin-1 drives the outward extension of ER tubules, dynein plays a complementary role by mediating inward-directed movement. Dynein has been shown to transport ER tubules in mammalian and amphibian eggs and in the fungus *Ustilago maydis* (Allan, 1995; FitzHarris *et al.*, 2007; Niclas *et al.*, 1996; Perkins & Allan, 2021; Wedlich-Söldner *et al.*, 2002; Woźniak *et al.*, 2009). However, its role in ER motility in cultured cells has been debated, as its inhibition does not produce uniform effects across different cell types. For example, disrupting dynein function by overexpressing the dynactin's p50 subunit has no noticeable impact on ER morphology in HeLa cells (Burkhardt *et al.*, 1997; Perkins & Allan, 2021). In contrast, in Vero cells, dynein inhibition results in the accumulation of ER sheets in the cell periphery while leaving outward kinesin-driven movement unaffected. (Burkhardt *et al.*, 1997; Perkins & Allan, 2021; Woźniak *et al.*, 2009). Additionally, in Vero cells, dynein is responsible for approximately half of the rapid ER tubule movements toward the cell center (Perkins & Allan, 2021; Woźniak *et al.*, 2009).

In conclusion, both kinesin-1 and dynein contribute to ER tubule motility, with kinesin-1 directing movement toward the cell periphery and dynein toward the cell center. Despite their essential roles, the identities of the kinesin-1 and dynein receptors/adaptors on the ER remain unknown. Several candidate receptors for kinesin-1 have been proposed, but their precise functions and interactions with these motors require further investigation. Currently, no dynein adaptor for the ER has been reported.

3.3.1.1 KTN1 and p180 as ER receptors for microtubule motors

The identification of the kinesin-1 receptor on the ER remains an open question, with several candidates proposed, including KTN1, p180, Rab10, Rab18, protrudin, and the DNAJ homolog subfamily B member 14 (DNAJB14). However, their precise roles in ER motility are still under debate (Perkins & Allan, 2021).

Kinectin (KTN1), named after “kinesin” and the Latin verb *nectere* (“to connect”), was among the first identified candidates. It was identified through an affinity purification method that used the kinesin tail domain as bait and detergent-solubilized chick embryo brain microsomes (Toyoshima *et al.*, 1992). Later, human KTN1 was also shown to interact with the C-terminus of KIF5A/B/C (Kumar *et al.*, 1995; Ong *et al.*, 2000; Perkins & Allan, 2021; Toyoshima *et al.*, 1992). Nevertheless, its role in ER motility may be cell type-specific, affecting ER positioning in some cells but not others (Perkins & Allan, 2021). KTN1 KO led to ER clustering in COS7 cells, whereas in U2OS cells, the ER became dispersed, likely reflecting KTN1’s preference for polyglutamylated microtubules, which are more abundant in COS7 cells (Zheng *et al.*, 2022). In contrast, mouse embryonic fibroblasts derived from KTN1 KO mice showed no defects in ER distribution (Perkins & Allan, 2021; Plitz & Pfeffer, 2001). KTN1 has been implicated in regulating focal adhesion dynamics during chemotaxis by forming a complex with kinesin-1 (Guadagno *et al.*, 2020; Ng *et al.*, 2016). One of the referred studies also reported the small GTPase Rab18 as a positive regulator of directional cell migration by promoting the targeting of the ER to focal adhesions at the cell’s leading edge (Guadagno *et al.*, 2020). In a study using brain microsomes, a weak interaction between KTN1 and dynein was suggested, as an antibody binding to the C-terminal domain of KTN1 blocked dynein binding to microsomes and reduced dynein-mediated motility (Kumar *et al.*, 1995). However, the functional significance of such potential interaction remains uncertain.

Another potential ER kinesin-1 receptor is p180, which shares homology with the kinesin-1 binding site of KTN1, and like KTN1, localizes to ER sheets in cells (Diefenbach *et al.*, 2004; Perkins & Allan, 2021). Yeast two-hybrid experiments have demonstrated an interaction between p180 and KIF5B (Diefenbach *et al.*, 2004). Unlike KTN1 KO, p180 KO leads to ER clustering, where the peripheral network remains tubular while the perinuclear ER collapses asymmetrically into a smaller region on one side of the nucleus (Zheng *et al.*, 2022). p180 has been shown to associate with both mono- and polyglutamylated microtubules, which are differentially distributed within the cell—monoglutamylated microtubules are more abundant in the periphery, while polyglutamylated microtubules are concentrated near the nucleus. This distribution aligns with p180’s association with peripheral microtubules and explains why its KO leads to ER clustering (Zheng *et al.*, 2022).

p180 has also been reported to be essential for peroxisome biogenesis and to play a role in forming membrane contact sites between the ER and peroxisomes in human cells (Fatima *et al.*, 2024).

3.4 Protein translation and the role of translation elongation factor-1

The ER plays an important role in protein synthesis, especially for secreted and integral membrane proteins, as well as for a subset of cytosolic proteins (Schwarz & Blower, 2016). ER sheets are often studded with membrane-bound ribosomes, creating the rough ER, where protein translation occurs. When multiple ribosomes bind to the same mRNA molecule, they form polysomes, which help concentrate translocon components and other elements of the translation machinery at specific sites on the ER membrane (Shibata *et al.*, 2010). In cases where messenger RNAs (mRNA) are translated by stably-bound ER ribosomes, the mRNAs are released after translation, while the ribosomes can remain attached to the ER and engage in multiple rounds of translation (Schwarz & Blower, 2016). The mechanisms by which mRNAs encoding cytosolic proteins are recruited to ER-bound ribosomes, and which ribosome populations initiate their translation, remain unclear (Schwarz & Blower, 2016). Shibata and colleagues proposed that ER sheet-associated proteins CLIMP63, p180, and KTN1 may have a direct or indirect affinity for membrane-bound polysomes (Shibata *et al.*, 2010). In contrast, Cui and colleagues suggested that p180 is specifically required for anchoring certain transcripts to the ER by directly interacting with RNA (Cui *et al.*, 2012; Schwarz & Blower, 2016).

The ER-sheet protein KTN1 has been implicated in protein translation through its interaction with the Elongation factor-1B (eEF1B). Specifically, KTN1 was shown to bind eEF1Bβ, a subunit of the eEF1B complex, suggesting a role in anchoring the translation machinery to the ER membrane (Ong *et al.*, 2003). Mammalian eEF1B's main function is to catalyze nucleotide exchange in eEF1A, which supplies the 80S ribosomes with aminoacyl-transfer RNAs (tRNA) (Negrutskii, 2020; Xu *et al.*, 2021). The eEF1B consists of three subunits: eEF1Bα, eEF1Bβ, and eEF1Bγ (Negrutskii *et al.*, 2023). While eEF1Bα and eEF1Bγ are highly conserved throughout evolution, eEF1Bβ is a metazoan-specific protein (Negrutskii *et al.*, 2023). The N-terminal domains of all three subunits mediate their assembly into the eEF1B complex, whereas the C-terminal domains of eEF1Bα and eEF1Bβ are responsible for the nucleotide exchange activity (Negrutskii *et al.*, 2023). Structurally, eEF1B is organized around two key components: eEF1Bβ, which forms a stable homotrimer, and eEF1Bγ that links eEF1Bβ to eEF1Bα within the complex (Bondarchuk *et al.*, 2022).

To accomplish the guanine-nucleotide exchange reaction, eEF1B associates with eEF1A forming a supercomplex known as heavy complex or eEF1H (Bondarchuk *et al.*, 2022; Negrutskii *et al.*, 2023). The purposed structure for eEF1H is built around a trimer of eEF1Bβ subunits, stabilized by a central LZ region. The C-terminal domain of each eEF1Bβ subunit binds with one eEF1A2 molecule. While its N-terminal domain associates with eEF1Bγ. Each eEF1Bγ then interacts with a complex consisting of eEF1Bα subunit and an additional eEF1A2 molecule (Bondarchuk *et al.*, 2022; Negrutskii *et al.*, 2023).

An apparent function of the stable trimeric eEF1B complex is to elevate the local concentration of guanine nucleotide factor (GEF) domains, which likely supports efficient GDP/GTP exchange on eEF1A molecules near translating ribosomes (Negrutskii *et al.*, 2023). As both eEF1Bα and eEF1Bβ exhibit comparable guanine nucleotide exchange activity *in vitro*, the reason for the presence of two distinct exchange factors within the same complex and whether they are functionally redundant *in vivo* remains unclear (Bondarchuk *et al.*, 2022; Negrutskii *et al.*, 2023).

4 CEREBELLAR DEGENERATION-RELATED PROTEINS

Cerebellar degeneration-related protein 2 (CDR2) and its paralog CDR2-like (CDR2L) are proteins associated with paraneoplastic cerebellar degeneration (PCD), a rare immune-mediated disorder triggered by gynaecological and breast cancers (Abbatemarco *et al.*, 2024). In patients with PCD, tumor-induced autoimmunity against neuronal antigens, including CDR2 and CDR2L, causes degeneration of Purkinje cells in the cerebellum, but the pathogenetic mechanism and the physiological roles of CDR2 and CDR2L remain unknown (Greenlee & Brashear, 2023).

4.1 Paraneoplastic cerebellar degeneration

Paraneoplastic neurologic syndromes are a group of rare immune-mediated disorders that impacts the nervous system in individuals with cancer. These syndromes, by definition, are not the result of direct tumor invasion or metastasis, but rather occur due to the autoimmune response targeting neuronal proteins expressed by the tumor (onconeural antigens) (Dalmau & Rosenfeld, 2008; Greenlee *et al.*, 2022). PCD is one of the most common paraneoplastic neurologic syndromes and it is characterized by severe loss of cerebellar Purkinje cells and the presence of inflammatory infiltrates in affected areas of the nervous system, which leads to fast and progressive ataxia, nystagmus and dysarthria (Shams'Ili *et al.*, 2003). PCD is associated with a variety of onconeural antibodies, with the most well-characterized being anti-Yo (gynaecological and breast cancers), anti-Hu (small cell lung cancer), and anti-Tr (Hodgkin's lymphoma) (Dalmau & Graus, 2012; Lozada *et al.*, 2025). Anti-Yo PCD represents approximately half of all PCD cases, making it the most thoroughly studied paraneoplastic neurologic syndromes (Venkatraman & Opal, 2016).

Yo antibodies (anti-Yo) were first identified in 1983 by Greenlee and Bashear in patients with cerebellar degeneration in the setting of ovarian cancer, and later confirmed by Jaeckle and colleagues (Greenlee *et al.*, 2022; Greenlee & Brashear, 1983, 2023; Jaeckle *et al.*, 1985). These antibodies were shown to react with specific proteins intracellularly expressed in Purkinje neurons: CDR1, CDR2 and CDR2L (Greenlee & Brashear, 2023; Lozada *et al.*, 2025). Currently, CDR1 is not recognized as a marker for Yo-PCD, and it has been shown that CDR2L, rather than CDR2, is the principal Yo antigen (Kråkenes *et al.*, 2019; Totland *et al.*, 2018).

4.2 CDR2 and CDR2L: molecular characteristics and subcellular localization

The human CDR2 gene (NCBI 1039), located on chromosome 16 at locus 16p12, encodes a 454-amino-acid protein (Uniprot Q01850) with an estimated molecular weight of

52 kDa, though reported weights range from 52 to 62 kDa (Darnell *et al.*, 2000; Eichler *et al.*, 2013; Raspotnig *et al.*, 2022). The human CDR2L gene (NCBI 30850) is located on chromosome 17 (locus 17q25.1) and encodes a 465-amino-acid protein (Uniprot Q86X02) with a predicted molecular weight of 53 kDa, although molecular weights as high as 62 kDa have been also reported (Eichler *et al.*, 2013; Raspotnig *et al.*, 2022). CDR2 and CDR2L are paralogous proteins sharing 45% sequence identity and 60% similarity. CDR2 was long considered the primary Yo antigen, largely due to the detection of *CDR2* mRNA in PCD-associated tumors (Corradi *et al.*, 1997). Nonetheless, in 2013, CDR2L emerged as a key factor in PCD and, later, it was described as the main Yo antigen (Eichler *et al.*, 2013; Kråkenes *et al.*, 2019). The expression of CDR2 and CDR2L was initially thought to be restricted to immune-privileged tissues, such as the cerebellum and testis, as well as in cancerous tissues. However, studies have since shown broader expression of both paralogs in normal and malignant tissues (Raspotnig *et al.*, 2017; Totland *et al.*, 2013).

In 1997, Corradi and colleagues reported that expression of CDR2 protein in mice was restricted to Purkinje and brainstem neurons and testes (Corradi *et al.*, 1997). Immunostaining of rat cerebellum sections using serum from a PCD patient positive for both CDR2 and CDR2L, along with commercially available antibodies, revealed cytoplasmic staining in Purkinje, stellate, and basket cells. Notably, CDR2L exhibited a stronger cytoplasmic signal compared to CDR2 in Purkinje cells and molecular layer interneurons (Raspotnig *et al.*, 2017). Immunoblot analysis of rat brain cortical lysates revealed that CDR2 protein expression is abundant in prenatal and early postnatal stages but undergoes a significant downregulation in adulthood (Hwang *et al.*, 2016). A similar pattern is observed in *Drosophila melanogaster*, where the CDR2 and CDR2L ortholog, Centrocortin (CEN), is highly expressed in ovaries and early embryos but declines to very low levels in late embryonic and larval stages (Kao & Megraw, 2009).

In the subsequent years, CDR2 was reported to be expressed in a variety of cancer cell lines, including those derived from cervical, ovarian, lung, neuroblastoma, and colon cancers (Balamurugan *et al.*, 2009; Darnell *et al.*, 2000; Raspotnig *et al.*, 2017; Totland *et al.*, 2011). Nevertheless, more recent studies have been showing a ubiquitous CDR2 and CDR2L expression in different cancerous and normal tissues (Kråkenes *et al.*, 2019; Raspotnig *et al.*, 2017, 2022; Totland *et al.*, 2011). Immuno-EM analyses of sera from PCD patients revealed that Yo antibodies localize to the cytoplasm and associate with both membrane-bound and free ribosomes in rat cerebellum (Hida *et al.*, 1994; Rodriguez *et al.*, 1988). Given that CDR2L has been identified as the major Yo antigen, these findings likely reflect the cellular localization of CDR2L (Kråkenes *et al.*, 2019). Recent work using both PCD sera and commercial anti-CDR2/CDR2L antibodies further supports this, showing that CDR2L associates with ribosomes, whereas CDR2 localizes to nuclear speckles in cancer

cell lines (Herdlevær *et al.*, 2020). Using mass spectrometry, super-resolution microscopy, and proximity ligation assays, Herdlevær and colleagues reported that CDR2 co-localizes and, potentially interacts, with the nuclear speckle proteins eukaryotic initiation factor 4A-III (eIF4A3) and SON, while CDR2L co-localizes with and may interact with the small ribosomal subunit protein eS6 (rpS6) (Herdlevær *et al.*, 2020). These findings indicate that CDR2 may play a role in mRNA maturation and CDR2L in protein synthesis.

4.3 CDR2 and CDR2L: Potential functions

4.3.1 Gene expression and regulation

Currently, CDR2/L functional role in cells is not well understood. The first insight about a biological function started with the identification of an extended amphipathic helix comprising a LZ motif in the N-terminal region of CDR2 (O'Donovan *et al.*, 2010; Okano *et al.*, 1999). The presence of a LZ motif in CDR2, a common dimerization motif in transcription factors, led to the hypothesis that CDR2 might function as a transcription factor or regulate gene expression by interacting with transcriptional regulators (O'Donovan *et al.*, 2010; Okano *et al.*, 1999; Sakai *et al.*, 2002). Accordingly, some LZ motif-containing proteins were proposed as CDR2 interactors: c-Myc, Mortality factor 4-like protein 2 (MRGX), Mortality factor 4-like protein 1 (MRG15), and Prolyl hydroxylase domain-containing protein 1 (PHD1) (Balamurugan *et al.*, 2009; O'Donovan *et al.*, 2010; Okano *et al.*, 1999; Sakai *et al.*, 2002, 2004; Takanaga *et al.*, 1998).

In 1999, Okano and colleagues reported that CDR2 interacts with c-Myc, a nuclear transcription factor, resulting in their colocalization in the cytoplasm of Purkinje neurons (Okano *et al.*, 1999). The prediction is that CDR2's LZ motif would directly interact with the LZ motif of c-Myc. Consequently, this interaction sequesters c-Myc in the cytoplasm and down-regulates c-Myc-dependent transcription, as demonstrated in co-transfection assays where increasing CDR2 levels resulted in decreased transcriptional activity of c-Myc (Okano *et al.*, 1999). Additionally, sera from PCD patients, previously reported to recognize an epitope in the region of the CDR2's LZ domain, disrupted CDR2 and c-Myc interaction, suggesting that CDR2 antibodies may antagonize the actions of CDR2 and c-Myc in the cytoplasm, leading to an increased c-Myc activity in the cytoplasm (Okano *et al.*, 1999). Given that aberrant activation of c-Myc-related pathways in Purkinje neurons is linked to apoptotic cell death, these findings suggested a mechanistic link between immune-mediated disruption of CDR2 function and neuronal degeneration in PCD (Okano *et al.*, 1999; Sakai *et al.*, 1993). More than a decade later, O'Donovan and colleagues reported that CDR2 interacts with c-Myc and synergistically regulates c-Myc-dependent transcription during mitosis (O'Donovan *et al.*, 2010). The authors described that CDR2 protein levels

fluctuate throughout the cell cycle, peaking during mitosis, after which it is ubiquitinated by the anaphase-promoting complex/cyclosome (APC/C) and rapidly degraded by the proteasome as cells exit mitosis (O'Donovan *et al.*, 2010). Moreover, CDR2 knockdown resulted in a greater proportion of cells with aberrant multipolar mitotic spindles (21% in CDR2 knockdown cells *vs.* 11% in controls) and defects in cell proliferation, but did not lead to significant cell cycle arrest (O'Donovan *et al.*, 2010). This study provided insight into a potential role for CDR2 in mitosis.

Sakai and colleagues described two other transcription factors as CDR2 interactors, namely MRGX and MRG15, which belong to the Mortality factor 4 (MORF4)-related gene (MRG) family of transcription factors (Sakai *et al.*, 2002, 2004). These evolutionarily conserved proteins are involved in DNA damage repair, cell proliferation, cellular senescence and apoptosis (Garcia & Pereira-Smith, 2008). In brief, overexpression of MRGX in glioblastoma cells led to abnormal nuclear morphology and cell death, while co-expression with CDR2 prevented these changes (Sakai *et al.*, 2002). In glioblastoma cells co-expressing CDR2 and MRGX, the subcellular localization of these proteins varies between individual transfected cells. In some cells, MRGX is retained in the cytoplasm along with CDR2, whereas in others, both proteins are distributed across the nucleus and cytoplasm (Sakai *et al.*, 2002). These observations suggested that CDR2 may regulate MRGX's functions, potentially influencing transcriptional regulation and the pathogenesis of PCD (Sakai *et al.*, 2002). In 2004, Sakai and colleagues also reported that CDR2 binds to MRG15. This transcription factor is known to displaces the E2F transcription factor from the tumor suppressor retinoblastoma protein (Rb), wherefore increasing E2F-responsive B-myb promoter activity, leading to neuronal apoptosis (Leung *et al.*, 2001). The authors reported that CDR2 interacts with MRG15, diminishing its effect on B-myb promoter activity. However, anti-Yo antibodies can reverse this repression, suggesting a potential pathogenic role in PCD (Sakai *et al.*, 2004). This finding indicates that CDR2 acts as a negative regulator of MRG15-induced B-myb promoter activation, a process crucial for neuronal survival (Sakai *et al.*, 2004).

CDR2 was also reported to interact with PHD1. Prolyl hydroxylases (PHD1-3) play an important role in regulation of the HIF, which coordinates the adaptive transcriptional response to hypoxia in metazoan cells (Balamurugan *et al.*, 2009; Kennel *et al.*, 2018). Under normoxic conditions, PHD proteins hydroxylate the HIF1α subunit, marking it for proteasomal degradation. In hypoxic conditions, the absence of oxygen inhibits PHD catalytic activity, leading to HIF1α stabilization, dimerization with HIF1β, and upregulation of numerous target genes involved in the cancer cell response to hypoxia (Kaufmann *et al.*, 2013; Kennel *et al.*, 2018). In two independent yeast two-hybrid assays, Balamurugan and colleagues, using PHD1 as bait, captured CDR2 from mouse and human testis cDNA

libraries. This interaction was further confirmed by co-immunoprecipitations from HeLa cells co-transfected with recombinant CDR2 and PHD1 proteins (Balamurugan *et al.*, 2009). In summary, this study demonstrated that CDR2 is highly expressed in papillary renal cell carcinoma (pRCC) and that its elevated levels are linked to the attenuation of the hypoxia response pathway, likely through the regulation of PHD1 protein abundance and HIF transactivation activity (Balamurugan *et al.*, 2009).

4.3.2 Calcium homeostasis

Calcium homeostasis is essential for cellular metabolism and mitochondrial stability, as its dysregulation can lead to neurodegeneration. (Bhosale *et al.*, 2015; Kinoshita-Kawada *et al.*, 2004; Schwaller, 2012). Intracellular calcium levels are tightly regulated through coordinated calcium influx and efflux mechanisms, as well as by cytoplasmic calcium-binding proteins such as calbindin D28K (CB) and the GoLoco domain protein Purkinje cell-specific protein-2 (L7/Pcp-2) (Kinoshita-Kawada *et al.*, 2004; Schwaller, 2012). L7/Pcp-2, in turn, modulates the activity of P/Q-type voltage-gated calcium channels (VGCC) (Gao *et al.*, 2012; Kinoshita-Kawada *et al.*, 2004; Todorov *et al.*, 2012). Consequently, any factor that perturbs CB or L7/Pcp-2 is likely to exert significant physiological and pathological effects on Purkinje cells (Schwaller, 2012).

Incubation of rat cerebellar organotypic slice cultures (cOTSC) with sera from PCD patients revealed that anti-Yo antibodies by binding to CDR2/L lead to alterations in mitochondrial and cytosolic calcium homeostasis, and increase reactive oxygen species (ROS) production—effects that are partly attributed to CB malfunction (Panja *et al.*, 2019; Schubert *et al.*, 2014). For instance, immunoprecipitation experiments from cerebellar lysates showed that endogenous CB protein interacts with CDR2, but not with CDR2L, suggesting a direct role for CDR2 in CB function (Schubert *et al.*, 2014). On the other hand, CDR2L has been associated with plasma membrane signaling events involving P/Q-type VGCC and AMPA receptor-mediator calcium regulation (Panja *et al.*, 2019). Internalization of anti-Yo disrupts the calcium-dependent VGCC-Protein kinase C-CB signaling pathway, leading to calpain-2 overactivation. Consequently, this affects respiratory chain complex I, increases ROS production, reduces mitochondrial membrane potential, and impairs respiration. Additionally, it alters calcium influx and anion efflux in mitochondrial and plasma membranes, compromising the cell's ability to counteract calcium overload (Panja *et al.*, 2019).

4.3.3 mRNA Transport

CEN, the ortholog of CDR2/L in *D. melanogaster*, shares around 60% similarity with CDR2/L within the first predicted coiled-coil region. It is predominantly expressed in ovaries and early embryos, with its expression gradually decreasing during embryonic and larval development (Kao & Megraw, 2009). CEN was initially identified due to its direct interaction with centrosomin (CNN), an essential scaffolding protein in the pericentriolar material (PCM) (Kao & Megraw, 2009). Kao and Megraw reported that CEN exhibits asymmetric localization at peri-centrosomal foci and cleavage furrows, and that CEN mutants display mitotic errors and embryonic lethality (Kao & Megraw, 2009). *Cen* mRNA forms micron-scale RNA-binding granules around centrosomes, which also contain CEN protein and the fragile-X mental retardation protein (FMRP), a negative regulator of *cen* mRNA translation (Ryder *et al.*, 2020). FMRP is an RNA-binding protein that plays a key role in mRNA transport, stability, and translational regulation, particularly in neurons. Its dysregulation is associated with the neurodevelopmental disorder Fragile X syndrome (FXS) (Richter & Zhao, 2021). FMRP regulates both the localization and steady-state levels of *cen* mRNA and CEN protein at centrosomes. Additionally, localization of *Cen* mRNA depends on the maintenance of intact polysomes, and its transcript undergoes localized translation at centrosomes (Bergalet *et al.*, 2020; Ryder *et al.*, 2020). As a result, the mislocalization of *cen* mRNA disrupts CEN protein localization at centrosomes, leading to centrosome separation defects, microtubule disorganization, DNA damage, and embryonic lethality (Ryder *et al.*, 2020). Recent findings indicate that although an N-terminal CEN fragment is sufficient for targeting the protein to the centrosome, it is insufficient for the formation and localization of *cen* mRNA granules (Zein-Sabatto *et al.*, 2024, Preprint). Additionally, the authors identified a CC1 box domain within CEN N-terminus that binds DLIC, purposing a model wherein dynein directly binds CEN, as it emerges from ribosomes, activating the dynein motor complex and directing CEN protein and *cen* mRNA to centrosomes (Zein-Sabatto *et al.*, 2024, Preprint).

Table 2 – CDR2 and CEN potential functions and interactors reported in literature.

Potential function	Potential interactor	References
CDR2		
	c-MYC	(Okano *et al.*, 1999)
	MRGX and MRG15	(Sakai *et al.*, 2002, 2004)
Gene expression & regulation	PHD1	(Balamurugan *et al.*, 2009)
	eIF4A3 and SON	(Herdlevær *et al.*, 2020)
	SON	(Herdlevær *et al.*, 2020)
Protein synthesis	RpS6	(Herdlevær *et al.*, 2020)
Calcium homeostasis	CB	(Panja *et al.*, 2019; Schubert *et al.*, 2014)
CEN (*D. melanogaster)*		
mRNA transport	CNN	(Kao & Megraw, 2009; Zein-Sabatto *et al.*, 2024, Preprint)

CHAPTER II.

AIMS

AIMS

The molecular motor complex dynein is responsible for the majority of intracellular transport that is directed toward the minus ends of microtubules. A central question is how the single dynein motor is recruited to its diverse cargo, which includes membrane-bound organelles. In recent years, an increasing number of cargo-specific adaptor proteins have been identified that use conserved motifs to co-recruit dynein and its obligatory activator dynactin.

In this thesis, two new dynein adaptors are presented and their role is explored in a human cancer cell line. Through *in silico* analysis, CDR2 and its paralog CDR2L were identified as containing a conserved dynein-binding motif (CC1 box). CDR2 and CDR2L are onconeural antigens associated with PCD, but their physiological roles remain unclear. Therefore, the aims of this study were:

1 Dissection of the dynein-dynactin-CDR2/CDR2L transport machine

- Assess whether CDR2 and CDR2L directly bind to dynein and dynactin, and evaluate the significance of their CC1 box motif in mediating this interaction *in vitro;*
- Evaluate the ability of CDR2 and CDR2L to act as activating adaptors of the dynein-dynactin transport machine by performing *in vitro* motility assays. Protein expression and purification of dynein, dynactin and LIS1, as well as the *in vitro* TIRF motility assays, were performed by Kashish Singh in the laboratory of Andrew P. Carter at the MRC Laboratory of Molecular Biology (Cambridge, United Kingdom).

2 Identification of dynein cargo transported by CDR2/CDR2L

- Generate stable cell lines expressing GFP::3xFLAG::CDR2 and GFP::3xFLAG::CDR2L at near-endogenous levels, enabling immunoprecipitation of CDR2/CDR2L and identification of associated proteins via mass spectrometry;
- Explore the interaction of CDR2/CDR2L with identified cargo proteins using *in vitro* assays and cell lines;

3 Address the functional role of CDR2/CDR2L in cells

- Generate CDR2/CDR2L single and double KO cell lines using CRISPR/Cas9-mediated genome editing, and characterize phenotypes using techniques such as transient transfections, immunofluorescence, live-imaging and EM.

CHAPTER III.

MATERIALS AND METHODS

MATERIALS AND METHODS

DNA constructs

Tissue culture

For transient expression of CDR2, CDR2L, eEF1Bβ and JIP3, cDNA was inserted into a pcDNA5-FRT-TO-based vector (Invitrogen) modified to contain N-terminal Myc::eGFP::TEV::S-peptide. KTN1 was inserted into pcDNA5-FRT-TO-based vector modified to contain C-terminal 3xFLAG tag (Table 3). To generate cell lines stably expressing GFP::3xFLAG-tagged CDR2 and CDR2L, cDNA for 3xFLAG::CDR2 and 3xFLAG::CDR2L was inserted into pLenti-CMV-GFP-Hygro (Addgene 17446) (Table 3). To generate CDR2/CDR2L single and double KO cells by CRISPR/Cas9, protospacer sequences targeting CDR2 and CDR2L (Table 5) were inserted into the BsmBI sites of pLenti-sgRNA (Addgene 71409) or pKM808 (Addgene 134181) (Table 3).

Biochemistry

For bacterial expression of CDR2, CDR2L, eEF1Bβ, and KTN1 fragments, cDNA was inserted into a 2CT vector containing an N-terminal 6xHis::maltose binding protein (MBP) followed by a TEV protease cleavage site (TEVsite) and C-terminal Strep-tag II (StTgII), or into pGEX-6P-1 containing N-terminal glutathione S-transferase (GST) followed by a PreScission protease cleavage site (PPsite) and C-terminal 6xHis (Table 3). DLIC1 (pGEX-6P-1), JIP3 (2CT) and KIF5C (pGEX-6P-1) constructs were already available in my host laboratory collection.

Protein residue numbers in text and figures refer to the following UniProt entries Q01850 (CDR2_HUMAN), Q86X02 (CDR2L_HUMAN), Q9Y6G9 (DC1L1_HUMAN), Q14204 (DYHC1_HUMAN), P29692 (EF1D_HUMAN), Q9UPT6 (JIP3_HUMAN), P28738 (KIF5C_MOUSE) and Q86UP2 (KTN1_HUMAN).

General cloning

Site-Directed Mutagenesis

To introduce or remove single nucleotides in a plasmid of interest (Table 3), site-directed mutagenesis was performed by PCR amplification of the entire plasmid using primers carrying the desired modification. The 50 µL PCR reaction contained 1× GC buffer, 5 mM dNTPs, 5% DMSO, 500 nM of each primer, 1 Unit (U) Phusion high-fidelity DNA polymerase (APExBio or homemade), and 50 ng of plasmid DNA. PCR cycling conditions included an initial denaturation at 98 °C, followed by 35 cycles of 98 °C for 30 (s), primer-specific annealing temperature for 30 s, and extension at 72 °C for 30 s/kilobase (kb), with a final

extension step at 72 °C for 5 minutes (min). Following amplification, the parental methylated plasmid was digested with *Dpn*I at 37 °C for 1 hour (h). The PCR product was then purified (see *DNA Purification* section). For circularization, 50 ng of the purified product were phosphorylated and ligated using 400 U T4 DNA ligase (New England Biolabs), 10 U T4 polynucleotide kinase (PNK; Thermo Fisher Scientific), and 1× T4 DNA ligase buffer (New England Biolabs). Ligation was carried out either overnight at 4 °C or for 2 h at 25 °C. Prior to bacterial transformation (see *Competent cells transformation and colonies screening* section), the ligase was inactivated by incubation at 65 °C for 10 min.

Restriction Digestion and Ligation of DNA

Plasmids and PCR fragments were digested with the appropriate restriction enzymes (Fermentas FastDigest®) at 37 °C for 1 h. To clone KTN1(1–1357)::StTgII and eEF1Bβ(30–127)::StTgII, gBlocks containing the respective sequences and restriction sites were ordered from Integrated DNA Technologies (IDT, Leuven, Belgium) (Table 3). Backbone plasmid DNA was additionally treated with 1 U of Rapid alkaline phosphatase (Thermo Fisher Scientific) at 37 °C for 30 min. Digestion products were purified (see *DNA Purification* below) and ligation reactions were performed using a plasmid-to-insert ratio of 1:3 or 1:5, either overnight at 4 °C or for 2 h at 25 °C, in the presence of 400 U T4 DNA Ligase (New England Biolabs). Prior to bacterial transformation (see *Competent cells transformation and colonies screening* section), the ligase was inactivated by incubation at 65 °C for 10 min.

Gibson Assembly

Gibson assembly was used for plasmid engineering (Table 3), allowing the assembly of several DNA fragments in an isothermal single reaction (Gibson *et al.*, 2009). Each DNA fragment included an overlap of 20–40 base pairs (bp). The reaction relies on three enzymes—T5 exonuclease, a high-fidelity DNA polymerase, and DNA ligase—combined in an isothermal reaction buffer (IRB: 25% (weight/volume (w/v)) PEG-8000, 500 mM Tris-HCl pH 7.5, 50 mM $MgCl_2$, 50 mM DTT, 1 mM each dNTP, and 5 mM NAD). The T5 exonuclease (New England Biolabs) resects the 5’ ends, the Phusion polymerase (APExBio) fills in gaps, and the DNA ligase (New England Biolabs) seals nicks. Gibson assembly reactions were freshly prepared using nuclease-free water, 5× IRB, Taq DNA ligase (40 U/μL), T5 exonuclease (1 U/μL), and Phusion polymerase (2 U/μL), and incubated at 50 °C for 1 h. An amount between 100–200 ng of predicted assembled DNA was transformed into competent bacteria (see *Competent cells transformation and colonies screening* section).

Target Guide Sequence Cloning

To generate sgRNAs for CDR2 and CDR2L KO, I followed the *Target Sequence Cloning Protocol* developed by the Zhang Laboratory (MIT & Broad Institute) (Sanjana *et al.*, 2014; Shalem *et al.*, 2014). Briefly, a pair of oligonucleotides (20 bp target sequence plus specific overhangs) was designed, phosphorylated, and annealed in a reaction containing 1× T4 DNA ligase buffer (New England Biolabs), 0.5 U PNK (Thermo Fisher Scientific), and 10 µM of each oligonucleotide. The mixture was incubated at 37 °C for 30 min, followed by 95 °C for 5 min, and gradually cooled to 25 °C at a rate of 5 °C/min. Phosphorylated and annealed oligonucleotides were cloned into either the pLenti-sgRNA or pKM808 backbone plasmid, previously digested with Esp3I. Ligation was performed using 400 U of T4 DNA ligase (New England Biolabs), 50 ng of digested plasmid, and a 1:200 dilution of the oligonucleotides. The reaction was incubated either overnight at 4 °C or for 2 h at 25 °C. The ligation mix was treated with 1 U of T5 exonuclease (New England Biolabs) at 37 °C for 30 min (this step is optional). Prior to transformation into competent bacteria (see *Competent cells transformation and colonies screening* section), the reaction was heat-inactivated at 65 °C for 10 min

DNA Purification

PCR products were purified using the NucleoSpin Gel and PCR Clean-up Kit (Macherey-Nagel). In some cases, PCR reactions were directly purified. In other cases, DNA fragments were separated by electrophoresis on 0.8% agarose gels containing GreenSafe (NZYtech; 1 µL per 100 mL of tris-acetate-EDTA (TAE) buffer) in TAE buffer (40 mM Tris, 20 mM glacial acetic acid, 1 mM EDTA, pH 8). Gels were visualized using a Gel Doc system (Bio-Rad) and bands of interest were excised with a scalpel under ultraviolet (UV) light. Gel-extracted DNA was then purified using the same kit, following the manufacturer's instructions.

Table 3 – Plasmids constructed and used in the course of this work.

"S-pt" denotes the *S-peptide sequence*. "Seq" stands for *Sequence*.

Description	Backbone vector	Cloning strategy
Expression in cells		
Myc::eGFP::TEVsite::S-pt::CDR2(1–454)	pcDNA5-FRT-TO	Restriction
Myc::eGFP::TEVsite::S-pt::CDR2(1–454) Δ23–39	pcDNA5-FRT-TO	Ligation
Myc::eGFP::TEVsite::S-pt::CDR2(1–420)	pcDNA5-FRT-TO	Ligation
Myc::eGFP::TEVsite::S-pt::CDR2(404–454)	pcDNA5-FRT-TO	Ligation
Myc::eGFP::TEVsite::S-pt::CDR2(Δ414–446)::eEF1Bβ(34–66)	pcDNA5-FRT-TO	Ligation
Myc::eGFP::TEVsite::S-pt::JIP3(2–185)::CDR2(186–454)	pcDNA5-FRT-TO	Gibson assembly
Myc::eGFP::TEVsite::S-pt::CDR2L(1–465)	pcDNA5-FRT-TO	Restriction
Myc::eGFP::TEVsite::S-pt::CDR2L(1–465) Δ23–39	pcDNA5-FRT-TO	Ligation
Myc::eGFP::TEVsite::S-pt::CDR2L(1–415)	pcDNA5-FRT-TO	Ligation
Myc::eGFP::TEVsite::S-pt::CDR2L(416–465)	pcDNA5-FRT-TO	Ligation
KTN1(1–1357)::3xFLAG	pcDNA5-FRT-TO	Restriction
KTN1(1–1357 Δ1114–1153)::3xFLAG	pcDNA5-FRT-TO	Ligation
CDR2 – sgRNA exon 1	pLenti-sgRNA	Target guide seq
CDR2 – sgRNA exon 3	pKM808	Target guide seq
CDR2L – sgRNA exon 1	pLenti-sgRNA	Target guide seq
GFP::3xFLAG::CDR2(1–454)	pLenti-CMV-GFP-Hygro	Restriction
GFP::3xFLAG::CDR2(1–454)	pLenti-CMV-GFP-Hygro	Restriction
Protein expression		
6xHis::MBP::TEVsite::CDR2(1–146)::StTgII	2CT	Ligation
6xHis::MBP::TEVsite::CDR2(1–146) Δ23–39::StTgII	2CT	Ligation
6xHis::MBP::TEVsite::CDR2(1–146) HBS1_6A::StTgII	2CT	Ligation
6xHis::MBP::TEVsite::CDR2L(1–159)::StTgII	2CT	Ligation
6xHis::MBP::TEVsite::CDR2L(1–290)::StTgII	2CT	Ligation
6xHis::MBP::TEVsite::CDR2L(1–290) Δ23–39::StTgII	2CT	Ligation
GST::PPsite::CDR2(411–454)::6xHis	pGEX-6P-1	Ligation
6xHis::MBP::TEVsite::KTN1(991–1357)::StTgII	2CT	Restriction
6xHis::MBP::TEVsite::KTN1(991–1357) Δ1114–1153::StTgII	2CT	Restriction
GST::PPsite::eEF1Bβ(30–66)::6xHis	pGEX-6P-1	Ligation
6xHis::MBP::TEVsite::eEF1Bβ(30–127)::StTgII	2CT	Restriction
GST::PPsite::CDR2(137–340)	pGEX-6P-1	Restriction
GST::PPsite::CDR2L(137–347)	pGEX-6P-1	Restriction

Competent cells transformation and colonies screening

Plasmid DNA was gently added to 100 µL of *Escherichia coli* DH5α chemically competent cells (homemade) and incubated on ice for 20 min. Cells were then heat-shocked at 42 °C for 1 min and immediately returned to ice for 2 min. For recovery, 0.5 mL of super optimal broth with catabolite repression medium (SOC; homemade; 2% tryptone, 0.5% yeast extract, 1% of 1M NaCl, and 0.25% of 1M KCl) was added, followed by incubation at 37 ºC for 1 h in a shaker incubator. Cells were then centrifuged at 850 rcf for 3 min, the supernatant was mostly removed, and the pellet resuspended. The full volume was plated on prewarmed selective agar plates using a sterile spreader and incubated overnight at 37 °C. Between 3 and 8 colonies (depending on the complexity of the assembly) were picked and grown overnight in 3–5 mL Luria-Bertani (LB) medium with the appropriate antibiotic at 37 °C with shaking. Plasmid DNA was extracted using the NucleoSpin® Plasmid Mini-Prep Kit (Macherey-Nagel) following the manufacturer's instructions. Extracted plasmids were analyzed by restriction digestion and Sanger sequencing.

Protein expression

For expression of CDR2, CDR2L, DLIC1, eEF1Bβ, JIP3, KIF5C and KTN1 fragments, plasmids were transformed into the *E. coli* Rosetta strain. Single colonies were grown in 10 mL LB medium overnight at 37 °C in a shaking incubator. 10 mL of saturated culture were diluted into 1 L and incubated at 30 °C until an OD600 of 0.5. Expression was induced with 0.1 mM IPTG and cultures were grown overnight at 18 °C. Cells were harvested by centrifugation at 4,000 rcf for 15 min at 4 °C in a Mega Star 4.0R centrifuge with TX-1000 rotor (Avantor), and cell pellets were stored at −80 °C.

Protein purification

For purification of CDR2, CDR2L, JIP3, KTN1, and eEF1Bβ fragments with a C-terminal StTgII, bacterial pellets from 1 L expression were resuspended in 30 mL lysis buffer A (20 mM Tris-HCl pH 8, 300 mM NaCl, 10 mM imidazole, 1 mM DTT) supplemented with 1 mM PMSF and 2 mM benzamidine-HCl. Cells were lysed with a cell cracker, and the lysate was cleared twice by centrifugation at 40,000 rcf for 20 min each at 4 °C using a JA 25.50 rotor (Beckman Coulter). The cleared lysate was incubated with 2 mL Ni-NTA resin (Thermo Fisher Scientific) for 1 h at 4 °C, transferred to a gravity flow column (Pierce), and washed with 150 mL wash buffer A (20 mM Tris-HCl pH 8, 300 mM NaCl, 20 mM imidazole, 0.1% (v/v) Tween 20, 1 mM DTT) supplemented with 2 mM benzamidine-HCl. Proteins were eluted with 10 mL elution buffer A (20 mM Tris-HCl pH 8, 300 mM NaCl, 250 mM imidazole, 1 mM DTT) and incubated overnight at 4 °C with 130 µg TEV protease. Cleaved proteins were incubated with 2 mL Strep-Tactin Sepharose resin (IBA) for 1 h at 4 °C, transferred to

a gravity flow column, washed with 2 × 50 mL wash buffer B (20 mM Tris-HCl pH 8, 300 mM NaCl) and 50 mL wash buffer C (20 mM Tris-HCl pH 8, 150 mM NaCl), and eluted with 10 mL elution buffer B (100 mM Tris-HCl pH 8, 150 mM NaCl, 10 mM d-desthiobiotin). Proteins were concentrated and loaded onto a Superdex 200 Increase 10/300 GL column pre-equilibrated with storage buffer A (25 mM HEPES pH 7.5, 150 mM NaCl, 1mM DTT). Peak fractions were pooled and concentrated, glycerol was added to 10% (v/v), and aliquots were flash frozen in liquid nitrogen and stored at −80 °C.

For purification of CDR2, DLIC1, eEF1Bβ, and KIF5C fragments with an N-terminal GST and C-terminal 6xHis tag, bacterial pellets from 1 L expression were lysed and proteins were purified with Ni-NTA resin, as described above. After elution from Ni-NTA resin, proteins were incubated with 2 mL Pierce Glutathione Agarose resin (Thermo Fisher Scientific) for 1 h at 4°C, transferred to a gravity flow column, washed with 2 × 50 mL wash buffer B and 50 mL wash buffer C. Proteins were eluted with 10 mL elution buffer C (25 mM HEPES pH 7.5, 150 mM NaCl, 10 mM reduced L-glutathione). For KIF5C, L-glutathione was removed with an Econo-Pac 10DG column (Bio-Rad) by buffer exchange into storage buffer, and the protein was concentrated, flash frozen and stored at −80 °C, as described for StTgII proteins. All other proteins were concentrated and loaded onto a Superdex 200 Increase 10/300 GL column pre-equilibrated with storage buffer. Peak fractions were pooled, concentrated, flash frozen and stored at −80 °C, as described for StTgII proteins

Table 4 – List of proteins expressed and purified in the course of this work.

"AC" denotes Affinity chromatography.

Protein	Purification steps
6xHis- and StTgII-tagged proteins	
CDR2(1–146)::StTgII	6xHis AC; TEV cleavage; StTgII AC; SEC
CDR2(1–146) Δ23–39::StTgII	6xHis AC; TEV cleavage; StTgII AC; SEC
CDR2(1–146) HBS1_6A::StTgII	6xHis AC; TEV cleavage; StTgII AC; SEC
CDR2L(1–159)::StTgII	6xHis AC; TEV cleavage; StTgII AC; SEC
CDR2L(1–290)::StTgII	6xHis AC; TEV cleavage; StTgII AC; SEC
CDR2L(1–290) Δ23–39::StTgII	6xHis AC; TEV cleavage; StTgII AC; SEC
KTN1(991–1357)::StTgII	6xHis AC; TEV cleavage; StTgII AC; SEC
KTN1(991–1357) Δ1114–1153::StTgII	6xHis AC; TEV cleavage; StTgII AC; SEC
eEF1Bβ(30–127)::StTgII	6xHis AC; TEV cleavage; StTgII AC; SEC
GST- and 6xHis-tagged proteins	
GST::PPsite::CDR2(411–454)::6xHis	6xHis AC; GST AC; SEC
GST::PPsite::DLIC1(388–523)::6xHis	6xHis AC; GST AC; SEC
GST::PPsite::DLIC1(388–523_F447A/F448A)::6xHis	6xHis AC; GST AC; SEC
GST::eEF1Bβ(30–66)::6xHis	6xHis AC; GST AC; SEC
GST::PPsite::KIF5C(807–956)::6xHis	6xHis AC; GST AC
GST-tagged proteins	
GST::PPsite::CDR2(137–340)	GST AC; PreScission cleavage;
GST::PPsite::CDR2(137–340)	GST AC; PreScission cleavage;

GST pull-downs

Proteins were mixed in a total of 20 µL pull-down (PD) buffer A (25 mM HEPES pH 7.5, 150 mM NaCl, 5 mM DTT) in a 1.5-mL tube. For *Figure 7C* and *Figure S4B*, 250 pmol of each protein were added. For *Figure 11C*, 150 pmol of CDR2 and KTN1-C fragments and 3 nmol of the eEF1Bβ fragment were added. After incubation at room temperature for 30 min, 4 µL were removed from the mixture and added to a tube containing 23 µL PD buffer A and 9 µL 4× SDS-PAGE sample buffer (200 mM Tris-HCl pH 6.8, 40% (v/v) glycerol, 8% (w/v) SDS, 400 mM DTT, 0.4% (w/v) bromophenol blue) ("Input"). To the remaining 16 µL protein mixture, 30 µL of a 50% slurry of Pierce Glutathione Agarose resin/PD buffer A were added and the resin/protein mixture was rotated horizontally for 30 min. The resin was washed quickly with 3 × 500 µL PD buffer A using 15-s spins in a microfuge (Roth), all buffer was removed with a gel loading tip, and the resin was incubated with 50 µL elution buffer C for 15 min with rotation. The resin was pelleted at 20,000 rcf for 1 min in an Eppendorf 5424

centrifuge, 36 µL of the eluate were removed and added to a tube containing 12 µL 4× SDS-PAGE sample buffer, and the sample was heated for 1 min at 95 °C ("GST pull-down"). 7 µL of "Input" and "GST pull-down" samples were separated by 14% SDS-PAGE and proteins were visualized with BlueSafe stain (NZYTech).

For the binding competition experiments (Figure 11C), the amount of KTN1-C in the pull-downs was quantified using Fiji software. The final integrated intensity of the KTN1-C band was calculated by subtracting the integrated intensity of a background region of the same size below the band. Data were plotted as the ratio of KTN-C band intensity in the presence *vs.* absence of eEF1Bβ (+/- eEF1Bβ).

Strep-Tag II pull-downs from porcine brain lysate

Porcine brain lysate was prepared as described previously (McKenney *et al.*, 2014). In brief, fresh brains were broken into small chunks, flash-frozen in liquid nitrogen, and stored at −80 °C. Frozen brain chunks were homogenized in equal w/v of buffer (50 mM HEPES pH 7, 50 mM PIPES, 1 mM EDTA, and 2 mM MgSO4, 1 mM DTT) using a waring blender, followed by glass pestle grinding. After clarification at 34,000 rcf for 45 min at 4 °C using a JA 25.50 rotor, the crude homogenate was flash frozen in 1-mL aliquots and stored at −80 °C.

For pull-downs, 250 pmol of purified protein were added to 15 µL Strep-Tactin Sepharose resin pre-equilibrated in 100 µL PD buffer B (30 mM HEPES pH 7.5, 50 mM KAc, 2 mM Mg(Ac)2, 1 mM EGTA, 10% (v/v) glycerol, 0.1% (v/v) NP-40, 5 mM DTT) in a 1.5-mL tube and incubated for 30 min at room temperature. Porcine brain lysate was thawed, supplemented with 1 mM PMSF, and cleared at 20,000 rcf for 10 min at 4 °C in a Megafuge 8R (Eppendorf). 1 µL was removed from the cleared lysate, added to a tube containing 39 µL 1× SDS-PAGE sample buffer, and heated for 3 min at 95 °C ("Brain lysate"). 300 µL PD buffer B and 100 µL brain lysate were added to the protein/resin mixture (total volume ~500 µL) and incubated with rotation for 1 h at 4 °C. The resin was washed quickly with 3 × 500 µL ice-cold PD buffer B using 15-s spins in a microfuge, all buffer was removed with a gel loading tip, and the resin was incubated with 50 µL elution buffer B for 15 min at room temperature with rotation. The resin was pelleted at 20,000 rcf for 1 min in an Eppendorf 5424 centrifuge, 36 µL of the eluate were removed, added to a tube containing 12 µL 4× SDS-PAGE sample buffer, and the sample was heated for 1 min at 95°C ("StTgII pull-down"). 8 µL of "Brain lysate" and "StTgII pull-down" samples were separated by 12% SDS-PAGE and visualized with BlueSafe stain, and 10 µL were separated by 12% SDS-PAGE and processed for immunoblotting, as described below (see *Immunoblotting* section).

Size exclusion chromatography to assess protein complex formation

4 nmol (Figure 8E; Figure 11B) or 8 nmol (Figure 7B; Figure S1C) of each protein were diluted with storage buffer to a final volume of 200 µL in a 1.5-mL tube, corresponding to final concentrations of 20 µM and 40 µM, respectively. After incubation at room temperature for 30 min, samples were cleared in a Megafuge 8R at 20,000 rcf for 10 min at 4 °C and loaded onto a Superdex 200 Increase 10/300 GL column. Size exclusion chromatography (SEC) was performed at room temperature on an ÄKTA Pure 25L1 system at a flow rate of 0.5 mL/min. 0.5-mL fractions were collected and protein elution was monitored at 280 nm. 30 µL were removed from each fraction and added to a tube containing 10 µL 4× SDS-PAGE sample buffer. Samples were heated for 1 min at 95 °C, and 5 µL were separated by 14% SDS-PAGE. Proteins were visualized by BlueSafe staining.

Production of CDR2 and CDR2L antibodies

Affinity-purified rabbit polyclonal antibodies against a divergent region between CDR2 (residues 137–340) and CDR2L (residues 137–347) were generated as described in Desai *et al.* (2003). In brief, GST::CDR2(137–340) and GST:CDR2L(137–347) were expressed in *E.coli*, purified using glutathione agarose resin (Thermo Fisher Scientific), and injected into rabbits (GeneCust). Serum was sequentially passed over two separate HiTrap N-hydroxysuccinimide (NHS) columns (GE Healthcare): first coupled to GST, and then to GST::CDR2(137–340) or GST::CDR2L(137–347) for affinity purification.

Protein expression and purification for rabbit injection

CDR2(137–340) and CDR2L(137–347) were cloned into the pGEX-6P-1 (containing N-terminal GST followed by a PreScission protease cleavage site) using restriction enzyme-based cloning (see *Restriction Digestion and Ligation of DNA* section). For expression, plasmids were transformed into the *E. coli* Rosetta strain. Single colonies were grown in 50 mL LB medium with 100 µg/mL ampicillin and 50 µg/mL chloramphenicol (rare codons of Rosetta strain are in a chloramphenicol resistant plasmid) overnight at 37 °C in a shaking incubator. 10 mL of saturated culture were diluted into 1 L (3 L in total were prepared) and incubated at 30 °C until an OD_{600} of 0.5. Expression was induced with 0.1 mM IPTG and cultures were grown overnight at 18 °C. Cells were harvested by centrifugation at 4,000 rcf for 25 min at 4 °C in a Mega Star 4.0R centrifuge with TX-1000 rotor (Avantor), and cell pellets were stored until protein purification at −80 °C.

For purification, bacterial pellets were resuspended in 30 mL lysis buffer B (1× PBS pH 7.4, 250 mM NaCl, 10 mM EGTA, 10 mM EDTA, 0.1% (v/v) Tween-20) supplemented with 1 mM PMSF and 2 mM benzamidine-HCl. Lysozyme was added to a final concentration of 1 mg/mL and incubated on ice for 15 min. Cells were lysed by sonication (output settings

4–6, 50% duty cycle, 4 × 30 s pulses with 1 min intervals, on ice). The lysate was cleared by centrifugation at 40,000 rcf for 30 min at 4 °C using a JA 25.50 rotor (Beckman Coulter). The cleared lysate was incubated with 2 mL Pierce Glutathione Agarose resin (Thermo Fisher Scientific) for 1 h at 4 °C. The resin was washed with 4 × 50 mL wash buffer D (1× PBS, 250 mM NaCl, 0.1% (v/v) Tween-20, 1 mM DTT and 2 mM Benzamidine-HCl) for 5 min. After draining the wash buffer using a poly-prep chromatography column (Bio-Rad), proteins were eluted with 1 mL of elution buffer D (50 mM Tris pH 8.0, 75 mM KCl, 15 mM reduced glutathione) and 20 fractions (total 5 bed volumes, ~4 mL) were collected. After SDS-PAGE analysis, desired fractions were pooled to a final volume of 3 mL. Protein concentration was determined and 5× 500 µL aliquots of GST fusion proteins (1 mg/mL) were sent to GeneCust company for rabbit immunization to generate antibodies against GST::CDR2(137–340) and GST::CDR2L(137–347).

Protein expression for antigen purification

After receiving the rabbit serum containing GST::CDR2(137–340) and GST::CDR2L(137–347) antibodies, GST::CDR2(137–340) and GST::CDR2L(137–347) proteins were re-expressed and purified to generate HiTrap NHS-activated columns for affinity purification of CDR2- and CDR2L-specific antibodies.

Given the high insolubility of CDR2(137–340), the GST tag was maintained to stabilize the protein, and a slightly modified purification protocol was used. GST::CDR2(137-340) was purified from a 3 L *E. coli* Rosetta culture. Cell pellets were resuspended in 60 mL lysis buffer C (50 mM HEPES pH 7.5, 250 mM NaCl, 10 mM EGTA, 10 mM EDTA, 0.1% (v/v) Tween-20) supplemented with 1 mM PMSF and 2 mM benzamidine-HCl. Lysozyme was added to 1 mg/mL and incubated for 15 min on ice. Before sonication, 5 mM DTT and 1.5% (w/v) sarkosyl were added to the lysate. The lysate was sonicated (output settings 4–6, 50% duty cycle, 4 × 30 s pulses with 1 min intervals, on ice) and cleared by centrifugation at 40,000 rcf for 40 min at 4 °C (JA 25.50 rotor, Beckman Coulter). Triton X-100 was added to a final concentration of 2% (v/v) to the cleared lysate and incubated for 10 min at 4 °C (to dissolve Triton X-100). The lysate was then incubated with 2 mL Pierce Glutathione Agarose resin (Thermo Fisher Scientific) for 1 h at 4 °C. The resin was washed with 4 × 50 mL wash buffer E (25 mM HEPES pH 7.5, 250 mM NaCl, 0.1% (v/v) Tween-20, 1 mM DTT, 2 mM benzamidine-HCl) for 5 min each. After draining the wash buffer, proteins were eluted with 10 mL elution buffer D (25 mM HEPES pH 7.5, 150 mM NaCl, 5 mM DTT, 15 mM reduced glutathione). Eluted proteins were dialyzed overnight at 4 °C against 5 L dialysis buffer (25 mM HEPES pH 7.5, 150 mM NaCl) using a magnetic stir bar set to gentle stirring.

For GST::CDR2L(137–347) purification, *E. coli* BL21 bacterial pellets from a 1 L expression culture were resuspended in 35 mL lysis buffer D (20 mM HEPES pH 7.5,

250 mM NaCl, 10 mM EGTA, 10 mM EDTA, 1 mM DTT) supplemented with 1 mM PMSF and 2 mM benzamidine-HCl. Cells were lysed using a cell cracker, 0.1% (v/v) Tween-20 was added, and the lysate was cleared by centrifugation at 40,000 rcf for 45 min at 4 °C (JA 25.50 rotor, Beckman Coulter). The subsequent purification steps were performed as described for GST::CDR2(137–340).

Desalting the antigen into coupling buffer and coupling to the NHS column

An Econo-Pac 10DG desalting column (BioRad) was washed with 30 mL water to remove phosphate from the storage buffer and prevent Ca^{2+} precipitation when using the coupling buffer (50 mM K-HEPES pH 8.0, 150 mM NaCl, 80 mM CaCl2). The column was then washed with 30 mL coupling buffer. After draining, 3 mL of GST::CDR2(137–340) or GST::CDR2L(137–347) were loaded onto the column and allowed to drain. Subsequently, 4 mL of coupling buffer were added, and the flow-through was collected—this was the desalted protein used for coupling to the HiTrap NHS column.

To couple the desalted antigen, a recirculation system was assembled onto the NHS-activated column, and the flow rate was set to 1.5 mL/min. First, a solution of ice-cold 1 M HCl was passed through the column for 2 min to activate the NHS groups. After activation, the desalted GST::CDR2(137–340) or GST::CDR2L(137–347) antigen was recirculated for 1 h at room temperature to covalently ligate to the column. To block any remaining reactive NHS groups, a blocking solution (0.5 M ethanolamine pH 8.3, 0.5 M NaCl) was circulated through the column for 5 min. The column was then sequentially washed with 10 mM Tris pH 8.0, 0.1 M glycine pH 2.0, 10 mM Tris pH 8.0, and 0.1 M triethylamine pH 11.5, for 5 min each. These washes were repeated once. Finally, the column was washed with PBS for 15 min and stored at 4 °C. Samples from pre- and post-desalting, as well as pre- and post-coupling, were analyzed by SDS-PAGE before proceeding to the next step.

Serum recirculation

The rabbit serum was thawed at 37 °C, and an equal volume of 2× PBS supplemented with 5 mM NaN3 was added. To remove any precipitates, the serum was filtered through 0.22 µm filters. After filtration, the serum was ready for recirculation and binding to the NHS columns. The serum was sequentially passed over two separate HiTrap NHS columns (GE Healthcare): first a GST-only column (available in my host laboratory) to remove anti-GST antibodies, and then a GST::CDR2(137–340) or GST::CDR2L(137–347) column for affinity purification of CDR2- or CDR2L-specific antibodies. For each column, the filtered serum was loaded into a tubing system connected to the NHS column, and the flow was set to 1.5 mL/min. The serum was recirculated overnight at room temperature. The following day, the column was washed with wash buffer F (1× PBS, 0.5 M NaCl, 0.1% (v/v) Triton X-100) for 2 h at room temperature, followed by a 30 min wash with PBS. Bound antibodies were

eluted by sequential elution with glycine pH 2.0 (acidic elution) and triethylamine pH 11.5 (basic elution). To neutralize the acidic glycine eluate, 200 µL of 2 M Tris pH 8.5 were immediately added to each acidic fraction. The OD280 of each fraction was measured, and fractions with OD280 > 0.1 were pooled together.

Dialysis

Affinity-purified antibodies were dialyzed overnight at 4 °C in 3 L of PBS with gentle stirring using a magnetic stir bar. The following morning, the PBS was replaced with fresh 3 L of PBS, and dialysis continued for an additional 8 h. After the second dialysis, the dialysis tubing was transferred to a new beaker containing 300 mL of PBS supplemented with 50% (v/v) glycerol, and stirred gently overnight at 4 °C. Dialyzed antibodies were centrifuged at 20,000 rcf for 30 min at 4 °C to remove any aggregates. The supernatant was transferred to a new tube, and the antibody concentration was determined by measuring the absorbance at 280 nm (OD280). Aliquots were flash-frozen in liquid nitrogen and stored at −80 °C.

HiTrap NHS Column Storage

The HiTrap NHS column used for affinity purification was prepared for storage to allow future reuse. The column was washed with PBS for 15 minutes, followed by PBS containing 50% (v/v) glycerol at a reduced flow rate of 0.5 mL/min for 5 minutes. After washing, column was securely capped and stored at –20 °C.

Cell culture

HeLa, HEK-293T and U2OS cells were maintained at 37 °C and 5% CO_2 in high glucose Dulbecco's modified Eagle's medium (DMEM) supplemented with 10% fetal bovine serum (FBS), GlutaMAX, and 1% penicillin/streptomycin (all reagents from Gibco). Cell lines were regularly tested for mycoplasma contamination by PCR.

Lentivirus production

HEK-293T cells were seeded 24 h prior to transfection in 6-well plates at a density of 7×10^5 cells/mL. Lentivirus were produced by co-transfecting cells with 1.2 µg transfer plasmid (pLenti-sgRNA or pKM808 containing protospacer sequences targeting CDR2 or CDR2L (Tables 3 and 5); pLenti-CMV-GFP-Hygro containing 3xFLAG::CDR2 or 3xFLAG::CDR2L (Table 3)), 0.3 µg envelope plasmid pMD2.G (Addgene 12259) and 1 µg packaging plasmid psPAX2 (Addgene 12260) using Lipofectamine 2000. The medium was changed 24 h after transfection. Culture supernatant containing the lentivirus was collected 72 h after transfection and stored for 24 h at −80 °C before transduction.

Table 5 – sgRNAs used to generate CDR2 and CDR2L single and double KO cell lines.

Gene	Exon	Single-guide recognition region 5'–3'
CDR2	1	GCTGGCGGAAAACCTGGTAG
	3	ACAATTAGACGTCACAGCAA
CDR2L	1	GCTGGTCGTACCAGGACTCC

CRISPR/Cas9-mediated genome editing and transgenic cell lines

To generate CDR2/CDR2L single and double KO cells, a HeLa cell line containing doxycycline-inducible human codon-optimized spCas9 was used (McKinley *et al.*, 2015). For transduction with lentivirus, 400 µL virus-containing supernatant were added to 5×10^5 cells suspended in 600 µL per well in a 24-well plate. Polybrene was added to a final concentration of 10 µg/mL, and the cell suspension was centrifuged in the 24-well plate at 1200 rcf (slow acceleration and deceleration) for 45 min at 37 °C in a Mega Star 4.0R centrifuge with a TX-1000 rotor. Viruses were removed 24 h later, and after a further 24 h, antibiotics (1 µg/mL puromycin or 5 µg/mL blasticidin S) were added for 6–10 days. Cas9 expression was then induced with 1 µM doxycycline for 3 days. Colonies derived from single cells were obtained by seeding 100 cells in a 10-cm dish and allowing colonies to grow for 15 days. Individual colonies were collected by small-scale trypsinization, and clones were expanded and screened by immunoblotting with antibodies against CDR2 and CDR2L. To confirm gene editing, the targeted region was PCR-amplified from genomic DNA (gDNA), purified, and subsequently sequenced. Single KO cells were generated first, and CDR2/L double KO cells were subsequently generated by targeting CDR2 in CDR2L KO cells.

To generate cells stably expressing GFP::3xFLAG-tagged CDR2 or CDR2L, CDR2/L double KO cells were infected with corresponding lentivirus and selected with 400 µg/µL hygromycin B for 12 days. Clonal lines were obtained as described above. Clones expressing GFP::3xFLAG::CDR2 or GFP::3xFLAG::CDR2L at levels similar to those of endogenous CDR2 and CDR2L in control cells were selected.

PCR-based validation of genome editing

gDNA was extracted from HeLa control and CDR2/L single and double KO cells using the Purogene® Core kit A (Qiagen), following the manufacturer's instructions. Genomic regions containing the sgRNA target sites were amplified by PCR. Reactions were set up with NZYTaq II 2× Green Master Mix (NZYtech), 500 nM of each primer, and 80–100 ng of gDNA. PCR cycling conditions were as follows: initial denaturation at 95 °C for 2 min; 35 cycles of denaturation at 98 °C for 30 seconds; annealing using a touchdown protocol

(starting 10 °C above the target annealing temperature and decreasing by 1 °C every 30 seconds until the final annealing temperature was reached); and extension at 72 °C for 1 min/kb. A final extension was carried out at 72 °C for 5 min. PCR products were resolved on 0.8% agarose gels. Bands of interest were excised, DNA was purified as described in the *DNA Purification* section, and samples were submitted for Sanger sequencing. Sequencing results were analyzed to confirm successful genome editing by identifying frameshift mutations or premature stop codons at or near the sgRNA target sites, which would disrupt CDR2 or CDR2L protein expression

Table 6 – Combination of primers used to screen CDR2/L single and double KO cell lines.

Gene	Exon	Forward primer sequence 5'–3'	Reverse primer sequence 5'–3'
	1	CCTAGAAGACCCAGCCGAGA	CCACTTACTGCGGGACACAC
CDR2	3	CTGACGAAGCAAGTGGAACT	CCCCTAGTCCTTCCTTGTCAG
	1–3	CCTAGAAGACCCAGCCGAGA	CCCCTAGTCCTTCCTTGTCAG
CDR2L	1	AGGAAGAGGAGTCCTGGTACG	CCTCCCAGCAAAACATGACG

Cell proliferation

HeLa control and CDR2/L double KO (two independent clones) cell lines were plated in standard media onto 6-well plates at a density of 1×10^5 cells per well, with six wells per cell line corresponding to the six days of cell counting. Cells were counted over a period of six days at 24-hour intervals. At each 24-hour time point, cells from a well were washed with PBS, trypsinized and counted using a Neubauer chamber. Two counts were performed at each time point and averaged. Total number of cells was plotted against time. Growth curves data were fitted to a non-linear growth model and doubling times were calculated using GraphPad Prism 10.

Cell cycle profile

Control and CDR2/L double KO cells were cultured in standard medium and grown to 80-90% confluency. At the time of detachment, cells were harvested, counted, and 1×10^6 cells were washed, pelleted, and resuspended in 0.7 mL PBS. Cells were fixed with 70% ethanol by adding 1.4 mL cold absolute ethanol and incubated at −20 ºC for 24 h. After fixation, cells were washed with PBS, treated with RNAse A (50 µg/mL; NZYtech), and

stained with propidium iodide (25 µg/mL; Sigma-Aldrich) at 37 ºC for 30 min in the dark. An unstained sample was included for gating purposes. Flow cytometry was performed using a BD Accuri™ C6 Plus cytometer using the blue laser (488 nm). FlowJO (version 10.8.1) was used to analyze the acquired data. Live, single cells were gated based on forward scatter area (FSC-A) *vs.* side scatter area (SSC-A) to exclude debris, and FSC-A *vs.* forward scatter height (FSC-H) to eliminate doublets. Cell cycle distribution was quantified by applying the Dean-Jett-Fox model, and the percentage of cells in each phase (G1, S, and G2/M) was calculated accordingly.

Time-lapse live-cell microscopy

Control and CDR2/L double KO cells were seeded in 35 mm high glass ibidi chambers coated with poly-*L*-lysine (1×10^6 cells per chamber) 24 h before imaging. 2 h before time-lapse live-cell imaging, cells were incubated in DMEM medium (high glucose, HEPES, no phenol red) supplemented with 10% FBS (GIBCO, Life Technologies) containing the SPY595-DNA cell-permeable dye (1:2000, Spirochrome). Time-lapse live-cell imaging was performed on a Nikon ECLIPSE Ti microscope equipped with an IRIS 9 (Photometrics) camera and an excitation optics system composed of a Spectra X LED light engine (Lumencor), all controlled by NIS Elements 5.4 software (Nikon). Imaging was conducted using a CFI Plan Apochromat Lambda D 40× NA 0.95 objective (Nikon) at 37 ºC and 5% CO_2. Five different positions were selected, and an image stack (four planes separated by 3 µm) was acquired every 3 min, spanning a total depth of 12 µm at each position for a total of 17 h.

Time-lapse live-cell imaging was used to measure cell cycle duration, time between nuclear envelope breakdown (NEBD) and anaphase onset (AOS), and to quantify cumulative mitotic and cell death indices. The mitotic index was calculated as the number of cells entering mitosis during imaging, divided by the initial cell count. The cell dead index was determined as the number of dead cells at the end of imaging, relative to the total population.

Transient expression

24 h prior to transfection, cells were seeded in a 24-well plate at 6×10^4 cells/well. For each well, 250 ng plasmid DNA and 0.75 µL Lipofectamine 2000 (Invitrogen) were combined in total of 100 µL Opti-MEM (Gibco) and incubated for 20 min at room temperature. The DNA–lipid complexes were then added to the well in a dropwise manner. After 24 h, cells were processed for immunofluorescence as described below (see *Immunofluorescence* section).

RNA interference

24 h prior to transfection, cells were seeded in a 24-well plate at 2×10^4 cells/well in medium without antibiotics. Cells were transfected with siRNAs (Dharmacon On-TARGETplus; Horizon Discovery) targeting KTN1 (SMARTpool J-010605-05-08), eEF1Bβ (SMARTpool J-011648-05-08), or Luciferase GL2 Duplex (D-001100-01) as a control. For each transfection, 1 µL of Lipofectamine RNAi-MAX (Invitrogen) and 50 nM of each siRNA were diluted in a total of 100 µL Opti-MEM and incubated for 20 min at room temperature. The siRNA-lipid complexes were then added in a dropwise manner to cells. After incubation for 6 h, the transfection mixture was replaced with fresh complete medium, and cells were processed for immunofluorescence or immunoblotting 72 h later.

Immunofluorescence

Cells grown on 13-mm round coverslips (No. 1.5H, Marienfeld) coated with poly-*L*-lysine were fixed with 4% paraformaldehyde (PFA), diluted from a 20% aqueous solution (Delta Microscopies), in PBS for 30 min at room temperature and permeabilized with 0.1% (v/v) Triton X-100 in PBS for 10 min. Autofluorescence was quenched with 20 mM glycine in PBS for 10 min, and cells were incubated with blocking solution (3% (w/v) BSA in PBS) for 30 min. Coverslips were placed in a humid chamber and cells were incubated overnight at 4 °C with the following primary antibodies diluted in blocking solution: mouse monoclonal anti-FLAG clone M2 (Merck F1804; 1:1000), rabbit monoclonal anti-KTN1 clone D5F7J (Cell Signaling Technology #13243; 1:100), rabbit polyclonal anti-CDR2 (Merck HPA023870; 1:200), mouse monoclonal anti-Climp63 clone G1/296 (MyBioSource MBS567120; 1:500), mouse monoclonal anti-GFP clone 9F9.F9 (Abcam ab1218; 1:500), rabbit monoclonal anti-Calnexin clone C5C9 (Cell Signaling Technology #2679; 1:100), mouse monoclonal anti-EF-1δ clone A-5 (Santa Cruz Biotechnology sc-393731; 1:200), mouse monoclonal anti-CETN3 clone 3E6 (Abnova H00001070-M01; 1:500), mouse monoclonal anti-GM130 (BD Transduction Laboratories 610822, 1:200), rabbit polyclonal anti-SEC16A (Atlas Antibodies HPA005684; 1:50). Coverslips were washed 3 × 5 min with PBS and incubated for 1 h at room temperature in blocking solution containing the following donkey polyclonal secondary antibodies conjugated to Alexa dyes (Jackson ImmunoResearch; 1:300): anti-mouse IgG Alexa 488 (715-545-150), anti-mouse IgG Alexa 594 (715-585-150), anti-rabbit IgG Alexa 488 (711-545-152) and anti-rabbit IgG Alexa 594 (711-585-152). Coverslips were washed 3 × 5 min in PBS, rinsed once in H_2O and mounted in ProLong Gold Antifade Mountant with DAPI (Thermo Fisher Scientific).

Cells were imaged on an Axio Observer microscope (Zeiss) equipped with an Orca Flash 4.0 camera (Hamamatsu) and an HXP 200C Illuminator (Zeiss), controlled by ZEN 2.3 software (Zeiss). Image stacks were acquired with a step size of 0.24 µm using a 63× NA

1.4 Plan-Apochromat objective. For presentation, images were pseudo-colored, cropped, and linearly adjusted for contrast using Fiji software (ImageJ2, version 2.14.0/1.54f). Images shown in figures correspond to individual images from a z-stack, unless stated otherwise. For quantification (Figure 9A, D, G; Figure 12C; Figure S3F), images were acquired randomly using identical settings for the different conditions in an experiment, and maximum intensity projections of z-stacks were used to score ER morphology. Cells were classified as having clustered ER if the signal was densely concentrated adjacent to the nucleus, extending along less than half of the nuclear circumference. Cells were classified as containing ER patches when they contained one or more irregularly shaped areas of at least 3 μm^2 with bright signal. Most CDR2/L double KO cells scored as "patchy" were well above this threshold, typically containing multiple patches of up to 15 μm^2 in size.

Immunoblotting

Cells grown in 24-well plates were collected by scraping with a pipette tip in 60 µL 1× SDS-PAGE sample buffer. Samples were heated for 3 min 95°C, vortexed, and centrifuged in an Eppendorf 5424 at 20,000 rcf for 5 min at room temperature. Proteins were resolved by 10 or 12% SDS-PAGE and transferred to a 0.2-µm nitrocellulose membrane (GE Healthcare). The membrane was blocked with 5% non-fat dry milk in TBS-T (20 mM Tris-HCl pH 7.5, 140 mM NaCl, 0.2% (v/v) Tween 20) for 1 h and probed overnight at 4 °C with the following primary antibodies diluted in 5% non-fat dry milk/TBS-T: mouse monoclonal anti-p150 clone 1/p150^{Glued} (BD Transduction Laboratories 610473; 1:2500), mouse monoclonal anti-DIC clone 74.1 (Dillman and Pfister, 1994; 1:5000), mouse monoclonal anti-GAPDH clone 1E6D9 (Proteintech 60004-1-Ig; 1:5000), mouse monoclonal anti-α-tubulin clone B-5-1-2 (Merck T5168; 1:5000), mouse monoclonal anti-EF-1δ clone A-5 (Santa Cruz Biotechnology sc-393731; 1:2000), rabbit monoclonal anti-KTN1 clone D5F7J (Cell Signaling Technology #13243; 1:2000), rabbit polyclonal anti-CDR2 (Merck HPA023870; 1:1000), rabbit polyclonal anti-CDR2L (Proteintech 14563-1-AP; 1:2000). The membrane was washed 4 × 7 min with TBS-T and incubated for 1 h at room temperature in 5% non-fat dry milk/TBS-T containing goat polyclonal anti-mouse IgG (115-035-003) or anti-rabbit IgG (111-035-003) coupled to horseradish peroxidase (Jackson ImmunoResearch; 1:10000). The membrane was washed again 4 × 7 min with TBS-T and incubated with Pierce ECL Western Blotting Substrate (Thermo Fisher Scientific 32106) or Clarity Western ECL Substrate (for CDR2 and CDR2L antibodies; Bio-Rad 1705061). Proteins were visualized using Amersham Hyperfilm ECL (Cytiva) or the Bio-Rad ChemiDoc XRS+ system controlled by Image Lab software.

The intensity of protein bands in images acquired by the ChemiDoc XRS+ system (Figure 12A; Figure S5C) was quantified using Fiji software. The final integrated intensity of the

band was calculated by subtracting the integrated intensity of a background region of the same size adjacent to the band. For *Figure 11A*, for each immunoblot, the eEF1Bβ signal was normalized to the α-tubulin signal, while KTN1 and CDR2 signals were normalized to the GAPDH signal. The normalized signal in the Luciferase RNAi condition was set to 1 in each experiment. For *Figure S5C*, CDR2 and CDR2L signals were normalized to GAPDH signal. The normalized signal in the G1/S condition was set to 1 in each experiment.

Immunoprecipitation and mass spectrometry

CDR2/L double KO cells (control) and CDR2/L double KO cells expressing GFP::3xFLAG::CDR2 or GFP::3xFLAG::CDR2L were grown to 90% confluency in 40 15-cm dishes. To each dish, 4 mL PBS with 3 mM EDTA were added for 5 min at room temperature, and cells were harvested with a cell scraper and collected into 50-mL tubes. Cells were pelleted at 185 rcf with slow deceleration for 5 min at 4 °C in a Mega Star 4.0R centrifuge with a TX-1000 rotor, washed sequentially with 50 mL PBS and 10 mL freezing buffer (50 mM HEPES pH 7.5, 100 mM KCl, 1 mM $MgCl_2$, 1 mM EGTA, 10% (v/v) glycerol and 0.05% (v/v) NP-40), resuspended in 1 mL freezing buffer, flash-frozen in liquid nitrogen in a dropwise manner, and stored at −80 °C.

Two replicate immunoprecipitations were performed per condition (on separate days). For each immunoprecipitation, half of the frozen cell droplets were thawed with 3 mL lysis buffer (freezing buffer supplemented with cOmplete EDTA-free protease inhibitor cocktail (1 tablet per 10 mL), 5 mM β-glycerophosphate, and 200 nM microcystin) in a 5-mL tube and lysed by sonication using a Branson sonifier 250 with a micro tip. The lysate was split equally into two 2-mL tubes and cleared at 20,000 rcf for 10 min at 4 °C in a Megafuge 8R. The cleared lysate was transferred to new 2-mL tubes containing 70 µL Anti-FLAG M2 affinity gel (Merck) pre-eluted with 0.1 M glycine pH 2.6 and equilibrated with lysis buffer. The resin/lysate mixture was rotated for 1 h at 4 °C, transferred to a gravity flow column, and the resin was washed with 3 × 1 mL ice-cold lysis buffer containing 300 KCl and with 2 × 1 mL lysis buffer/300 KCl without NP-40. Proteins were eluted with 3 × 150 µL 0.1 M glycine pH 2.6 into a 1.5-mL tube containing 150 µL 2 M Tris-Cl pH 8.5. Proteins were precipitated with 20% trichloroacetic acid overnight on ice.

For LC-MS, proteins were reduced, alkylated and digested with trypsin following the solid-phase-enhanced (SP3) sample preparation approach (Hughes *et al.*, 2019). Data were acquired on an Ultimate 3000 liquid chromatography system connected to a Q-Exactive mass spectrometer (Thermo Scientific), as described in Osório *et al.* (2021). Proteins were identified with Proteome Discoverer software v3.0.1.27 (Thermo Scientific) using the UniProt database (*Homo sapiens* proteome, 20,389 entries, 2022_05). Relative protein abundances between samples were determined using the label-free quantification

(LFQ) method. Only proteins with a minimum of two unique peptides or two razor peptides and an abundance count of at least 10 were considered.

Transmission electron microscopy

For TEM analysis, cells grown on 13-mm round poly-L-lysine-coated coverslips were fixed by adding to the culture medium an equal volume of 4% PFA (Electron Microcopy Sciences) and 5% glutaraldehyde (GTA) (Electron Microscopy Sciences) in 0.2 M cacodylate pH 7.4 for 15 min at room temperature. The fixation medium was removed, cells were further fixed with 2% PFA and 2.5% GTA in 0.1 M cacodylate pH 7.4 for 1 h and washed 3 times with 0.1 M cacodylate pH 7.4. Cells were incubated with 1% osmium tetroxide (Electron Microscopy Sciences) in 0.1 M cacodylate pH 7.4 for 1 h, washed 3 times with H_2O, incubated with 1% uranyl acetate (Electron Microscopy Sciences) for 30 min, washed again with H_2O, dehydrated through graded series of ethanol (50-70-80-100-100-100%), and embedded in Embed-812 resin (Electron Microscopy Sciences).

Ultrathin sections (70 nm) were cut on an RMC Ultramicrotome (PowerTome) using a diamond knife and recovered to 200 mesh nickel grids (Electron Microscopy Sciences), followed by post-staining with UranylLess (Electron Microscopy Sciences) and 3% lead citrate solution (Electron Microscopy Sciences) for 5 min each. Images were acquired at 80 kV on a JEM 1400 transmission electron microscope (JEOL) equipped with a PHURONA CMOS camera (EMSIS). For each condition (Figure 9B; Figure S3E), images were taken randomly in a section approximately corresponding to the central plane of cell nuclei.

Images captured at 3000–6000× magnification, enabling visualization of entire cells, were used for the quantification of ER sheet stacks (Figure 9B; Figure S3E). For each cell, the stack containing the greatest number of sheets was identified, and the number of stacked sheets was documented. Each condition was repeated three times with 40–50 cells scored per replicate.

Correlative light–electron microscopy

Cells were grown in 35-mm glass bottom dishes (P35G-1.5-14-C-Grid, MatTeK) coated with poly-*L*-lysine. Cells were fixed with PFA and GTA as described for TEM, washed with PBS, permeabilized with 0.1% (w/v) saponin in PBS for 10 min, and incubated in PBS/0.1% saponin containing 20 mM glycine for 10 min. Cells were then incubated in blocking solution (see *Immunofluorescence* section) supplemented with 0.1% saponin for 30 min at room temperature. Anti-KTN1 antibody (see *Immunofluorescence* section) was diluted in the same solution and added to cells overnight at 4 °C in a humid chamber. Cells were washed 3 × 5 min with PBS/0.1% saponin, and incubated with Alexa 594-conjugated secondary antibody (Jackson ImmunoResearch 711-585-152) diluted in blocking buffer. Cells were

washed 3 × 5 min with PBS and imaged in PBS on a Nikon Eclipse Ti microscope coupled to an Andor Revolution XD spinning disk confocal system, composed of an iXon Ultra 897 CCD camera (Andor Technology), a solid-state laser combiner (ALC-UVP 350i, Andor Technology), and a CSU-X1 confocal scanner (Yokogawa Electric Corporation), controlled by Andor IQ3 software (Andor Technology). A z-stack (0.1 µm step size) through the entire cell was acquired with a 100x NA 1.45 Plan-Apochromat objective (Nikon). After fluorescence imaging, cells were further processed for TEM as described above (see *Transmission Electron Microscopy* section), except that sequential sections were cut at 70 nm and formvar-coated slot grids (Electron Microscopy Sciences) were used. Fluorescence images corresponding to EM images were identified based on the shape of the cell's outer boundary. Images (Figure S3D) were linearly resized, rotated, and moved in x and y to achieve best visual overlay using Fiji software.

Structure prediction

The ColabFold implementation (Mirdita *et al.*, 2022) of AlphaFold2 (AF2) (Jumper *et al.*, 2021) was used for structure prediction. The CDR2–DLIC1–DHC–DIC2 complex (Figure S1A) was predicted by running ColabFold v1.5.5 with default parameters on two copies of CDR2(1–139) (UniProt Q01850), two copies of DC1L1(440–455) (UniProt Q9Y6G9), one copy of DYHC1(576–864) (UniProt Q14204) and one copy of DC1I2(226–583) (UniProt Q13409). The CDR2–KTN1 complex (Figure 8D) was predicted using two copies each of CDR2(421–454) (UniProt Q01850) and KTN1(1114–1357) (UniProt Q86UP2). The eEF1Bβ–KTN1 complex (Figure S3F) was predicted using one copy of EF1D(1–281) (UniProt P29692) and two copies of KTN1(1114–1357) (UniProt Q86UP2). The structure showing that eEF1Bβ and CDR2 occupy the same binding site on KTN1 (Figure 11A) was predicted using one copy of CDR2(421–454) (UniProt Q01850), one copy of EF1D 39–68 (UniProt P29692) and two copies of KTN1(1114–1357) (UniProt Q86UP2). Structures were visualized with UCSF ChimeraX (Pettersen *et al.*, 2021).

Cell cycle synchronization

For synchronization at the G1/S boundary, HeLa control cells growing in standard medium at 40–50% confluency were treated with 2 mM thymidine (Sigma-Aldrich) for 16 h. Thymidine was then washed out twice with PBS and three times with standard medium (5 min each, in the incubator). Cells were subsequently incubated for 8 h in standard medium before a second 16 h thymidine treatment. At this point, cells were arrested at the G1/S boundary. To release the block, cells were washed again with PBS and standard medium as described and lysed at the indicated time points. For mitotic (G2/M) synchronization, cells were treated with 3 µM nocodazole (Sigma-Aldrich) for 8 h following

release from the second thymidine block. Cells were lysed as described before in *Immunoblotting* section.

Graphs and statistical analysis

Prism 10.0 software (GraphPad) was used for statistical analysis and to generate graphs. Statistical significance was determined using a two-tailed t test or ordinary one-way ANOVA followed by Tukey's multiple comparisons test. The analytical method used is specified in the figure legends.

***In vitro* TIRF motility assays**

Protein expression and purification of dynein, dynactin and LIS1 proteins used in *in vitro* TIRF motility assays, and the assays themselves were performed by Kashish Singh in the laboratory of Andrew P. Carter at the MRC Laboratory of Molecular Biology (Cambridge, United Kingdom). Materials and methods can be seen in (Teixeira *et al.*, 2025).

CHAPTER IV.

RESULTS

RESULTS

This chapter includes both unpublished and published results reported in Vanessa Teixeira, Kashish Singh, José Gama, Matilde Moreira, Ricardo Celestino, Ana Xavier Carvalho, Paulo Pereira, Carla Abreu, Tiago Dantas, Andrew Carter, and Reto Gassmann. (2025). CDR2 is a dynein adaptor recruited by kinectin to regulate ER sheets organization. *Journal of Cell Biology*. https://doi.org/10.1083/jcb.202411034.

CDR2 and CDR2L are novel adaptors for cytoplasmic dynein-1

The first coiled-coil of human CDR2 and its paralog CDR2L contain a N-terminal CC1 box followed by an HBS1 (Figure 7A; Figure S1A, B), suggesting they might be dynein adaptors. To test this, the ability of the CC1 box to bind DLIC was assessed using purified recombinant proteins. SEC demonstrated that CDR2(1–146) forms a complex with GST::DLIC1(388–523), but not when the CC1 box is deleted (Δ23–39) (Figure 7B) or when DLIC1 residues known to be critical for CC1 box binding are mutated (F447A/F448A) (Celestino *et al.*, 2019) (Figure S1C). GST pull-down experiments likewise showed that CDR2L binds GST::DLIC1(388–523) in a CC1 box-dependent manner (Figure 7C).

Next, the ability of purified recombinant CDR2 and CDR2L to form complexes with dynein and dynactin from porcine brain lysate was evaluated. When affinity-isolated from lysate through their C-terminal Strep-tag II, CDR2(1–146), CDR2L(1–159) and CDR2L(1–290) co-isolated dynein–dynactin (Figure 7D). CDR2(1–146) performed as robustly in this assay as the previously characterized activating adaptor fragment JIP3(1–185) (Singh *et al.*, 2024), while CDR2L fragments were less efficient. The CC1 box in CDR2(1–146) and CDR2L(1–290) was essential for complex formation, and introducing point mutations into the HBS1 motif (HBS1_6A) of CDR2(1–146) reduced complex formation (Figure 7D).

Finally, in collaboration with Kashish Singh and Andrew P. Carter (MRC Laboratory of Molecular Biology, Cambridge, United Kingdom), it was assessed whether CDR2 and CDR2L support processive movement of tetramethylrhodamine (TMR)-labeled dynein–dynactin in a motility assay, using LIS1 to facilitate dynein activation (Baumbach *et al.*, 2017) (Figure 7E). This revealed that CDR2L fragments 1–159 and 1–290 can activate dynein motility in a CC1 box-dependent manner, although they were less potent than JIP3(1–185). Dynein activation could not be detected with CDR2(1–146), for reasons that remain unclear. Longer CDR2 fragments also failed to activate, although it is noted that dynein adaptors typically adopt autoinhibited conformations (Abid Ali *et al.*, 2025; d'Amico *et al.*, 2022; Hoogenraad *et al.*, 2003; Singh *et al.*, 2024).

These findings indicate that CDR2 and CDR2L exhibit biochemical properties characteristic of dynein adaptors.

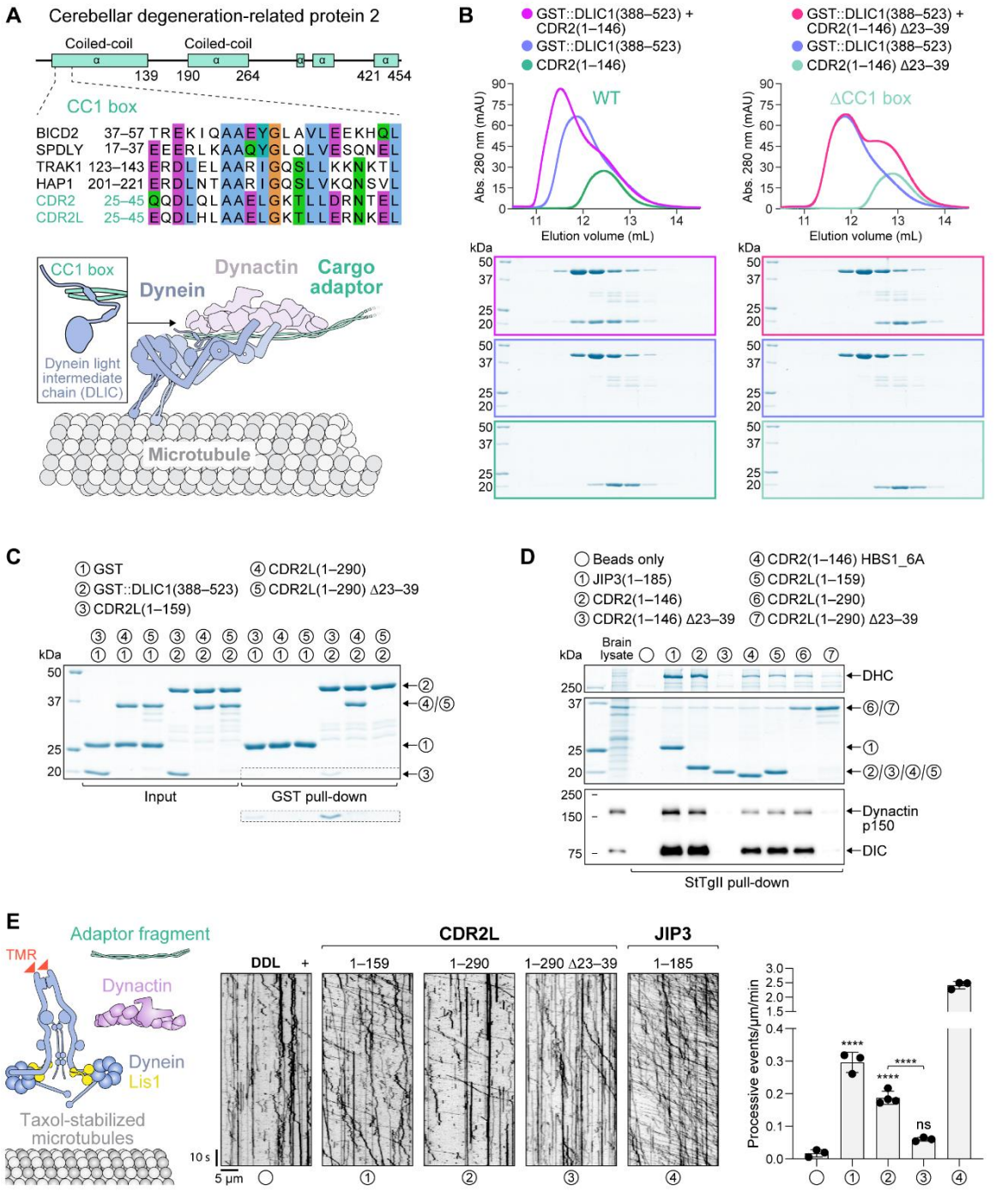

Figure 7 – CDR2 and CDR2L are novel adaptors for cytoplasmic dynein-1.

(A) Schematic of the human CDR2 protein and sequence alignment of its N-terminal CC1 box (motif AAXXG) with that of other human dynein adaptors *(see also Figure S1B)*. The CC1 box binds DLIC, as illustrated in the cartoon below the alignment. *(continued on the next page)*

Figure 7 *(continued)* – CDR2 and CDR2L are novel adaptors for cytoplasmic dynein-1.
(B) Elution profiles and BlueSafe-stained SDS-PAGE gels of purified recombinant human CDR2 and DLIC1 fragments after SEC. The elution profile and gel for DLIC1 are shown on both left and right to facilitate comparison between wild-type (WT) CDR2 and the ΔCC1 box mutant. Molecular weight is indicated in kDa. **(C)** BlueSafe-stained SDS-PAGE gels of purified recombinant proteins prior to addition of glutathione agarose resin (Input) and after elution from the resin (GST pull-down), showing that CDR2L binds to DLIC1. For CDR2L(1–159), a contrast-enhanced version of the pull-down is shown in separate. **(D)** BlueSafe-stained SDS-PAGE gel and immunoblot after pull-down of purified recombinant proteins, C-terminally tagged with StTgII, from porcine brain lysate. In the HBS1_6A construct, 6 residues in CDR2's predicted HBS1 are mutated to alanine, as shown in *Figure S1B*. **(E)** *In vitro* motility assays with TMR-labeled dynein, dynactin, LIS1 and adaptor fragments. Representative kymographs and the number of processive events per micrometer of microtubule per minute (mean ± SD of 3-4 technical replicates) are shown. The total number of events analyzed were 21 (DDL), 344 (CDR2L1-159), 278 (CDR2L1-290), 69 (CDR2L1-290 ΔCC1) and 304 (JIP31-185). Statistical significance was determined using ordinary one-way ANOVA followed by Tukey's multiple comparisons test. ****$P < 0.0001$; *ns* = not significant, $P > 0.05$.

CDR2 and CDR2L interact and co-localize with the integral ER membrane protein KTN1

To identify potential cargo linked to dynein via the adaptors CDR2 and CDR2L, immunoprecipitations were performed from HeLa cells stably expressing transgenic GFP::3xFLAG-tagged CDR2 or CDR2L in a CDR2/L double KO background (Figure S2A, B). Quantitative mass spectrometry revealed that the ER sheet component KTN1 was the most enriched protein in anti-FLAG immunoprecipitates from both transgenic cell lines when compared to control immunoprecipitates from control CDR2/L double KO cells (Figure 8A). Immunoprecipitates from GFP::3xFLAG::CDR2L cells were additionally enriched for the KTN1 paralog p180 (Figure 8A).

Immunofluorescence revealed striking co-localization of GFP::3xFLAG::CDR2 with KTN1 (Figure 8B). GFP::3xFLAG::CDR2L also co-localized with KTN1 and in addition exhibited diffuse cytoplasmic localization (Figure S2C). To test whether the endogenous proteins localize to ER sheets, HeLa cells were co-stained with antibodies against CDR2 and CDR2L and the ER sheet component CLIMP63 (Shibata *et al.*, 2010). Endogenous CDR2 was reproducibly detectable on ER sheets by immunofluorescence (Figure 8C). Signal intensity varied between cells and was generally close to background signal observed in CDR2 KO cells, which were used as a control for antibody specificity. This suggests CDR2 is expressed at relatively low levels in HeLa cells. Although CDR2L was detectable by immunoblot (Figure S2A), specific immunofluorescence signal could not be

detected with multiple antibodies, including one generated during this study, against CDR2L.

Overall, these data suggest that the dynein adaptors CDR2 and CDR2L interact with ER sheet components and localize to ER sheets.

A C-terminal helix in CDR2 is necessary and sufficient for binding to KTN1 and recruitment to ER sheets

To determine whether CDR2 and KTN1 directly bind each other, AF2 (Jumper *et al.*, 2021) was first used to predict interacting domains. KTN1 consists of an N-terminal transmembrane domain anchored in the ER membrane followed by a 1000-residue cytoplasmic domain with multiple segments of parallel dimeric coiled-coil. Structure prediction identified a high-confidence interaction between the last coiled-coil segment of KTN1 and the C-terminal helix in CDR2, which is highly conserved in CDR2 and CDR2L homologs from vertebrate and invertebrate species (Figure 8D; Figure S2D). SEC with purified recombinant KTN1(991–1357) and GST::CDR2(411–454) confirmed this interaction, which was abolished when the predicted CDR2 binding site in KTN1 was deleted (∆1114–1153) (Figure 8E). Transient expression of GFP-tagged CDR2 and CDR2L fragments in CDR2/L double KO cells showed that the C-terminal helix is necessary and sufficient for co-localization with KTN1 (Figure 8F; Figure S2E).

Interestingly, knockdown of KTN1 by RNAi not only delocalized CDR2 but also decreased its total levels (Figure S2F–H), suggesting that the KTN1–CDR2 interaction stabilizes CDR2. It was concluded that KTN1 recruits CDR2 through a direct interaction between their C-termini (Figure 8G).

Given that the binding site for the C-terminal helix of CDR2 and CDR2L is conserved in the KTN1 paralog RRBP1/p180 (Figure S2I), dynein is likely recruited to the ER by both of these integral membrane proteins. Since p180 was selectively enriched in immunoprecipitates of GFP::3xFLAG::CDR2L (Figure 8A), CDR2 and CDR2L may preferentially bind to KTN1 and p180, respectively.

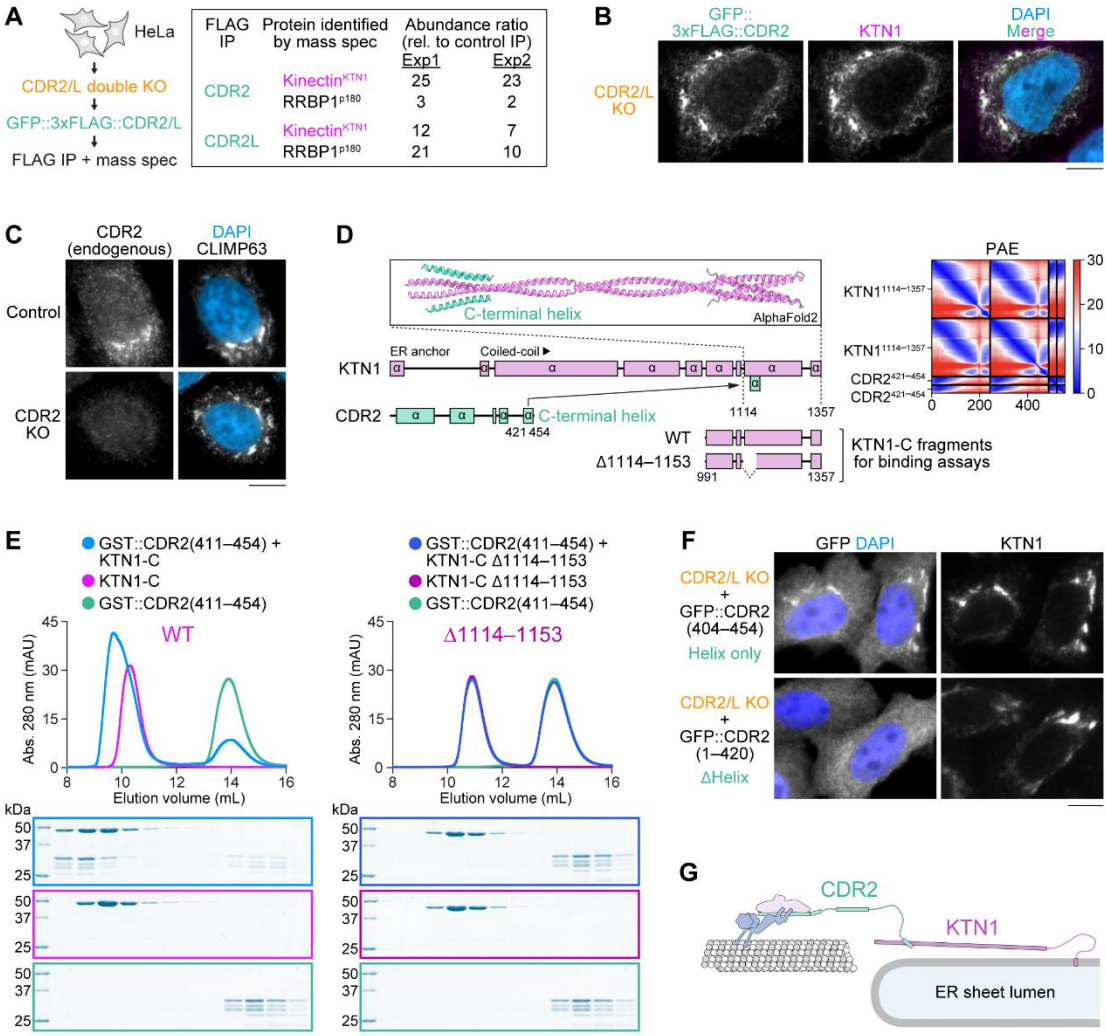

Figure 8 – CDR2 and CDR2L interact and co-localize with the integral ER membrane protein KTN1.

(A) Schematic illustrating construction of HeLa CDR2/L double KO cell lines stably expressing exogenous GFP::3xFLAG-tagged CDR2 or CDR2L used for immunoprecipitation followed by quantitative mass spectrometry. The relative abundance of KTN1 and RRBP1/p180 in anti-FLAG immunoprecipitations from transgenic and control CDR2/L double KO cells is shown for two independent experiments (Exp1 and 2) on the right. **(B)** Immunofluorescence image of a HeLa cell stably expressing GFP::3xFLAG-tagged CDR2, showing co-localization with the ER sheet protein KTN1. Scale bar, 5 µm. **(C)** Immunofluorescence showing co-localization of endogenous CDR2 with the ER sheet protein CLIMP63. A CDR2 KO cell serves as the control for CDR2 antibody specificity. Scale bar, 5 µm. **(D)** AF2 model and predicted alignment error (PAE) plot of the KTN1 C-terminal coiled-coil domain in complex with the C-terminal helix of CDR2. KTN1 domain organization and C-terminal KTN1 fragments (KTN1-C) used for *in vitro* binding assays in *(E)* are also shown. *(continued on the next page)*

Figure 8 *(continued)* – CDR2 and CDR2L interact and co-localize with the integral ER membrane protein KTN1.

(E) Elution profiles and BlueSafe-stained SDS-PAGE gels of purified recombinant human CDR2 and KTN1 fragments after SEC. The elution profile and gel for CDR2 are shown on both left and right to facilitate comparison between wild-type KTN1-C and the Δ1114–1153 mutant. Molecular weight is indicated in kDa. **(F)** Immunofluorescence images of HeLa CDR2/L double KO cells transiently expressing the GFP-tagged C-terminal helix of CDR2 or GFP::CDR2 without the helix, demonstrating that the helix is necessary and sufficient for ER localization. Scale bar, 5 µm. **(G)** Cartoon of the dynein recruitment pathway at ER sheets, based on results from *in vitro* reconstitution of protein–protein interactions and cell-based assays with binding-deficient mutants.

Double KO of CDR2 and CDR2L promotes organization of ER sheets into stacks

To address the function of CDR2 and CDR2L, ER morphology was examined in CDR2/L double KO cells. Immunofluorescence showed that the naturally patchy distribution of the ER sheet components KTN1 and CLIMP63 became significantly more patchy in CDR2/L double KO cells (Figure 9A; Figure S3A). By contrast, there was no obvious effect on the morphology or positioning of the Golgi apparatus, marked by GM130 (Figure S3B), or on the distribution of ER exit sites, marked by SEC16A (Figure S3C). Correlative light–electron microscopy revealed that the bright µm-sized KTN1 patches observed by immunofluorescence correspond to stacks of ER sheets (Figure S3D). In the absence of CDR2 and CDR2L, the fraction of cells with bright KTN1 patches was increased (Figure 9A), and ER sheet stacks contained more sheets per stack, as determined by transmission electron microscopy (TEM) (Figure 9B).

Depleting KTN1 by RNAi in CDR2/L double KO cells essentially abolished ER sheet stacking but not formation of ER sheets *per se* (Figure 9C, D; Figure S3E), consistent with prior work implicating ER sheet proteins in stacking (Shibata *et al.*, 2010). Immunoblotting showed that KTN1 levels were unchanged in CDR2/L double KO cells (Figure S2H), suggesting enhanced stacking is not due to KTN1 overexpression. Instead, the brightness of KTN1 patches may indicate that KTN1 distribution within the ER becomes more concentrated on sheets in the absence of CDR2 and CDR2L. The CDR2/L double KO phenotype could be reversed by expressing exogenous wild-type GFP::CDR2 but not CDR2 lacking its CC1 box (Δ23–39) or C-terminal helix (Δ421–454) (Figure 9E–G; Figure S3F).

Collectively, these results suggest that CDR2 opposes the KTN1-dependent organization of ER sheets into stacks, and that this requires CDR2 recruitment by KTN1 and CDR2's DLIC-binding CC1 box (Figure 9H).

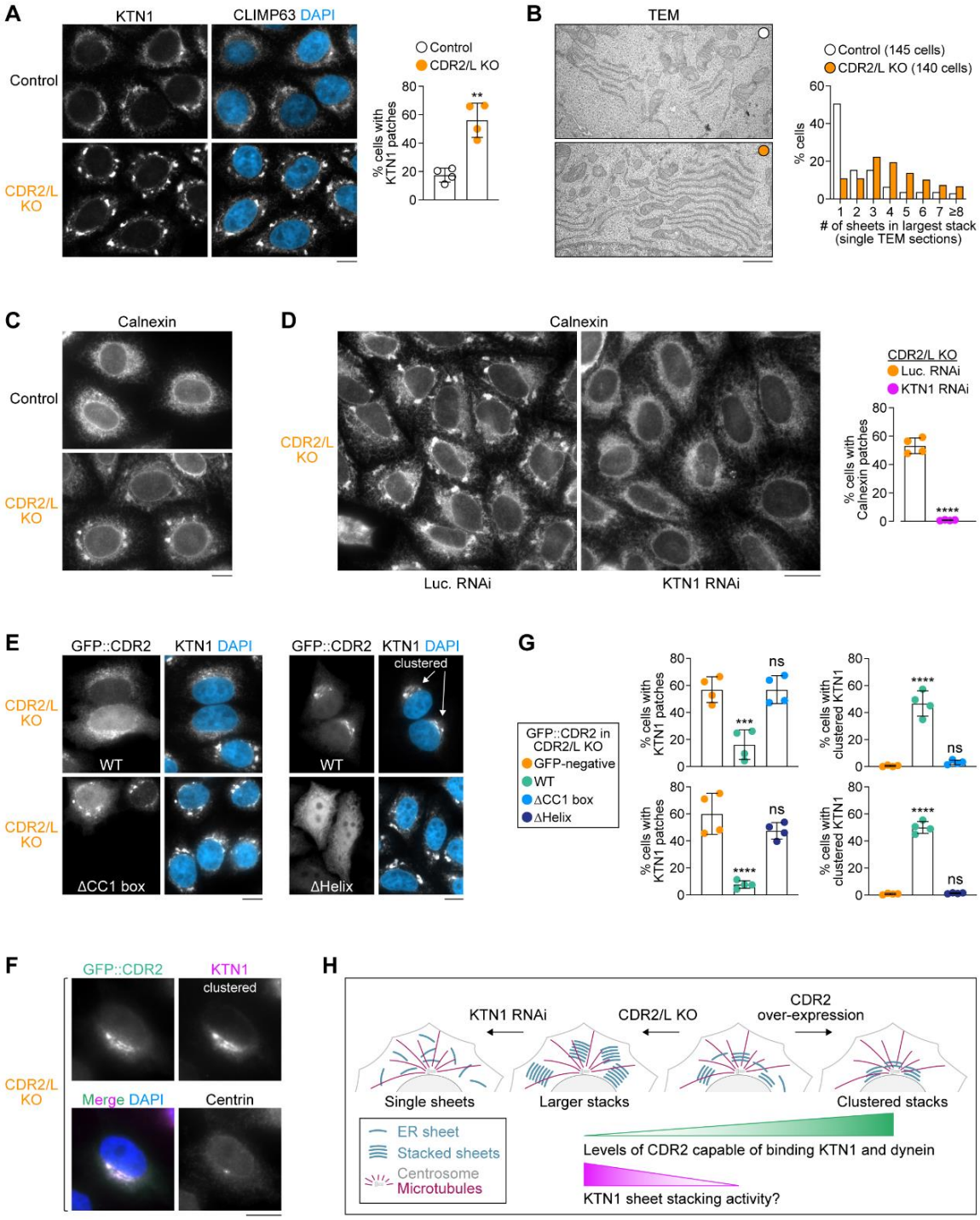

Figure 9 – CDR2 regulates the organization of ER sheets.

(A) *(left)* Immunofluorescence images showing exacerbated patchy distribution of KTN1 and CLIMP63 in HeLa CDR2/L double KO cells. Scale bar, 5 µm. *(right)* Fraction of cells with prominent KTN1 patches, plotted as mean ± SD (4 independent experiments, >1000 cells scored in total per condition). Statistical significance was determined using a two-tailed t test. ***P* < 0.01. See also *Figure S3A*. **(B)** *(left)* TEM images of ER sheets in control and CDR2/L double KO cells, both treated with siRNAs against Luciferase to facilitate comparison with KTN1 depletion in *Figure S3E*. Scale bar, 1 µm. *(right)* Number of ER sheets present in the largest stack identified in individual cells using single TEM sections. The total number of cells analyzed in 3 independent experiments is indicated. *(continued on the next page)*

Figure 9 *(continued)* – CDR2 regulates the organization of ER sheets.
(C), (D) Immunofluorescence showing patchy distribution of the ER protein Calnexin in CDR2/L double KO cells, which is abolished after knockdown of KTN1 by RNAi. Luciferase (Luc.) RNAi serves as the control. Scale bars, 10 µm *(C)* and 20 µm *(D)*. The fraction of cells with prominent Calnexin patches is plotted as mean ± SD (4 independent experiments, >1500 cells scored in total per condition). Statistical significance was determined using a two-tailed t test. ****$P < 0.0001$. **(E), (F)** Immunofluorescence images of CDR2/L double KO cells transiently expressing WT GFP::CDR2 or mutants lacking residues 23–39 (ΔCC1 box) or 404–454 (ΔHelix). Centrin-3 staining in *(F)* shows that WT GFP::CDR2 and KTN1 cluster together at centrosomes. Images in *(E)* include examples of untransfected cells (GFP-negative) for comparison. Scale bars, 10 µm. **(G)** Fraction of cells (mean ± SD, 4 independent experiments, >600 cells scored in total per condition) with prominent KTN1 patches *(left)* and centrosome-proximal KTN1 clustering *(right)* in the conditions shown in *(E)*. ΔCC1 box and ΔHelix experiments each have their own WT and GFP-negative controls. Statistical significance was determined using ordinary one-way ANOVA followed by Tukey's multiple comparisons test. ****$P < 0.0001$; ***$P < 0.001$; *ns* = not significant, $P > 0.05$. **(H)** Cartoon summarizing the effect of CDR2 and KTN1 levels on ER sheet organization.

CDR2 overexpression results in CC1 box-dependent clustering of ER sheets near centrosomes

Rescue experiments with exogenous GFP::CDR2 in CDR2/L double KO cells revealed that in addition to reversing excessive ER sheet stacking, GFP::CDR2 frequently induced clustering of ER sheets near centrosomes, marked by centrin-3 staining (Figure 9E–G; Figure S3G). The KTN1 signal near centrosomes remained distinct from that of GM130, suggesting that ER clustering does not induce trafficking of ER sheet components to the Golgi apparatus (Figure S3H). ER sheet clustering in CDR2/L double KO cells was never observed with exogenous GFP::CDR2 lacking the CC1 box or C-terminal helix. ER sheets also did not cluster appreciably in untransfected control cells, suggesting that clustering is specifically induced by exogenous GFP::CDR2. These results support the idea that KTN1-associated CDR2 can recruit dynein activity to promote centrosome-directed transport of ER sheets (Figure 9H).

To compare CDR2's ability to recruit dynein activity to that of another established activating adaptor, the CDR2 N-terminal region (1–185) was replaced with that of JIP3 (Singh *et al.*, 2024). The JIP3(1–185)::CDR2(186–454) chimera co-localized with KTN1 in CDR2/L double KO cells and induced penetrant and tight clustering (Figure S3I). This indicates that the CDR2 N-terminus is less efficient than that of JIP3 at dynein recruitment and/or activation at ER sheets, which would be consistent with our results from *in vitro*

motility assays. Alternatively, the efficiency of the JIP3::CDR2 chimera may reflect the absence of autoinhibition mechanisms present in full-length CDR2.

Overexpression of KTN1 lacking CDR2 binding site mimics the CDR2/L double KO phenotype in U2OS cells

After identifying the CDR2 binding site in the C-terminus of KTN1, KTN1 mutants were engineered for overexpression in U2OS cells to assess their effect on ER morphology and determine whether deleting CDR2 binding site in KTN1 results in a phenotype similar to that of the CDR2/L double KO. Overexpression of KTN1(1-1357)::3xFLAG dramatically altered ER morphology, resulting in dense and extensive ER sheet-like structures that occupied much of the cytoplasm, with few remaining tubules at the cell periphery (Figure 10). In contrast, overexpression of KTN1(Δ1114-1153)::3xFLAG, which misses CDR2 binding site, resulted in a patchy distribution of the ER, a phenotype resembling that observed in CDR2/L double KO cells (Figure 10). Although this phenotype was not quantified, the similarity in ER morphology suggests a critical role for the CDR2–KTN1 interaction in maintaining proper ER sheet organization.

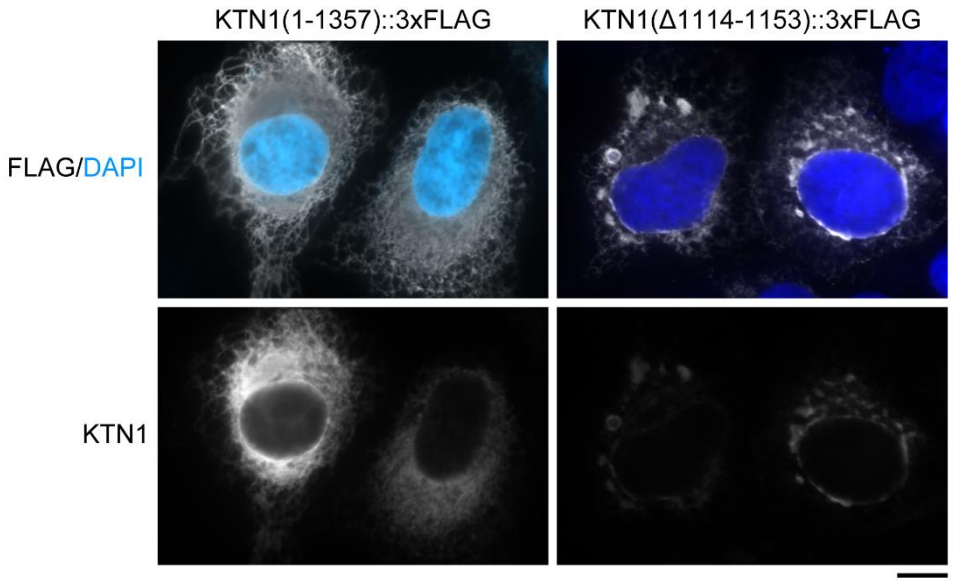

Figure 10 – KTN1 lacking CDR2 binding site mimics CDR2/L double KO phenotype in U2OS cells.

Immunofluorescence images (maximum intensity projection of z-stack) showing U2OS cells transiently transfected with KTN1(1-1357)::3xFLAG showing extensive ER sheet structures and KTN1(Δ1114-1153)::3xFLAG (CDR2 binding site deletion) showing a patchy ER morphology. Cells were stained with FLAG and KTN1 antibodies. Scale bar, 10 µm.

CDR2 competes with eEF1Bβ, but not KIF5C, for binding to KTN1

Prior studies identified the three KIF5 isoforms and the eEF1Bβ subunit of the translation elongation factor 1B complex (eEF1B) as direct binding partners of the human KTN1 C-terminus (Ong *et al.*, 2000, 2003, 2006). The KIF5 binding site was mapped to KTN1 residues 1188-1288 (Ong *et al.*, 2000). CDR2 and KIF5 therefore occupy adjacent, non-overlapping sites. By contrast, structure prediction suggested that a helix formed by eEF1Bβ residues 33–60 occupies the same site on KTN1 as the CDR2 helix (Figure 11A; Figure S4A). SEC with purified recombinant proteins demonstrated that GST::eEF1Bβ(30–66) forms a robust complex with KTN1(991–1357), but not when the CDR2 binding site in KTN1 is deleted (Δ1114–1157) (Figure 11B). GST pull-downs confirmed that KTN1(991–1357) binds GST::KIF5C(807–956) and showed that this interaction is insensitive to deletion of the CDR2/eEF1Bβ binding site (Figure S4B). Adding an excess of eEF1Bβ(30–127), which contains the KTN1-binding helix and a helix that forms a trimeric coiled-coil (Figure S4A, C), substantially reduced the amount of KTN1(991–1357) recovered in GST::CDR2(421–454) pull-downs (Figure 11C). In cells, eEF1Bβ co-localized with KTN1 and CDR2 (Figure 11D, E), and replacing the CDR2 helix with the eEF1Bβ helix was sufficient to localize the GFP-tagged chimera to ER sheets (Figure 11F). Furthermore, overexpression of GFP::CDR2 lacking its CC1 box (Δ23–39) displaced eEF1Bβ from KTN1 patches in CDR2/L double KO cells (Figure 11G).

It was concluded that eEF1Bβ, but not KIF5C, competes with CDR2 for binding to KTN1 and recruitment to ER sheets.

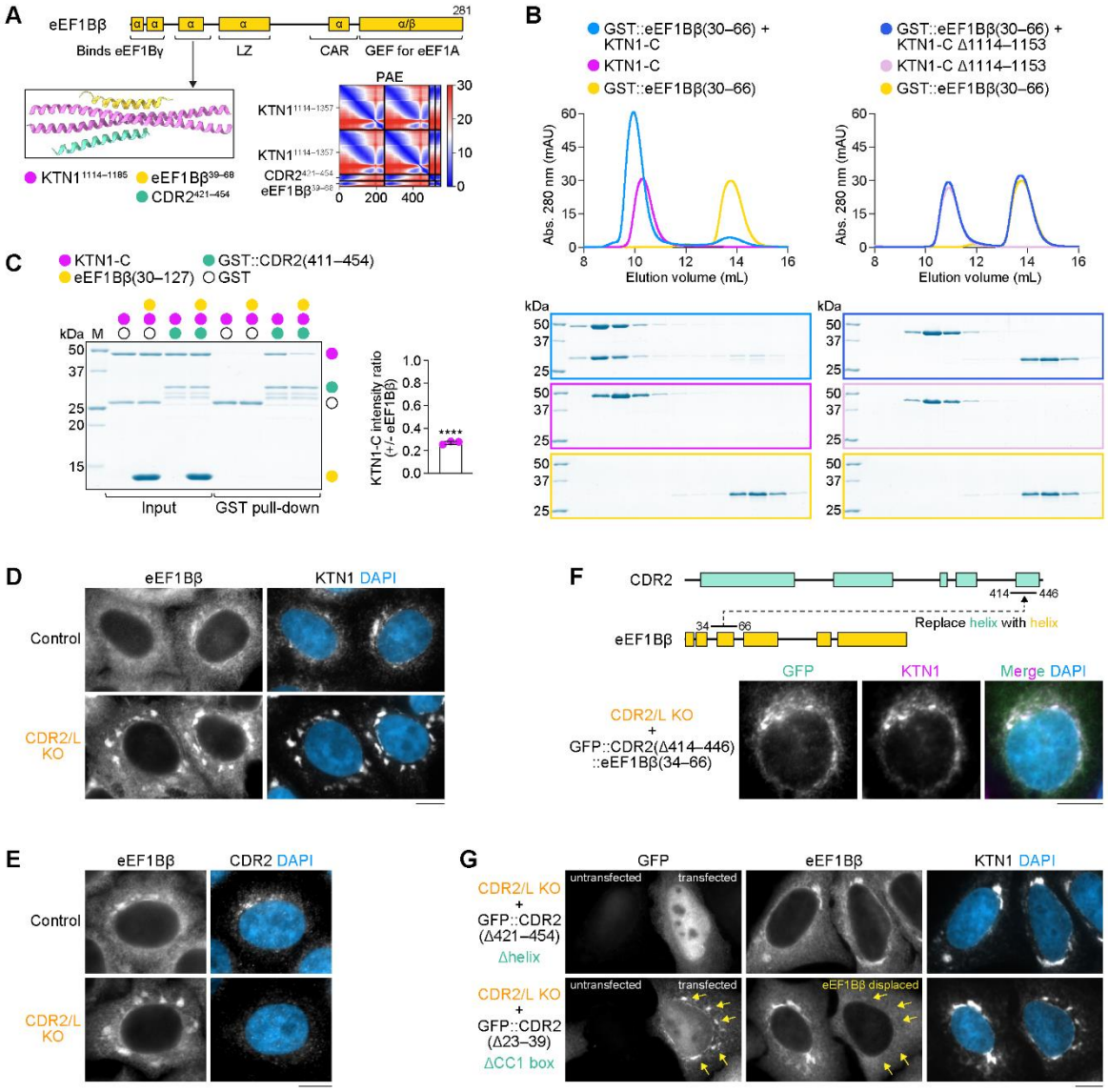

Figure 11 – CDR2 competes with eEF1Bβ for binding to KTN1 and localization to ER sheets.

(A) Domain organization of the β subunit of eEF1Bβ (UniProt P29692; encoded by gene EEF1D). AF2 model and PAE plot shows that an N-terminal eEF1Bβ helix and the C-terminal CDR2 helix occupy the same site in KTN1. See *Figure S4A* for a prediction of full-length eEF1Bβ in complex with KTN1. **(B)** Elution profiles and BlueSafe-stained SDS-PAGE gels of purified recombinant human eEF1Bβ and KTN1 fragments after SEC. The elution profile and gel for eEF1Bβ are shown on both left and right to facilitate comparison between WT KTN1-C and the Δ1114–1153 mutant. Molecular weight is indicated in kDa. **(C)** *(left)* BlueSafe-stained SDS-PAGE gels of purified recombinant proteins prior to addition of glutathione agarose resin (Input) and after elution from the resin (GST pull-down), showing that adding an excess of eEF1Bβ(30–127) reduces the amount of KTN1-C associated with GST::CDR2(421–454). *(continued on the next page)*

Figure 11 *(continued)* – CDR2 competes with eEF1Bβ for binding to KTN1 and localization to ER sheets. (C) *(right)* Quantification of KTN1-C levels (mean ± SD, 3 independent experiments) in pull-downs after adding a 20-fold molar excess of eEF1Bβ(30–127), normalized to KTN1-C levels in pull-downs without eEF1Bβ(30–127). Statistical significance was determined using a two-tailed t test. ****$P < 0.0001$. **(D), (E)** Immunofluorescence demonstrating co-localization of eEF1Bβ, KTN1, and CDR2 in HeLa cells. Scale bars, 10 µm. **(F)** Domain swapping experiment showing that replacing the C-terminal CDR2 helix with the N-terminal eEF1Bβ helix (both 33 residues long) is sufficient to target GFP::CDR2 to the ER. Scale bar, 10 µm. **(G)** Immunofluorescence showing that overexpression of GFP::CDR2 displaces eEF1Bβ from the ER (arrows), but only if CDR2 can bind KTN1. Scale bar, 10 µm.

eEF1Bβ knockdown enhances recruitment of endogenous CDR2 to ER sheets and promotes ER sheet clustering near centrosomes

Given that eEF1Bβ is an abundant protein, eEF1Bβ levels may be limiting for CDR2 recruitment to ER sheets due to competition for KTN1 binding. To test this idea, eEF1Bβ levels were decreased by RNAi. Immunoblotting showed that overall levels of CDR2 increased (~1.4 fold) and KTN1 levels remained unchanged after eEF1Bβ knockdown (Figure 12A). CDR2 localization to ER sheets was significantly more pronounced in eEF1Bβ-depleted cells, consistent with the idea that KTN1 is now free to bind CDR2 (Figure 12B). Strikingly, ER sheets with elevated CDR2 levels tended to cluster near centrosomes (Figure 12C, D). By contrast, ER sheet distribution remained unchanged when eEF1Bβ was knocked down in CDR2/L double KO cells (Figure S4D). These results support the idea that enhanced recruitment of CDR2 to ER sheets promotes ER sheet clustering near centrosomes.

Taken together, these findings suggest that competitive binding of the dynein adaptor CDR2 and eEF1Bβ to KTN1 regulates ER sheet organization.

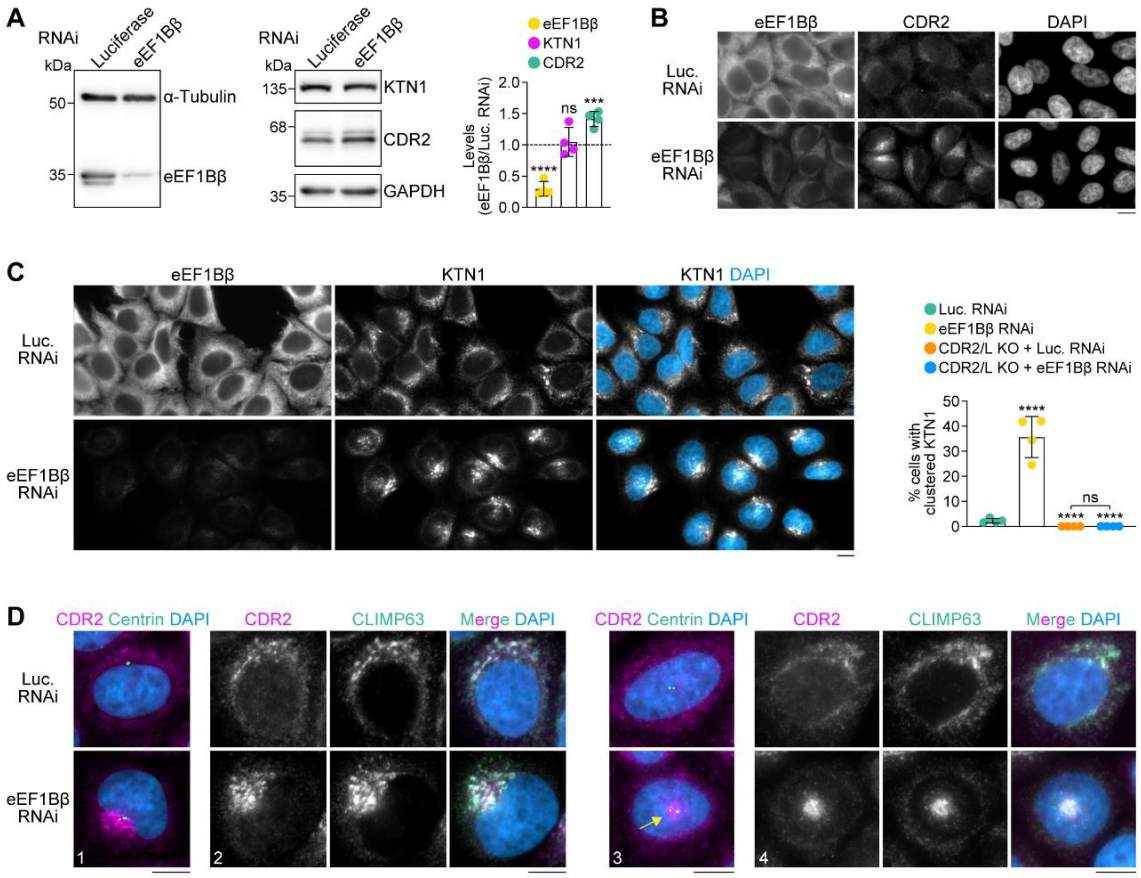

Figure 12 – eEF1Bβ knockdown enhances CDR2 recruitment to ER sheets and promotes ER sheet clustering near centrosomes.

(A) Immunoblots and quantification of protein levels in HeLa control cells treated with siRNAs against Luciferase or eEF1Bβ. The 3 immunoblots on the right are from the same membrane. Protein levels relative to Luciferase RNAi, quantified based on immunoblot signal intensity after normalization to the loading control (α-tubulin for eEF1Bβ, GAPDH for CDR2 and KTN1), are plotted as mean ± SD (4 independent experiments). Statistical significance was determined using a two-tailed t test. ****P < 0.0001; ***P < 0.001; *ns* = not significant, P > 0.05. **(B)** Immunofluorescence images showing enhanced ER localization of CDR2 in eEF1Bβ-depleted HeLa control cells. Scale bar, 10 µm. **(C)** Immunofluorescence images (maximum intensity projection of z-stack) showing that eEF1Bβ knockdown results in redistribution of KTN1 into clusters. Scale bar, 20 µm. See *Figure S4D* for corresponding immunofluorescence images in CDR2/L double KO cells. The fraction of mock- and eEF1Bβ-depleted cells with a clustered KTN1 distribution is plotted as mean ± SD (4 independent experiments, >1300 cells scored in total per condition). Statistical significance was determined using ordinary one-way ANOVA followed by Tukey's multiple comparisons test. ****P < 0.0001; *ns* = not significant, P > 0.05. **(D)** Immunofluorescence images (maximum intensity projection of z-stack) illustrating that CDR2 and CLIMP63 clustering together at centrosomes in eEF1Bβ-depleted cells. Four examples are shown, in which the ER clusters either on the side (cells 1 and 2) and on top (cells 3 and 4) of the nucleus. Scale bars, 10 µm

CDR2/L KO cells show normal proliferation rates

To further investigate the effects of CDR2/L loss, the proliferative capacity of CDR2/L double KO cells was monitored over six consecutive days. Two independent CDR2/L double KO clones exhibited a slight decrease in their proliferative rate compared to the control cell line, particularly from day four onward (Figure 13A). Calculation of doubling times confirmed that the control cell line required less time to double (1.61 days) than CDR2/L double KO clones (1.76 and 1.71 days), although this difference was not statistically significant (Figure 13B).

Additionally, cell sorting with propidium iodide staining was performed to analyze cell cycle distribution. All cell lines displayed a normal cell cycle profile. However, a modest but consistent reduction in the percentage of cells in G1 phase was observed in CDR2/L double KO clones compared to the control (Figure 13C). Despite this, no significant changes were found in the overall distribution across S and G2/M phases (Figure 13C, D).

The duration of mitosis, measured as the time from NEBD to the onset of anaphase, assessed by time-lapse imaging, was not significantly altered in CDR2/L double KO cells. However, one CDR2/L double KO clone displayed a significantly shorter mitotic duration compared to control cells (Figure 13E), which may reflect clonal variation or off-target effects. Although both CDR2/L double KO clones showed a trend toward a reduced mitotic index and increased overall cell death, these differences were not statistically significant (Figure 13F, G).

Overall, these data suggest that the CDR2/L loss does not cause major disruptions in cell proliferation, cell cycle progression, or cell viability under the tested conditions. The slight reduction in proliferation rate and decreased G1-phase occupancy observed in the CDR2/L double KO cells may indicate a subtle alteration in cell cycle regulation. Although these changes were not statistically significant, they are consistent with previous findings that CDR2L KO impairs proliferation in OVCAR-3 ovarian carcinoma cells (Solheim *et al.*, 2024). These findings suggest that while CDR2/L are dispensable for basal cell cycle progression and viability, they may influence proliferation in a context-dependent manner, particularly under stress or in specific cancer background.

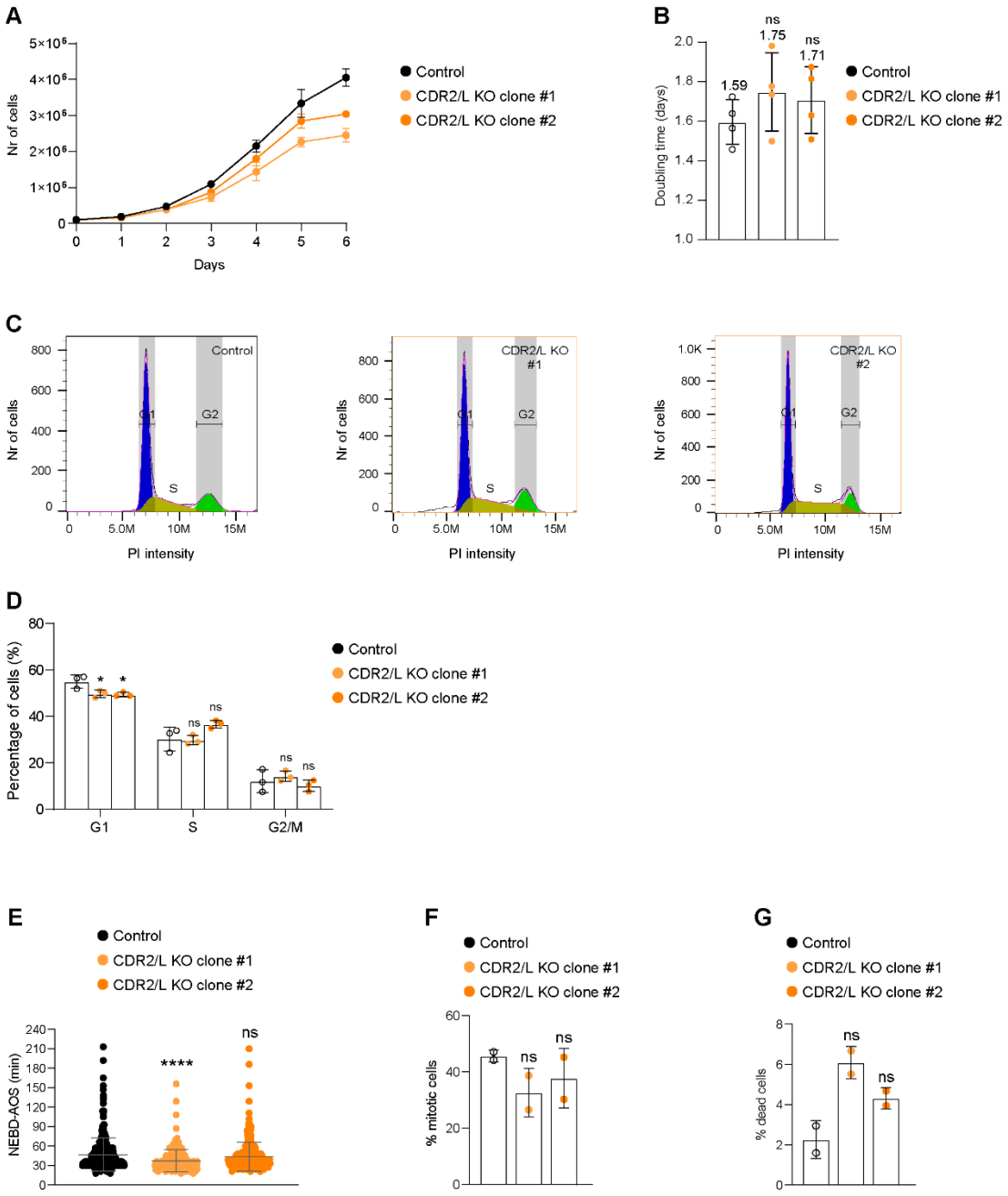

Figure 13 – CDR2/L double KO cells show normal proliferation rates.

(A) Cell growth curves and **(B)** doubling times of control and two independent CDR2/L double KO clones. Cells were seeded at 1x10⁵ cells/well and counted for six consecutive days. Growth curves represent the mean ± SD of four independent experiments. Growth curves data were fitted to a non-linear growth model and doubling times were calculated using GraphPad Prism 10. Statistical analysis was determined by a two-tailed t test. *ns* = not significant**. (C)** Cell cycle profile of control and two independent CDR2/L double KO clones determined by FACS analysis. The graphs illustrate the cell count (three independent experiments) in the different phases of the cell cycle, which correlates to the PI intensity. Cells cycle distribution was quantified by applying the Dean-Jett-Fox model. **(D)** Quantification of cell cycle distribution. Data represents the mean ± SD (three independent experiments). Statistical significance was determined using a two-tailed t test. **P* < 0.05, *ns* = not significant. *(continued on the next page)*

Figure 13 *(continued)* – CDR2/L double KO cells show normal proliferation rates.
(E) Duration of NEBD to anaphase onset (AOS) in control and two CDR2/L double KO clones, measured by live-cell imaging. Each dot represents a single mitosis. Mean ± SD (two independent experiments) is shown. Statistical significance was determined by a two-tailed t test. ****$P < 0.0001$, *ns* = not significant. **(F)** Percentage of mitotic cells in control and CDR2/L double KO clones, measured by live-imaging. Bars represent mean ± SD (two independent experiments). Statistical analysis was determined by a two-tailed t test. *ns* = not significant. **(G)** Percentage of cells that died during imaging period in control and CDR2/L double KO clones. Bars represent mean ± SD (two independent experiments). Statistical analysis was determined by a two-tailed t test. *ns* = not significant.

CHAPTER V.

DISCUSSION

DISCUSSION

Dynein is the primary retrograde motor in cells, playing a central role in intracellular transport, as well as the positioning and anchoring of organelle and cellular structures. Dynein is fully active when in complex with dynactin and a cargo adaptor protein. The existence of a variety of cargo adaptors target dynein to the different functions within the cell. In this work, a molecular pathway that recruits dynein to ER sheets and regulates ER organization in a human cancer cell line was identified and dissected. The pathway involves the novel dynein adaptors CDR2 and CDR2L, which use a conserved C-terminal helix to bind an equally well conserved site on the related integral ER membrane proteins KTN1 and p180, configuring the very first described dynein adaptors for the ER.

CDR2 and CDR2L as new dynein adaptors

Dynein activation and cargo specificity are conferred by a diverse set of adaptor proteins, many of which contain conserved motifs such as the CC1 box and HBS1 that mediate interactions with DLIC and DHC, respectively (Celestino *et al.*, 2019; Chaaban & Carter, 2022; Gama *et al.*, 2017; Lee *et al.*, 2018; Sacristan *et al.*, 2018; Schroeder & Vale, 2016). In this work, CDR2 and CDR2L were identified as novel dynein adaptors that contain both CC1 box and HBS1 motifs, and it was demonstrated that they can form a stable dynein-dynactin-adaptor complex in a CC1 box-dependent manner.

As observed for other adaptors such as BICD2 and JIP3, full-length CDR2 and CDR2L may adopt autoinhibited conformations that occlude their N-terminal dynein-binding domains (d'Amico *et al.*, 2022; Hoogenraad *et al.*, 2003; Singh *et al.*, 2024). AF2 structural predictions support this idea, showing that in both CDR2 and CDR2L, the second coiled-coil region folds back onto the N-terminal coiled coil. Consistent with this, full-length CDR2/L were less efficient at crosslinking dynein and dynactin from pig brain lysates compared to their truncated N-terminal constructs (Figure S5A, B). Therefore, N-terminal fragments of CDR2(1–146), CDR2L(1–159), and CDR2L(1–289) were used in all subsequent biochemical assays.

These N-terminal fragments were sufficient to bind dynein and dynactin and promote complex formation *in vitro* (Figure 7B–D; Figure S1C). However, a striking functional difference emerged between CDR2 and CDR2L: while CDR2(1–146) robustly recruited dynein–dynactin complexes (Figure 7D), it did not activate processive movement in motility assays. In contrast, both CDR2L(1–159) and CDR2L(1–289) not only assembled the motor complex but also induced processive movement (Figure 7D, E). To explore this discrepancy, we tested longer CDR2 fragments (CDR2(1–265); (1–289); (1–388)), but these constructs also failed to induce motility (data not shown). These results suggest that

additional regions of CDR2 may be required for activity, or that CDR2, unlike CDR2L, is fundamentally unable to activate motility in this context.

Domain-swapping experiments between CDR2 and CDR2L may help identify the specific residues or structural elements that account for their functional divergence. By exchanging specific domains or residues between CDR2 and CDR2L, it may be possible to pinpoint the features required for dynein activation. These experiments could help clarify whether CDR2 lacks critical structural elements, regulatory sequences, or interaction motifs that are present in CDR2L and necessary for activating dynein motility.

Testing full-length CDR2(1–454) is also a possible experiment; however, it may adopt an autoinhibited conformation that is not relieved *in vitro*. In addition, working with full-length CDR2 is technically more challenging, since the protein has to be expressed in insect cells. Nonetheless, testing full-length CDR2(1–454) in combination with the KTN1 C-terminal fragment might help relieve this autoinhibition and restore activity.

In addition to intrinsic structural features, adaptor conformation may be modulated by environmental factors such as pH. For example, BICD2 adopts a more compact, autoinhibited state at pH 7.0 and transitions to an open, active conformation at pH 8.0 (Fagiewicz *et al.*, 2022). This raises the possibility that adaptor proteins, including CDR2, may require a specific pH range to become motility-competent—an important consideration for future *in vitro* assays, as current assays are performed at pH 7.2. Whether pH-driven conformational changes occur *in vivo* is unknown, but intracellular pH fluctuations could broadly influence adaptor activity. At physiological ER pH (~7.2), CDR2 may adopt a compact, autoinhibited conformation that requires additional signals for activation.

CDR2 function may be modulated by post-translational modifications, which could relieve autoinhibition or enhance interaction with its binding partners. Phosphorylation, in particular, is a well-established regulatory mechanism for dynein adaptors like BICD2, where it modulates conformational states and binding affinities (Fagiewicz *et al.*, 2022; Gallisà-Suñé *et al.*, 2023). Phospho-proteomic datasets report multiple serine and threonine modifications within CDR2 sequence (PhosphoSitePlus, v6.7.9), suggesting that phosphorylation may toggle the protein between inactive and active states. Future work could explore this hypothesis by mutating candidate phosphorylation sites or assessing whether incubation with kinases—particularly with PKN, a reported CDR2 interactor (Takanaga *et al.*, 1998)—enhances CDR2 activity.

Moreover, CDR2 may require additional cofactors or scaffolds, absent in reconstituted systems but present in cells, that promote a functional conformation capable of activating dynein. To further characterize the interactome of the CDR2 N-terminus and identify any additional regulatory elements, pull-down eluates from brain lysates using CDR2(1–146) were subjected to mass spectrometry analysis. Alongside dynein and dynactin subunits,

kinesin-1 components were specifically enriched compared to the control, revealing an unexpected potential interaction (Table S1). This finding suggests that CDR2 may not be exclusively associated with dynein, but could also engage with kinesin-1, potentially contributing to motor coordination or regulation in cells. This aligns with the emerging realization that many cargos are simultaneously associated with dynein and kinesin, coordinated by dual adaptors (Abid Ali *et al.*, 2025; Canty *et al.*, 2023; Cason & Holzbaur, 2022; Celestino *et al.*, 2022; Cmentowski *et al.*, 2023; Kendrick *et al.*, 2019; Splinter *et al.*, 2010). These dual adaptors often contain overlapping or adjacent binding regions for both motors, enabling them to regulate the directionality, activation, or switching of cargo transport. The identification of kinesin-1 in CDR2 complexes raises the possibility that CDR2 functions in a similar way. Therefore, determining the kinesin-1 binding region in CDR2 and exploring its functional relevance will be important for understanding its broader role in intracellular transport.

Although CDR2 does not promote dynein motility *in vitro*, cellular assays indicate that it is able to recruit dynein activity. Expression of full-length CDR2 in CDR2/L double KO cells rescued the ER sheet phenotype, unlike a CC1 box-deleted mutant (Figure 9E–G). Notably, CDR2 also frequently induced clustering of ER sheets near centrosomes (Figure 9E–G), indicating its ability to drive dynein-dependent ER reorganization in cells. One possible explanation for this apparent discrepancy is that the autoinhibited conformation of CDR2 may be relieved by post-translational modifications, binding partners, or specific membrane contexts that are absent in biochemical assays. Supporting this, a JIP3(1–185)::CDR2(188–454) chimera—combining JIP3's dynein-binding domain with CDR2's C-terminal coiled coil—produced more robust and penetrant centrosomal clustering of ER sheets than full-length CDR2 (Figure S3I), consistent with the idea that the native protein is autoinhibited.

In contrast to CDR2, CDR2L is capable of activating dynein-dynactin motility *in vitro*, but fails to restore ER sheet organization when expressed in CDR2/L double KO cells (Figure S2E). This lack of rescue may be due to its more diffuse cytoplasmic distribution or preferential interaction with p180 (Figure 8A), which can reflect alternative functional roles. Accordingly, addressing CDR2L interaction with p180 would help to clarify the molecular mechanisms underlying these functional differences and provide a more comprehensive understanding of how CDR2 and CDR2L contribute to ER dynamics.

A recent study in *D. melanogaster* embryos identified the CDR2 homolog CEN as a dynein adaptor mediating the co-translational transport of its mRNA to centrosomes (Zein-Sabatto *et al.*, 2024, Preprint)—a role that appears evolutionarily divergent from the ER-associated function uncovered here for CDR2/L. Consistent with this, the C-terminal cargo-recognition helices of CDR2/L are conserved in CEN (Figure S2D), whereas the corresponding binding site in the KTN1/p180 homolog Aluminum Tubes is not (data not

shown). This suggests that the ER-associated function of CDR2/L proteins may have emerged later in evolution.

CDR2 and ER sheets: a role mediated by KTN1

To identify potential dynein cargo of CDR2 and CDR2L, immunoprecipitations were performed from HeLa cells extracts stably expressing at near-endogenous levels transgenic GFP::3xFLAG tagged CDR2 or CDR2L in CDR2/L double KO background. This approach was chosen after unsuccessful attempts to generate fluorescently-tagged knock-in cell lines at the endogenous CDR2 and CDR2L loci using two CRISPR strategies, possibly due to the low endogenous expression levels of these genes, which may have hindered the detection and recovery of edited clones.

The identification of KTN1 as an ER receptor for CDR2 (and most likely also CDR2L) suggests that ER sheets are a major site of action for these adaptors. CDR2 directly interacts with KTN1, as demonstrated by recombinant protein binding assays and transient transfection experiments. This interaction is mediated by a conserved C-terminal helix in CDR2 and the C-terminal region of KTN1 (Figure 8D-F; Figure S2D). This mode of cargo binding mirrors that of other dynein adaptors, in which a C-terminal coiled-coil binds cargo, while the N-terminus remains available for assembling with dynein and dynactin (Olenick & Holzbaur, 2019; Reck-Peterson *et al.*, 2018). In cells, endogenous CDR2 was reproducibly detectable by immunofluorescence on ER sheets, although signal intensity varied between cells and was generally close to background levels observed in CDR2 KO cell line (Figure 8C). In contrast, I was unable to detect a specific immunofluorescence signal for CDR2L despite testing multiple antibodies, including one generated during this work, and applying various immunofluorescence protocols. These findings support the notion that CDR2 and CDR2L are expressed at low levels and that their expression may be tightly regulated, possibly restricted to specific physiological conditions or cell types. Although it was initially thought that CDR2 and CDR2L were only expressed in immune-privileged organs, such as the brain, recent studies have shown a broader expression across various human tissues (Kråkenes *et al.*, 2019; Raspotnig *et al.*, 2022; Totland *et al.*, 2011). According to The Human Protein Atlas, both CDR2 and CDR2L are expressed in the brain as well as in other tissues, including the cervix, which is particularly relevant given that HeLa cells are derived from cervical tissue.

O'Donovan and colleagues (2010) reported that CDR2 expression increases in cancer cells during mitosis and is regulated through *de novo* transcription and protein synthesis, as well as by downregulation, at least in part, via APC/C-mediated ubiquitination and proteasomal degradation (O'Donovan *et al.*, 2010). The authors proposed a mitotic role for CDR2, supported by elevated mitotic levels and the formation of multipolar spindles upon

CDR2 knockdown (O'Donovan *et al.*, 2010). In contrast, no significant defects in proliferation or mitotic progression were observed in CDR2/L double KO cells (Figure 13). Nevertheless, the expression of CDR2/L was assessed in interphase and mitosis, revealing elevated protein levels during mitosis, predominantly CDR2 (Figure S5C). This mitotic upregulation is especially intriguing given the dynamic reorganization of the ER during mitosis, when both the nuclear envelope and peripheral ER remodel and reassemble around the mitotic spindle (Obara *et al.*, 2023). In *D. melanogaster* syncytial embryos, ER membranes near spindle poles contribute to spindle architecture and function (Araújo *et al.*, 2022). Nonetheless, no defects in spindle morphology or ER organization during mitosis were detected in the system used in the present work.

Instead, the most striking phenotype was excessive stacking of ER sheets (Figure 9A–C; Figure S3A). This phenotype was KTN1-dependent, as its depletion abolished the stacking phenotype without preventing ER sheet formation itself (Figure 9C, D; S3E) and also destabilized CDR2 protein and its localization to the ER (Figure S2F–H). These results identify KTN1 as a critical ER-localized binding partner that mediates the recruitment and function of CDR2 in ER sheet organization.

KTN1 was first identified through its ability to bind the kinesin motor domain and it has been reported to undergo kinesin-1-mediated transport toward the cell periphery, a process implicated in focal adhesion maturation and cytoskeletal remodeling (Guadagno *et al.*, 2020; Ng *et al.*, 2016; Santama *et al.*, 2004; Toyoshima *et al.*, 1992; Zhang *et al.*, 2010).
In this context, a pool of dynein recruited by CDR2 or CDR2L may act antagonistically to kinesin-1, transporting KTN1 toward the cell center and thereby maintaining its perinuclear localization. This model is supported by our observation that overexpression of CDR2 causes prominent perinuclear clustering of KTN1, consistent with enhanced minus-end–directed motility (Figure 9E, F). However, the effects of CDR2/L double KO diverge from the simple expectation of increased peripheral KTN1 accumulation. Instead of peripheral dispersion, KTN1 accumulates at stacked ER sheets in these cells. These observations suggest that the absence of CDR2/L disrupts the normal regulation of KTN1 transport, leading to its abnormal accumulation at ER sheets rather than promoting its shift to the cell periphery.

The role of kinesin-1 in ER motility, however, remains ambiguous. Some studies reported that downregulation of kinesin-1, using an antisense approach, results in ER clustering around the nucleus, resembling the changes seen upon microtubule depolymerization (Feiguin *et al.*, 1994). Similarly, inhibition of kinesin-1 in mammalian Vero cells, achieved by overexpressing kinesin-1-inhibitory fragments, blocked outward ER tubule movement and increased the proportion of ER sheets in the cell periphery (Woźniak *et al.*, 2009). However, other studies have found that the KO of the kinesin-1 motor subunit KIF5B in mice

does not significantly affect ER morphology (Tanaka *et al.*, 1998), and function-blocking antibodies against kinesin-1 in sea urchin eggs had no noticeable effect on ER structure (Wright *et al.*, 1993). These conflicting findings suggest that kinesin-1's role may vary across cell types or experimental conditions.

This ambiguity surrounding kinesin-1's role in ER dynamics is further complicated by the involvement of dynein in opposing kinesin-1's outward movement. Dynein has been shown to transport ER tubules in various systems, including mammalian and amphibian eggs and the fungus *Ustilago maydis* (Allan, 1995; FitzHarris *et al.*, 2007; Niclas *et al.*, 1996; Perkins & Allan, 2021; Wedlich-Söldner *et al.*, 2002; Woźniak *et al.*, 2009). However, the significance of dynein in ER motility in cultured cells remains debated, as its inhibition does not produce uniform effects across different cell types. For instance, disrupting dynein function by overexpressing the dynactin p50 subunit has no noticeable impact on ER morphology in HeLa cells (Burkhardt *et al.*, 1997; Perkins & Allan, 2021). In contrast, in Vero cells, dynein inhibition leads to the accumulation of ER sheets at the cell periphery, while outward kinesin-driven movement remains unaffected (Burkhardt *et al.*, 1997; Perkins & Allan, 2021; Woźniak *et al.*, 2009). This indicates that dynein's role in ER motility might be context-dependent and cell-type-specific.

Whether and how KTN1-associated kinesin-1 affects this process, and, more broadly, how motor recruitment to the C-terminus of KTN1 functionally relates to its N-terminal microtubule-binding activity, recently reported to control ER distribution (Zheng *et al.*, 2022), are interesting questions for the future. Together, these observations suggest that both kinesin-1 and dynein play dynamic and context-dependent roles in ER motility. The lack of a clear, uniform response to the inhibition or KO of these factors underlines the complexity of ER organization and highlights the need for further studies to unravel the precise molecular mechanisms that govern ER dynamics in different cellular contexts.

CDR2 competes with eEF1Bβ for KTN1 binding

Previous studies have shown that the three isoforms of KIF5 and the eEF1Bβ subunit of the eEF1B directly bind to the C-terminal region of KTN1 (Ong *et al.*, 2000, 2003, 2006). The KIF5 binding region has been mapped to KTN1 residues 1188–1288 (Ong *et al.*, 2000), while CDR2 interaction site was identified within residues 1114–1153 (Figure 8D–F). This means that CDR2 and KIF5 bind to adjacent but distinct, non-overlapping regions of KTN1. In contrast, although eEF1Bβ was known to associate with the C-terminal region of KTN1, the precise binding site on either protein had not been defined. Structure predictions and biochemical assays with recombinant proteins revealed that a helix formed by eEF1Bβ residues 33–60 occupies the same region on KTN1 as the CDR2 C-terminal helix (Figure 11A, B; Figure S4A–C), and that the two proteins compete for binding to KTN1 (Figure 11C).

ER sheets are specialized in protein translation, and it has been proposed that membrane-bound polysomes cooperate with the sheet-enriched membrane proteins KTN1, p180 and CLIMP63 to form segregated rough ER domains in mammalian cells (Shibata *et al.*, 2006, 2010). This process involves polysomes concentrating sheet-enriched proteins, which in turn reinforce polysome localization—a positive feedback loop that promotes sheet stacking (Shibata *et al.*, 2010; Terasaki *et al.*, 2013). If CDR2–dynein–mediated transport of KTN1 along microtubules counteracts its concentration on sheets, it would explain why loss of CDR2/L enhances sheet stacking. Moreover, since eEF1Bβ anchors the eEF1B complex at ER sheets (Ong *et al.*, 2003, 2006), CDR2's competition for KTN1 binding suggests that in the absence of CDR2/L, KTN1 may associate more strongly with polysomes, further promoting sheet stacking. Supporting this idea, preliminary data show that treating CDR2/L double KO cells with puromycin (a translation inhibitor) reduces the percentage of cells with ER patches (52% in control *vs.* 38% in puromycin-treated cells).

Although eEF1Bβ is considerably more abundant than CDR2 in cells, the results presented in this study demonstrate that CDR2 can still compete for KTN1 binding (Figure 11C). This suggests that competition is not governed solely by total protein levels, but may instead rely on local concentration, binding affinities, or context-dependent regulation. For example, CDR2 may be enriched at specific ER subdomains where it locally displaces eEF1Bβ. Alternatively, CDR2 may bind KTN1 with higher affinity or undergo post-translational modifications that enhance binding. Measuring the relative binding affinities of CDR2 and eEF1Bβ for KTN1 would help clarify these possibilities.

Such spatial or conditional regulation could allow cells to dynamically modulate ER architecture in response to changes in translational demand or stress. For instance, during mitosis or nutrient deprivation, global downregulation of translation initiation may reduce eEF1Bβ association with KTN1, permitting CDR2-mediated dynein recruitment and ER redistribution toward the cell center. Conversely, in high-demand secretory states, elevated translation may promote persistent eEF1Bβ–KTN1 association, stabilizing rough ER regions. Thus, the competition between CDR2 and eEF1Bβ may function as a tunable switch linking ER dynamics with the cellular translation state.

Further support for a role of CDR family proteins in translation comes from previous studies implicating CDR2/L in the regulation of gene expression at both transcriptional and translational levels. EM analysis of sera from PCD patients revealed that Yo antibodies, which recognize CDR2/L, localize to the cytoplasm and associate with both membrane-bound and free ribosomes in rat cerebellum (Hida *et al.*, 1994; Rodriguez *et al.*, 1988). More recently, Herdlevær and colleagues showed that CDR2L associates with ribosomes while CDR2 localizes to nuclear speckles in cancer cell lines, using both PCD sera and commercial antibodies (Herdlevær *et al.*, 2020). Through mass spectrometry, super-

resolution microscopy, and proximity ligation assays, they reported that CDR2 co-localizes and potentially interacts with the nuclear speckle proteins SON and eukaryotic initiation factor eIF4A3 (Herdlevær *et al.*, 2020). Notably, eIF4A3 can shuttle to the cytoplasm, where it facilitates mRNA loading onto ribosomes and interacts with ribosomal protein RpS6, which also binds CDR2L (Herdlevær *et al.*, 2020; Rogers *et al.*, 2001; Singh *et al.*, 2012). These findings support a model in which CDR2 is involved in mRNA maturation and export, while CDR2L contributes to translation. Further strengthening this idea, the recent identification of *D. melanogaster* CEN as a dynein adaptor that transports its mRNA and associated ribosomes (Zein-Sabatto *et al.*, 2024, Preprint) hints at the possibility that CDR2/L could facilitate their own translation at the ER. Supporting this, immunoprecipitation performed in this study from GFP::3xFLAG::CDR2 cells was enriched in multiple ribosomal proteins, including components of the large (60S; RPL3, RPL4, RPL6, RPL7, RPL7A) and small (40S; RPS2, RPS9) ribosomal subunits (Table S2). These results are consistent with CDR2 associating, either directly or indirectly, with ribosomes or translation machinery in the cytoplasm.

Taken together, these findings support an overall antagonistic relationship between dynein-driven ER dynamics mediated by CDR2/L and protein synthesis at ER membranes. The higher abundance of eEF1Bβ suggests it may limit CDR2/L access to KTN1, under translation-active conditions, thereby promoting ER sheet stacking. Although the full rationale for such regulatory mechanism remains to be elucidated, it highlights an intriguing intersection between intracellular transport and translational control.

CDR2 and CDR2L in neuronal cells and PCD

CDR2/L are prominently expressed in the mammalian brain (Hwang *et al.*, 2016; Raspotnig *et al.*, 2022). Neurons, with their unique compartmentalized ER organization (Farías *et al.*, 2019; Koppers *et al.*, 2024; Renvoisé & Blackstone, 2010), may thus offer a relevant physiological context in which to further explore the roles of CDR2/L in ER organization. In patients with PCD, the predominant tumor-induced autoantibody present in serum and cerebrospinal fluid is anti-Yo, which recognizes both CDR2/L (Kråkenes *et al.*, 2019; Sakai *et al.*, 1990). Anti-Yo can be internalized by Purkinje cells *in vivo* (Graus *et al.*, 1991; Greenlee *et al.*, 1995), and their interaction with CDR2/L induces Purkinje cell death *in vitro* (Greenlee *et al.*, 2010; Schubert *et al.*, 2014). The study presented in this thesis raises the possibility that the toxicity following anti-Yo uptake stems from pathologic changes in ER organization, a factor implicated in various neurological disorders (Perkins & Allan, 2021; Westrate *et al.*, 2015). EM studies with anti-Yo have indeed demonstrated reactivity with ER-associated antigens (Hida *et al.*, 1994; Rodriguez *et al.*, 1988), and anti-

Yo exposure has been shown to impair calcium homeostasis in Purkinje neurons (Panja *et al.*, 2019; Schubert *et al.*, 2014), a function tightly linked to ER integrity.

In conclusion, the findings presented here establish a direct role for CDR2/L in ER organization and shed light on a previously unrecognized mechanism that may contribute to PCD pathogenesis.

CHAPTER VI.

CONCLUDING REMARKS AND PERSPECTIVES

CONCLUDING REMARKS AND PERSPECTIVES

Since the discovery of dynein nearly four decades ago, it became evident that its broad functional diversity arises from complex and multilayered regulation. In this thesis, CDR2/L were identified as novel dynein adaptors, expanding the repertoire of known regulators of dynein-driven transport. Using HeLa cells, it was demonstrated that these adaptors link dynein to the ER, where they influence ER sheet morphology by modulating the function of the ER membrane protein KTN1. Building on these findings, structural approaches, such as cryo-EM, will be crucial to resolve how CDR2/L engage with dynein, dynactin, and ER-resident proteins at the molecular level, and to better characterize these newly identified adaptors.

Beyond their adaptor function, CDR2 was found to compete with eEF1Bβ, a subunit of the translation elongation machinery, for binding to KTN1. Downregulation of eEF1Bβ enhances CDR2 accumulation on ER sheets and promotes centrosome-proximal clustering of the ER. This reveals a novel layer of crosstalk between the protein translation machinery and ER spatial organization. The molecular mechanisms underlying this competition remain to be fully characterized. Nevertheless, these findings provide a new conceptual framework to investigate how protein synthesis, organelle positioning, and microtubule-based transport are functionally integrated in the cell.

While this work advances our understanding of ER-associated dynein regulation, several open questions remain. Future studies should investigate the distinct contributions of CDR2/L to ER subdomains, their interactions with other ER-resident proteins, and how these roles vary across different cellular contexts. Of particular interest is the potential interplay between CDR2L and p180, a ribosome receptor at the ER, which could position CDR2L within translationally active regions of the ER. This opens an exciting avenue to dissect how ER-bound translation and ER morphology influence one another.

To further dissect these questions, live-cell imaging of ER dynamics will be essential to understanding how CDR2/L influence ER remodeling in real time. Exploring their roles across diverse cell types—particularly those with specialized ER architecture, such as neurons—may uncover cell type-specific functions. The CDR2 and CDR2L single KO models generated in this study also provide a powerful system to dissect their individual contributions with greater resolution.

An additional layer of complexity lies in the possibility that CDR2 interfaces with kinesin motors, raising interesting questions about the balance of bidirectional ER transport and how opposing motors are integrated at the ER surface.

In summary, this thesis identifies two new adaptors that recruit dynein to the ER, uncovers a novel regulatory axis linking translation to ER morphology, and lays the

groundwork for future research into motor-driven ER organization and its broader physiological relevance, particularly in the context of PCD.

CHAPTER VII.

LIST OF REFERENCES

LIST OF REFERENCES

Abbatemarco, J. R., Vedeler, C. A., & Greenlee, J. E. (2024). Paraneoplastic cerebellar and brainstem disorders. *Handbook of Clinical Neurology*, *200*, 173–191. https://doi.org/10.1016/B978-0-12-823912-4.00030-X

Abid Ali, F., Zwetsloot, A. J., Stone, C. E., Morgan, T. E., Wademan, R. F., Carter, A. P., & Straube, A. (2025). KIF1C activates and extends dynein movement through the FHF cargo adapter. *Nature Structural & Molecular Biology*. https://doi.org/10.1038/s41594-024-01418-z

Agrawal, R., Gillies, J. P., Zang, J. L., Zhang, J., Garrott, S. R., Shibuya, H., Nandakumar, J., & DeSantis, M. E. (2022). The KASH5 protein involved in meiotic chromosomal movements is a novel dynein activating adaptor. *ELife*, *11*(e78201). https://doi.org/10.7554/eLife.78201

Allan, V. (1995). Protein Phosphatase 1 Regulates the Cytoplasmic Dynein-driven Formation of Endoplasmic Reticulum Networks In Vitro. *The Journal of Cell Biology*, *128*(5), 879–891. https://doi.org/10.1083/jcb.128.5.879

Amos, L. A. (1989). Brain dynein crossbridges microtubules into bundles. *Journal of Cell Science*, *93*, 19–28. https://doi.org/10.1242/jcs.93.1.19

Araújo, M., Tavares, A., Vieira, D. V., Telley, I. A., & Oliveira, R. A. (2022). Endoplasmic reticulum membranes are continuously required to maintain mitotic spindle size and forces. *Life Science Alliance*, *6*(1). https://doi.org/10.26508/lsa.202201540

Arimoto, M., Koushika, S. P., Choudhary, B. C., Li, C., Matsumoto, K., & Hisamoto, N. (2011). The Caenorhabditis elegans JIP3 Protein UNC-16 Functions As an Adaptor to Link Kinesin-1 with Cytoplasmic Dynein. *The Journal of Neuroscience*, *31*(6), 2216–2224. https://doi.org/10.1523/JNEUROSCI.2653-10.2011

Arruda, A. P., & Parlakgül, G. (2023). Endoplasmic Reticulum Architecture and Inter-Organelle Communication in Metabolic Health and Disease. *Cold Spring Harbor Perspectives in Biology*, *15*(2). https://doi.org/10.1101/cshperspect.a041261

Aslan, M., d'Amico, E. A., Cho, N. H., Taheri, A., Zhao, Y., Zhong, X., Blaauw, M., Carter, A. P., Dumont, S., & Yildiz, A. (2024). Structural and functional insights into activation and regulation of the dynein-dynactin-NuMA complex. *BioRxiv*. https://doi.org/10.1101/2024.11.26.625568

Ayloo, S., Lazarus, J. E., Dodda, A., Tokito, M., Ostap, E. M., & Holzbaur, E. L. F. (2014). Dynactin functions as both a dynamic tether and brake during dynein-driven motility. *Nature Communications*. https://doi.org/10.1038/ncomms5807

Bachmann-Gagescu, R., Dona, M., Hetterschijt, L., Tonnaer, E., Peters, T., De Vrieze, E., Mans, D. A., Van Beersum, S. E. C., Phelps, I. G., Arts, H. H., Keunen, J. E., Ueffing,

M., Roepman, R., Boldt, K., Doherty, D., Moens, C. B., Neuhauss, S. C. F., Kremer, H., Van Wijk, E., & Dutcher, S. K. (2015). The Ciliopathy Protein CC2D2A Associates with NINL and Functions in RAB8-MICAL3-Regulated Vesicle Trafficking. *PLOS Genetics*, *11*((10):e1005575). https://doi.org/10.1371/journal.pgen.1005575

Balamurugan, K., Luu, V. D., Kaufmann, M. R., Hofmann, V. S., Boysen, G., Barth, S., Bordoli, M. R., Stiehl, D. P., Moch, H., Schraml, P., Wenger, R. H., & Camenisch, G. (2009). Onconeuronal cerebellar degeneration-related antigen, Cdr2, is strongly expressed in papillary renal cell carcinoma and leads to attenuated hypoxic response. *Oncogene*, *28*(37), 3274–3285. https://doi.org/10.1038/onc.2009.186

Barlan, K., & Gelfand, V. I. (2017). Microtubule-based transport and the distribution, tethering, and organization of organelles. *Cold Spring Harbor Perspectives in Biology*, *9*(5). https://doi.org/10.1101/cshperspect.a025817

Baumbach, J., Murthy, A., McClintock, M. A., Dix, C. I., Zalyte, R., Hoang, H. T., & Bullock, S. L. (2017). Lissencephaly-1 is a context-dependent regulator of the human dynein complex. *ELife*, *6*(e:21768). https://doi.org/10.7554/eLife.21768.001

Bergalet, J., Patel, D., Legendre, F., Lapointe, C., Benoit Bouvrette, L. P., Chin, A., Blanchette, M., Kwon, E., & Lécuyer, E. (2020). Inter-dependent Centrosomal Co-localization of the cen and ik2 cis-Natural Antisense mRNAs in Drosophila. *Cell Reports*, *30*(10), 3339-3352.e6. https://doi.org/10.1016/j.celrep.2020.02.047

Bhosale, G., Sharpe, J. A., Sundier, S. Y., & Duchen, M. R. (2015). Calcium signaling as a mediator of cell energy demand and a trigger to cell death. *Annals of the New York Academy of Sciences*, *1350*, 107–116. https://doi.org/10.1111/nyas.12885

Bielska, E., Schuster, M., Roger, Y., Berepiki, A., Soanes, D. M., Talbot, N. J., & Steinberg, G. (2014). Hook is an adapter that coordinates kinesin-3 and dynein cargo attachment on early endosomes. *Journal of Cell Biology*, *204*(6), 989–1007. https://doi.org/10.1083/jcb.201309022

Bondarchuk, T. V., Shalak, V. F., Lozhko, D. M., Fatalska, A., Szczepanowski, R. H., Liudkovska, V., Tsuvariev, O. Y., Dadlez, M., El'skaya, A. V., & Negrutskii, B. S. (2022). Quaternary organization of the human eEF1B complex reveals unique multi-GEF domain assembly. *Nucleic Acids Research*, *50*(16), 9490–9504. https://doi.org/10.1093/nar/gkac685

Bragulat-Teixidor, H., Ishihara, K., Szücs, G. M., & Otsuka, S. (2024). The endoplasmic reticulum connects to the nucleus by constricted junctions that mature after mitosis. *EMBO Reports*, *25*(7), 3137–3159. https://doi.org/10.1038/s44319-024-00175-w

Burkhardt, J. K., Echeverri, C. J., Nilsson, T., & Vallee, R. B. (1997). Overexpression of the Dynamitin (p50) Subunit of the Dynactin Complex Disrupts Dynein-dependent

Maintenance of Membrane Organelle Distribution. *The Journal of Cell Biology*, *139*(2), 469–484. https://doi.org/10.1083/jcb.139.2.469

Cantalupo, G., Alifano, P., Roberti, V., Bruni, C. B., & Bucci, C. (2001). Rab-interacting lysosomal protein (RILP): The Rab7 effector required for transport to lysosomes. *EMBO Journal*, *20*(4), 683–693. https://doi.org/10.1093/EMBOJ/20.4.683

Canty, J. T., Hensley, A., Aslan, M., Jack, A., & Yildiz, A. (2023). TRAK adaptors regulate the recruitment and activation of dynein and kinesin in mitochondrial transport. *Nature Communications*, *14*(1376). https://doi.org/10.1038/s41467-023-36945-8

Canty, J. T., & Yildiz, A. (2020). Activation and Regulation of Cytoplasmic Dynein. *Trends in Biochemical Sciences*, *45*(5), 440–453. https://doi.org/10.1016/j.tibs.2020.02.002

Carter, A. P., Diamant, A. G., & Urnavicius, L. (2016). How dynein and dynactin transport cargos: A structural perspective. *Current Opinion in Structural Biology*, *37*, 62–70. https://doi.org/10.1016/j.sbi.2015.12.003

Cason, S. E., Carman, P. J., Van Duyne, C., Goldsmith, J., Dominguez, R., & Holzbaur, E. L. F. (2021). Sequential dynein effectors regulate axonal autophagosome motility in a maturation-dependent pathway. *Journal of Cell Biology*, *220*(7). https://doi.org/10.1083/jcb.202010179

Cason, S. E., & Holzbaur, E. L. F. (2022). Selective motor activation in organelle transport along axons. *Nature Reviews Molecular Cell Biology*. https://doi.org/10.1038/s41580-022-00491-w

Cavalli, V., Kujala, P., Klumperman, J., & Goldstein, L. S. B. (2005). Sunday driver links axonal transport to damage signaling. *Journal of Cell Biology*, *168*(5), 775–787. https://doi.org/10.1083/jcb.200410136

Caviston, J. P., Ross, J. L., Antony, S. M., Tokito, M., & Holzbaur, E. L. F. (2007). Huntingtin facilitates dynein/dynactin-mediated vesicle transport. *Proceedings of the National Academy of Sciences*, *104*(24), 10045–10050. https://doi.org/10.1073/pnas.0610628104

Celestino, R., Gama, J. B., Castro-Rodrigues, A. F., Barbosa, D. J., Rocha, H., d'Amico, E. A., Musacchio, A., Carvalho, A. X., Morais-Cabral, J. H., & Gassmann, R. (2022). JIP3 interacts with dynein and kinesin-1 to regulate bidirectional organelle transport. *Journal of Cell Biology*, *221*(8). https://doi.org/10.1083/jcb.202110057

Celestino, R., Henen, M. A., Gama, J. B., Carvalho, C., McCabe, M., Barbosa, D. J., Born, A., Nichols, P. J., Carvalho, A. X., Gassmann, R., & Vögeli, B. (2019). A transient helix in the disordered region of dynein light intermediate chain links the motor to structurally diverse adaptors for cargo transport. *PLOS Biology*, *17*(1). https://doi.org/10.1371/journal.pbio.3000100

Chaaban, S., & Carter, A. P. (2022). Structure of dynein–dynactin on microtubules shows tandem adaptor binding. *Nature*, *610*(7930), 212–216. https://doi.org/10.1038/s41586-022-05186-y

Cianfrocco, M. A., DeSantis, M. E., Leschziner, A. E., & Reck-Peterson, S. L. (2015). Mechanism and Regulation of Cytoplasmic Dynein. *Annual Review of Cell and Developmental Biology*, *31*, 83–108. https://doi.org/10.1146/annurev-cellbio-100814-125438

Cmentowski, V., Ciossani, G., d'Amico, E., Wohlgemuth, S., Owa, M., Dynlacht, B., & Musacchio, A. (2023). RZZ-Spindly and CENP-E form an integrated platform to recruit dynein to the kinetochore corona. *The EMBO Journal*. https://doi.org/10.15252/embj.2023114838

Colombo, S., Michel, C., Speroni, S., Ruhnow, F., Gili, M., Brito, C., & Surrey, T. (2025). NuMA is a mitotic adaptor protein that activates dynein and connects it to microtubule minus ends. *Journal of Cell Biology*, *224*(4). https://doi.org/10.1083/jcb.202408118

Corradi, J. P., Yang, C., Darnell, J. C., Dalmau, J., & Darnell, R. B. (1997). A Post-Transcriptional Regulatory Mechanism Restricts Expression of the Paraneoplastic Cerebellar Degeneration Antigen cdr2 to Immune Privileged Tissues. *The Journal of Neuroscience*, *17*(4), 1406–1415. https://doi.org/10.1523/JNEUROSCI.17-04-01406.1997

Cui, X. A., Zhang, H., & Palazzo, A. F. (2012). P180 promotes the ribosome-independent localization of a subset of mRNA to the endoplasmic reticulum. *PLoS Biology*, *10*(5). https://doi.org/10.1371/journal.pbio.1001336

Dabora, S. L., & Sheetz, M. F. (1988). The microtubule-dependent formation of a tubulovesicular network with characteristics of the ER from cultured cell extracts. *Cell*, *54*(1), 27–35. https://doi.org/10.1016/0092-8674(88)90176-6

Dalmau, J., & Graus, F. (2012). Paraneoplastic syndromes: from remote to clear and present knowledge. *Brain*, *135*(5), 1650–1653. https://doi.org/10.1093/brain/aws064

Dalmau, J., & Rosenfeld, M. R. (2008). Paraneoplastic syndromes of the CNS. *The Lancet Neurology*, *7*(4), 327–340. https://doi.org/10.1016/S1474-4422(08)70060-7

d'Amico, E. A., Ahmad, M. U. D., Cmentowski, V., Girbig, M., Müller, F., Wohlgemuth, S., Brockmeyer, A., Maffini, S., Janning, P., Vetter, I. R., Carter, A. P., Perrakis, A., & Musacchio, A. (2022). Conformational transitions of the Spindly adaptor underlie its interaction with Dynein and Dynactin. *Journal of Cell Biology*, *221*(11). https://doi.org/10.1083/jcb.202206131

Darnell, J. C., Albert, M. L., & Darnell, R. B. (2000). Cdr2, a target antigen of naturally occuring human tumor immunity, is widely expressed in gynecological tumors. *Cancer Research*, *60*(8), 2136–2139. http://www.ncbi.nlm.nih.gov/pubmed/10786675

Desai, A., Rybina, S., Müller-Reichert, T., Shevchenko, A., Shevchenko, A., Hyman, A., & Oegema, K. (2003). KNL-1 directs assembly of the microtubule-binding interface of the kinetochore in C. elegans. *Genes and Development*, *17*(19), 2421–2435. https://doi.org/10.1101/gad.1126303

Diefenbach, R. J., Diefenbach, E., Douglas, M. W., & Cunningham, A. L. (2004). The ribosome receptor, p180, interacts with kinesin heavy chain, KIF5B. *Biochemical and Biophysical Research Communications*, *319*(3), 987–992. https://doi.org/10.1016/j.bbrc.2004.05.069

Eichler, T. W., Totland, C., Haugen, M., Qvale, T. H., Mazengia, K., Storstein, A., Haukanes, B. I., & Vedeler, C. A. (2013). CDR2L Antibodies: A New Player in Paraneoplastic Cerebellar Degeneration. *PLoS ONE*, *8*(6). https://doi.org/10.1371/journal.pone.0066002

Elshenawy, M. M., Kusakci, E., Volz, S., Baumbach, J., Bullock, S. L., & Yildiz, A. (2020). Lis1 activates dynein motility by modulating its pairing with dynactin. *Nature Cell Biology*, *22*(5), 570–578. https://doi.org/10.1038/s41556-020-0501-4

Endow, S. A., Kull, F. J., & Liu, H. (2010). Kinesins at a glance. *Journal of Cell Science*, *123*(20), 3420–3424. https://doi.org/10.1242/jcs.064113

Fagiewicz, R., Crucifix, C., Klos, T., Deville, C., Kieffer, B., Nominé, Y., Busselez, J., Rossolillo, P., & Schmidt, H. (2022). In vitro characterization of the full-length human dynein-1 cargo adaptor BicD2. *Structure*, *30*(11), 1470-1478.e3. https://doi.org/10.1016/j.str.2022.08.009

Farías, G. G., Fréal, A., Tortosa, E., Stucchi, R., Pan, X., Portegies, S., Will, L., Altelaar, M., & Hoogenraad, C. C. (2019). Feedback-Driven Mechanisms between Microtubules and the Endoplasmic Reticulum Instruct Neuronal Polarity. *Neuron*, *102*(1), 184-201.e8. https://doi.org/10.1016/j.neuron.2019.01.030

Fatima, K., Vihinen, H., Akpinar, B. A., Somborac, T., Jokitalo, E., Katajisto, P., & Konovalova, S. (2024). Ribosome-binding protein 1, RRBP1, maintains peroxisomal biogenesis. In *bioRxiv*. https://doi.org/10.1101/2024.04.10.588905

Feiguin, F., Ferreira, A., Kosik, K. S., & Caceres, A. (1994). Kinesin-mediated organelle translocation revealed by specific cellular manipulations. *The Journal of Cell Biology*, *127*(4), 1021–1039. https://doi.org/10.1083/jcb.127.4.1021

Fellows, A. D., Bruntraeger, M., Burgold, T., Bassett, A. R., & Carter, A. P. (2024). Dynein and dynactin move long-range but are delivered separately to the axon tip. *Journal of Cell Biology*, *223*(5). https://doi.org/10.1083/jcb.202309084

FitzHarris, G., Marangos, P., & Carroll, J. (2007). Changes in endoplasmic reticulum structure during mouse oocyte maturation are controlled by the cytoskeleton and

cytoplasmic dynein. *Developmental Biology*, *305*, 133–144. https://doi.org/10.1016/j.ydbio.2007.02.006

Fumoto, K., Hoogenraad, C. C., & Kikuchi, A. (2006). GSK-3β-regulated interaction of BICD with dynein is involved in microtubule anchorage at centrosome. *The EMBO Journal*, *25*(24), 5670–5682. https://doi.org/10.1038/sj.emboj.7601459

Gallisà-Suñé, N., Sànchez-Fernàndez-de-Landa, P., Zimmermann, F., Serna, M., Regué, L., Paz, J., Llorca, O., Lüders, J., & Roig, J. (2023). BICD2 phosphorylation regulates dynein function and centrosome separation in G2 and M. *Nature Communications*, *14*(1), 2434. https://doi.org/10.1038/s41467-023-38116-1

Gama, J. B., Pereira, C., Simões, P. A., Celestino, R., Barbosa, D., Reis, R. M., Pires, H. R., Carvalho, C., Amorim, J., Carvalho, A. X., Cheerambathur, D. K., & Gassmann, R. (2017). Molecular mechanism of kinetochore dynein recruitment by the Rod/Zw10/Zwilch complex and Spindly. *Journal of Cell Biology*, *216*(4), 943–960. https://doi.org/10.1083/jcb.201610108

Gao, Z., Todorov, B., Barrett, C. F., van Dorp, S., Ferrari, M. D., van den Maagdenberg, A. M. J. M., De Zeeuw, C. I., & Hoebeek, F. E. (2012). Cerebellar Ataxia by Enhanced $Ca_V2.1$ Currents Is Alleviated by Ca^{2+}-Dependent K^+-Channel Activators in *Cacna1a*^{S218L} Mutant Mice. *The Journal of Neuroscience*, *32*(44), 15533–15546. https://doi.org/10.1523/JNEUROSCI.2454-12.2012

Garcia, S. N., & Pereira-Smith, O. (2008). MRGing Chromatin Dynamics and Cellular Senescence. *Cell Biochemistry and Biophysics*, *50*(3), 133–141. https://doi.org/10.1007/s12013-008-9006-7

Garner, K. E. L., Salter, A., Lau, C. K., Gurusaran, M., Villemant, C. M., Granger, E. P., McNee, G., Woodman, P. G., Davies, O. R., Burke, B. E., & Allan, V. J. (2023). The meiotic LINC complex component KASH5 is an activating adaptor for cytoplasmic dynein. *Journal of Cell Biology*, *222*(5). https://doi.org/10.1083/jcb.202204042

Garrott, S. R., Gillies, J. P., & DeSantis, M. E. (2022). Nde1 and Ndel1: Outstanding Mysteries in Dynein-Mediated Transport. *Frontiers in Cell and Developmental Biology*, *10*. https://doi.org/10.3389/fcell.2022.871935

Gassmann, R., Holland, A. J., Varma, D., Wan, X., Filiz, C., Oegema, K., Salmon, E. D., & Desai, A. (2010). Removal of Spindly from microtubule- attached kinetochores controls spindle checkpoint silencing in human cells. *Genes & Development*, *24*, 957–971. https://doi.org/10.1101/gad.1886810

Gibbons, I. R. (1963). STUDIES ON THE PROTEIN COMPONENTS OF CILIA FROM TETRAHYMENA PYRIFORMIS. *Proceedings of the National Academy of Sciences*, *50*(5), 1002–1010. https://doi.org/10.1073/pnas.50.5.1002

Gibbons, I. R., & Rowe, A. J. (1965). Dynein: A Protein with Adenosine Triphosphatase Activity from Cilia. *Science*, *149*(3682), 424–426. https://doi.org/10.1126/science.149.3682.424

Gibson, D. G., Young, L., Chuang, R. Y., Venter, J. C., Hutchison, C. A., & Smith, H. O. (2009). Enzymatic assembly of DNA molecules up to several hundred kilobases. *Nature Methods*, *6*(5), 343–345. https://doi.org/10.1038/nmeth.1318

Gill, S. R., Schroer, T. A., Szilak, I., Steuer, E. R., Sheetz, M. P., & Cleveland, D. W. (1991). Dynactin, a conserved, ubiquitously expressed component of an activator of vesicle motility mediated by cytoplasmic dynein. *The Journal of Cell Biology*, *115*(6), 1639–1650. https://doi.org/10.1083/jcb.115.6.1639

Goodson, H. V., & Jonasson, E. M. (2018). Microtubules and microtubule-associated proteins. *Cold Spring Harbor Perspectives in Biology*, *10*(6). https://doi.org/10.1101/cshperspect.a022608

Goyal, U., & Blackstone, C. (2013). Untangling the web: Mechanisms underlying ER network formation. *Biochimica et Biophysica Acta (BBA) - Molecular Cell Research*, *1833*(11), 2492–2498. https://doi.org/10.1016/j.bbamcr.2013.04.009

Graus, F., Illa, I., Agusti, M., Ribalta, T., Cruz-Sanchez, F., & Juarez, C. (1991). Effect of intraventricular injection of an anti-Purkinje cell antibody (anti-Yo) in a guinea pig model. *Journal of the Neurological Sciences*, *106*(1), 82–87. https://doi.org/10.1016/0022-510X(91)90198-G

Greenlee, J. E., & Brashear, H. R. (1983). Antibodies to cerebellar Purkinje cells in patients with paraneoplastic cerebellar degeneration and ovarian carcinoma. *Annals of Neurology*, *14*(6), 609–613. https://doi.org/10.1002/ana.410140603

Greenlee, J. E., & Brashear, H. R. (2023). The Discovery of Anti-Yo (Anti-PCA1) Antibody in Patients with Paraneoplastic Cerebellar Degeneration: Opening a Window into Autoimmune Neurological Disease. *Cerebellum*, *22*(4), 531–533. https://doi.org/10.1007/s12311-022-01446-9

Greenlee, J. E., Burns, J. B., Rose, J. W., Jaeckle, K. A., & Clawson, S. (1995). Uptake of systemically administered human anticerebellar antibody by rat Purkinje cells following blood-brain barrier disruption. *Acta Neuropathologica*, *89*(4), 341–345. https://doi.org/10.1007/BF00309627

Greenlee, J. E., Carlson, N. G., Abbatemarco, J. R., Herdlevær, I., Clardy, S. L., & Vedeler, C. A. (2022). Paraneoplastic and Other Autoimmune Encephalitides: Antineuronal Antibodies, T Lymphocytes, and Questions of Pathogenesis. In *Frontiers in Neurology* (Vol. 12). Frontiers Media S.A. https://doi.org/10.3389/fneur.2021.744653

Greenlee, J. E., Clawson, S. A., Hill, K. E., Wood, B. L., Tsunoda, I., & Carlson, N. G. (2010). Purkinje Cell Death After Uptake of Anti-Yo Antibodies in Cerebellar Slice Cultures.

Journal of Neuropathology & Experimental Neurology, *69*(10), 997–1007. https://doi.org/10.1097/NEN.0b013e3181f0c82b

Griffis, E. R., Stuurman, N., & Vale, R. D. (2007). Spindly, a novel protein essential for silencing the spindle assembly checkpoint, recruits dynein to the kinetochore. *Journal of Cell Biology*, *177*(6), 1005–1015. https://doi.org/10.1083/jcb.200702062

Grotjahn, D. A., Chowdhury, S., Xu, Y., McKenney, R. J., Schroer, T. A., & Lander, G. C. (2018). Cryo-electron tomography reveals that dynactin recruits a team of dyneins for processive motility. *Nature Structural and Molecular Biology*, *25*, 203–207. https://doi.org/10.1038/s41594-018-0027-7

Guadagno, N. A., Margiotta, A., Bjørnestad, S. A., Haugen, L. H., Kjos, I., Xu, X., Hu, X., Bakke, O., Margadant, F., & Progida, C. (2020). Rab18 regulates focal adhesion dynamics by interacting with kinectin-1 at the endoplasmic reticulum. *Journal of Cell Biology*, *219*(7). https://doi.org/10.1083/JCB.201809020

Guo, X., Farías, G. G., Mattera, R., & Bonifacino, J. S. (2016). Rab5 and its effector FHF contribute to neuronal polarity through dynein-dependent retrieval of somatodendritic proteins from the axon. *Proceedings of the National Academy of Sciences*, *113*(36). https://doi.org/10.1073/pnas.1601844113

Guo, Y., Li, D., Zhang, S., Yang, Y., Liu, J.-J., Wang, X., Liu, C., Milkie, D. E., Moore, R. P., Tulu, U. S., Kiehart, D. P., Hu, J., Lippincott-Schwartz, J., Betzig, E., & Li, D. (2018). Visualizing Intracellular Organelle and Cytoskeletal Interactions at Nanoscale Resolution on Millisecond Timescales. *Cell*, *175*(5), 1430-1442.e17. https://doi.org/10.1016/j.cell.2018.09.057

Ham, H., Huynh, W., Schoon, R. A., Vale, R. D., & Billadeau, D. D. (2015). HkRP3 Is a Microtubule-Binding Protein Regulating Lytic Granule Clustering and NK Cell Killing. *The Journal of Immunology*, *194*, 3984–3996. https://doi.org/10.4049/jimmunol.1402897

Heinrich, L., Bennett, D., Ackerman, D., Park, W., Bogovic, J., Eckstein, N., Petruncio, A., Clements, J., Pang, S., Xu, C. S., Funke, J., Korff, W., Hess, H. F., Lippincott-Schwartz, J., Saalfeld, S., Weigel, A. V., Ali, R., Arruda, R., Bahtra, R., & Nguyen, D. (2021). Whole-cell organelle segmentation in volume electron microscopy. *Nature*, *599*(7883), 141–146. https://doi.org/10.1038/s41586-021-03977-3

Herdlevær, I., Kråkenes, T., Schubert, M., & Vedeler, C. A. (2020). Localization of CDR2L and CDR2 in paraneoplastic cerebellar degeneration. *Annals of Clinical and Translational Neurology*, *7*(11), 2231–2242. https://doi.org/10.1002/acn3.51212

Hida, C., Tsukamoto, T., Awano, H., & Yamamoto, T. (1994). Ultrastructural Localization of Anti-Purkinje Cell Antibody--Binding Sites in Paraneoplastic Cerebellar Degeneration.

Archives of Neurology, *51*(6), 555–558. https://doi.org/10.1001/archneur.1994.00540180033010

Hoogenraad, C. C. (2001). Mammalian Golgi-associated Bicaudal-D2 functions in the dynein-dynactin pathway by interacting with these complexes. *The EMBO Journal*, *20*(15), 4041–4054. https://doi.org/10.1093/emboj/20.15.4041

Hoogenraad, C. C. (2003). Bicaudal D induces selective dynein-mediated microtubule minus end-directed transport. *The EMBO Journal*, *22*(22), 6004–6015. https://doi.org/10.1093/emboj/cdg592

Horgan, C. P., Hanscom, S. R., Jolly, R. S., Futter, C. E., & McCaffrey, M. W. (2010). Rab11-FIP3 links the Rab11 GTPase and cytoplasmic dynein to mediate transport to the endosomal-recycling compartment. *Journal of Cell Science*, *123*(2), 181–191. https://doi.org/10.1242/jcs.052670

Htet, Z. M., Gillies, J. P., Baker, R. W., Leschziner, A. E., DeSantis, M. E., & Reck-Peterson, S. L. (2020). LIS1 promotes the formation of activated cytoplasmic dynein-1 complexes. *Nature Cell Biology*, *22*(5), 518–525. https://doi.org/10.1038/s41556-020-0506-z

Hueschen, C. L., Kenny, S. J., Xu, K., & Dumont, S. (2017). NuMA recruits dynein activity to microtubule minus-ends at mitosis. *ELife*, *6:e29328*. https://doi.org/10.7554/eLife.29328.001

Hughes, C. S., Moggridge, S., Müller, T., Sorensen, P. H., Morin, G. B., & Krijgsveld, J. (2019). Single-pot, solid-phase-enhanced sample preparation for proteomics experiments. *Nature Protocols*, *14*(1), 68–85. https://doi.org/10.1038/s41596-018-0082-x

Hwang, J.-Y., Lee, J., Oh, C.-K., Kang, H. W., Hwang, I.-Y., Um, J. W., Park, H. C., Kim, S., Shin, J.-H., Park, W.-Y., Darnell, R. B., Um, H.-D., Chung, K. C., Kim, K., & Oh, Y. J. (2016). Proteolytic degradation and potential role of onconeural protein cdr2 in neurodegeneration. *Cell Death and Disease*, *7*(e2240). https://doi.org/10.1038/cddis.2016.151

Jaeckle, K. A., Graus, F., Houghton, A., Cardon-Cardo, C., Nielsen, S. L., & Posner, J. B. (1985). Autoimmune response of patients with paraneoplastic cerebellar degeneration to a Purkinje cell cytoplasmic protein antigen. *Annals of Neurology*, *18*(5), 592–600. https://doi.org/10.1002/ana.410180513

Jumper, J., Evans, R., Pritzel, A., Green, T., Figurnov, M., Ronneberger, O., Tunyasuvunakool, K., Bates, R., Žídek, A., Potapenko, A., Bridgland, A., Meyer, C., Kohl, S. A. A., Ballard, A. J., Cowie, A., Romera-Paredes, B., Nikolov, S., Jain, R., Adler, J., … Hassabis, D. (2021). Highly accurate protein structure prediction with AlphaFold. *Nature*. https://doi.org/10.1038/s41586-021-03819-2

Kao, L.-R., & Megraw, T. L. (2009). Centrocortin Cooperates with Centrosomin to Organize Drosophila Embryonic Cleavage Furrows. *Current Biology*, *19*, 937–942. https://doi.org/10.1016/j.cub.2009.04.037

Kardon, J. R., Reck-Peterson, S. L., & Vale, R. D. (2009). Regulation of the processivity and intracellular localization of *Saccharomyces cerevisiae* dynein by dynactin. *Proceedings of the National Academy of Sciences*, *106*(14), 5669–5674. https://doi.org/10.1073/pnas.0900976106

Kaufmann, M. R., Schraml, P., Hermanns, T., Wenger, R. H., & Camenisch, G. (2013). Onconeuronal antigen Cdr2 correlates with HIF prolyl-4-hydroxylase PHD1 and worse prognosis in renal cell carcinoma. *Experimental and Molecular Pathology*, *94*, 453–457. https://doi.org/10.1016/j.yexmp.2013.03.005

Kendrick, A. A., Dickey, A. M., Redwine, W. B., Tran, P. T., Vaites, L. P., Dzieciatkowska, M., Harper, J. W., & Reck-Peterson, S. L. (2019). Hook3 is a scaffold for the opposite-polarity microtubule-based motors cytoplasmic dynein-1 and KIF1C. *Journal of Cell Biology*, *218*(9), 2982–3001. https://doi.org/10.1083/JCB.201812170

Kennel, K. B., Burmeister, J., Schneider, M., & Taylor, C. T. (2018). The PHD1 oxygen sensor in health and disease. In *Journal of Physiology* (Vol. 596, Issue 17, pp. 3899–3913). Blackwell Publishing Ltd. https://doi.org/10.1113/JP275327

King, S. J., & Schroer, T. A. (2000). Dynactin increases the processivity of the cytoplasmic dynein motor. *Nature Cell Biology*, *2*, 20–24. https://doi.org/10.1038/71338

Kinoshita-Kawada, M., Oberdick, J., & Xi Zhu, M. (2004). A Purkinje cell specific GoLoco domain protein, L7/Pcp-2, modulates receptor-mediated inhibition of Ca v2.1 Ca 2+ channels in a dose-dependent manner. *Molecular Brain Research*, *132*(1), 73–86. https://doi.org/10.1016/j.molbrainres.2004.09.007

Koppers, M., Özkan, N., Nguyen, H. H., Jurriens, D., McCaughey, J., Nguyen, D. T. M., Li, C. H., Stucchi, R., Altelaar, M., MacGillavry, H. D., Kapitein, L. C., Hoogenraad, C. C., & Farías, G. G. (2024). Axonal endoplasmic reticulum tubules control local translation via P180/RRBP1-mediated ribosome interactions. *Developmental Cell*, *59*(16), 2053–2068. https://doi.org/10.1016/j.devcel.2024.05.005

Kråkenes, T., Herdlevær, I., Raspotnig, M., Haugen, M., Schubert, M., & Vedeler, C. A. (2019). CDR2L Is the Major Yo Antibody Target in Paraneoplastic Cerebellar Degeneration. *Annals of Neurology*, *86*(2), 316–321. https://doi.org/10.1002/ana.25511

Kumar, J., Yu, H., & Sheetz, M. P. (1995). Kinectin, an Essential Anchor for Kinesin-Driven Vesicle Motility. *Science*, *267*(5205), 1834–1837. https://doi.org/10.1126/science.7892610

Lane, J. D., & Allan, V. J. (1999). Microtubule-based Endoplasmic Reticulum Motility in *Xenopus laevis*: Activation of Membrane-associated Kinesin during Development. *Molecular Biology of the Cell*, *10*(6), 1909–1922. https://doi.org/10.1091/mbc.10.6.1909

Lau, C. K., O'Reilly, F. J., Santhanam, B., Lacey, S. E., Rappsilber, J., & Carter, A. P. (2021). Cryo-EM reveals the complex architecture of dynactin's shoulder region and pointed end. *The EMBO Journal*, *40*(8). https://doi.org/10.15252/embj.2020106164

Lee, I.-G., Cason, S. E., Alqassim, S. S., Holzbaur, E. L. F., & Dominguez, R. (2020). A tunable LIC1-adaptor interaction modulates dynein activity in a cargo-specific manner. *Nature Communications*, *11*(1), 5695. https://doi.org/10.1038/s41467-020-19538-7

Lee, I.-G., Olenick, M. A., Boczkowska, M., Franzini-Armstrong, C., Holzbaur, E. L. F., & Dominguez, R. (2018). A conserved interaction of the dynein light intermediate chain with dynein-dynactin effectors necessary for processivity. *Nature Communications*, *9*(986). https://doi.org/10.1038/s41467-018-03412-8

Leung, J. K., Berube, N., Venable, S., Ahmed, S., Timchenko, N., & Pereira-Smith, O. M. (2001). MRG15 Activates the B-myb Promoter through Formation of a Nuclear Complex with the Retinoblastoma Protein and the Novel Protein PAM14. *Journal of Biological Chemistry*, *276*(42), 39171–39178. https://doi.org/10.1074/jbc.M103435200

Li, X.-J., & Li, S.-H. (2005). HAP1 and intracellular trafficking. *Trends in Pharmacological Sciences*, *26*(1), 1–3. https://doi.org/10.1016/j.tips.2004.11.001

Lozada, P. S. M., Montalvo, R. M., Carrillo, A. I., Montesdeoca-Lozada, M., Rodas, J. A., & Leon-Rojas, J. E. (2025). Roles of CDR2 and CDR2L in Anti-Yo Paraneoplastic Cerebellar Degeneration: A Literature Review. *International Journal of Molecular Sciences*, *26*(1), 70. https://doi.org/10.3390/ijms26010070

Markus, S. M., Marzo, M. G., & McKenney, R. J. (2020). New insights into the mechanism of dynein motor regulation by lissencephaly-1. *ELife*, *9*, 1–27. https://doi.org/10.7554/eLife.59737

Matanis, T., Akhmanova, A., Wulf, P., Del Nery, E., Weide, T., Stepanova, T., Galjart, N., Grosveld, F., Goud, B., De Zeeuw, C. I., Barnekow, A., & Hoogenraad, C. C. (2002). Bicaudal-D regulates COPI-independent Golgi–ER transport by recruiting the dynein–dynactin motor complex. *Nature Cell Biology*, *4*(12), 986–992. https://doi.org/10.1038/ncb891

McKenney, R. J., Huynh, W., Tanenbaum, M. E., Bhabha, G., & Vale, R. D. (2014). Activation of cytoplasmic dynein motility by dynactin-cargo adapter complexes. *Science*, *345*(6194), 337–341. https://doi.org/10.1126/science.1254198

McKinley, K. L., Sekulic, N., Guo, L. Y., Tsinman, T., Black, B. E., & Cheeseman, I. M. (2015). The CENP-L-N Complex Forms a Critical Node in an Integrated Meshwork of

Interactions at the Centromere-Kinetochore Interface. *Molecular Cell*, *60*(6), 886–898. https://doi.org/10.1016/j.molcel.2015.10.027

Merdes, A., Heald, R., Samejima, K., Earnshaw, W. C., & Cleveland, D. W. (2000). Formation of Spindle Poles by Dynein/Dynactin-Dependent Transport of Numa. *The Journal of Cell Biology*, *149*(4), 851–862. https://doi.org/10.1083/jcb.149.4.851

Miki, H., Setou, M., Kaneshiro, K., & Hirokawa, N. (2001). All kinesin superfamily protein, KIF, genes in mouse and human. *Proceedings of the National Academy of Sciences*, *98*(13), 7004–7011. https://doi.org/10.1073/pnas.111145398

Mirdita, M., Schütze, K., Moriwaki, Y., Heo, L., Ovchinnikov, S., & Steinegger, M. (2022). ColabFold: making protein folding accessible to all. *Nature Methods*. https://doi.org/10.1038/s41592-022-01488-1

Montagnac, G., De Forges, H., Smythe, E., Gueudry, C., Romao, M., Salamero, J., & Chavrier, P. (2011). Decoupling of activation and effector binding underlies ARF6 priming of fast endocytic recycling. *Current Biology*, *21*(7), 574–579. https://doi.org/10.1016/j.cub.2011.02.034

Montagnac, G., Sibarita, J. B., Loubéry, S., Daviet, L., Romao, M., Raposo, G., & Chavrier, P. (2009). ARF6 Interacts with JIP4 to Control a Motor Switch Mechanism Regulating Endosome Traffic in Cytokinesis. *Current Biology*, *19*(3), 184–195. https://doi.org/10.1016/j.cub.2008.12.043

Negrutskii, B. (2020). Non-translational Connections of eEF1B in the Cytoplasm and Nucleus of Cancer Cells. *Frontiers in Molecular Biosciences*, *7*(56). https://doi.org/10.3389/fmolb.2020.00056

Negrutskii, B. S., Shalak, V. F., Novosylna, O. V., Porubleva, L. V., Lozhko, D. M., & El'skaya, A. V. (2023). The eEF1 family of mammalian translation elongation factors. *BBA Advances*, *3*. https://doi.org/10.1016/j.bbadva.2022.100067

Ng, I. C., Pawijit, P., Teo, L. Y., Li, H., Lee, S. Y., & Yu, H. (2016). Kinectin-dependent endoplasmic reticulum transport supports focal complex maturation for chemotaxis in shallow gradients. *Journal of Cell Science*, *129*(13), 2660–2672. https://doi.org/10.1242/jcs.181768

Niclas, J., Allan, V. J., & Vale, R. D. (1996). Cell cycle regulation of dynein association with membranes modulates microtubule-based organelle transport. *The Journal of Cell Biology*, *133*(3), 585–593. https://doi.org/10.1083/jcb.133.3.585

Nixon-Abell, J., Obara, C. J., Weigel, A. V., Li, D., Legant, W. R., Xu, C. S., Pasolli, H. A., Harvey, K., Hess, H. F., Betzig, E., Blackstone, C., & Lippincott-Schwartz, J. (2016). Increased spatiotemporal resolution reveals highly dynamic dense tubular matrices in the peripheral ER. *Science*, *354*(6311). https://doi.org/10.1126/science.aaf3928

Obara, C. J., Moore, A. S., & Lippincott-Schwartz, J. (2023). Structural Diversity within the Endoplasmic Reticulum—From the Microscale to the Nanoscale. *Cold Spring Harbor Perspectives in Biology*, *15*(6). https://doi.org/10.1101/cshperspect.a041259

O'Donovan, K. J., Diedler, J., Couture, G. C., Fak, J. J., & Darnell, R. B. (2010). The onconeural antigen cdr2 is a novel APC/C target that acts in mitosis to regulate C-Myc target genes in mammalian tumor cells. *PLoS ONE*, *5*(4). https://doi.org/10.1371/journal.pone.0010045

Okada, K., Iyer, B. R., Lammers, L. G., Gutierrez, P. A., Li, W., Markus, S. M., & McKenney, R. J. (2023). Conserved roles for the dynein intermediate chain and Ndel1 in assembly and activation of dynein. *Nature Communications*, *14*(5833). https://doi.org/10.1038/s41467-023-41466-5

Okano, H. J., Park, W. Y., Corradi, J. P., & Darnell, R. B. (1999). The cytoplasmic Purkinje onconeural antigen cdr2 down-regulates c-Myc function: Implications for neuronal and tumor cell survival. *Genes and Development*, *13*, 2087–2097. https://doi.org/10.1101/gad.13.16.2087

Okuda, H., DeBoer, K., O'Connor, A. E., Merriner, D. J., Jamsai, D., & O'Bryan, M. K. (2017). LRGUK1 is part of a multiprotein complex required for manchette function and male fertility. *FASEB Journal*, *31*(3), 1141–1151. https://doi.org/10.1096/fj.201600909R

Olenick, M. A., & Holzbaur, E. L. F. (2019). Dynein activators and adaptors at a glance. *Journal of Cell Science*, *132*(6). https://doi.org/10.1242/jcs.227132

Olenick, M. A., Tokito, M., Boczkowska, M., Dominguez, R., & Holzbaur, E. L. F. (2016). Hook Adaptors Induce Unidirectional Processive Motility by Enhancing the Dynein-Dynactin Interaction. *Journal of Biological Chemistry*, *291*(35), 18239–18251. https://doi.org/10.1074/jbc.M116.738211

Ong, L. L., Er, C. P. N., Ho, A., Aung, M. T., & Yu, H. (2003). Kinectin anchors the translation elongation factor-1δ to the endoplasmic reticulum. *Journal of Biological Chemistry*, *278*(34), 32115–32123. https://doi.org/10.1074/jbc.M210917200

Ong, L. L., Lim, A. P. C., Er, C. P. N., Kuznetsov, S. A., & Yu, H. (2000). Kinectin-kinesin binding domains and their effects on organelle motility. *Journal of Biological Chemistry*, *275*(42), 32854–32860. https://doi.org/10.1074/jbc.M005650200

Ong, L. L., Lin, P. C., Zhang, X., Chia, S. M., & Yu, H. (2006). Kinectin-dependent assembly of translation elongation factor-1 complex on endoplasmic reticulum regulates protein synthesis. *Journal of Biological Chemistry*, *281*(44), 33621–33634. https://doi.org/10.1074/jbc.M607555200

Osório, H., Silva, C., Ferreira, M., Gullo, I., Máximo, V., Barros, R., Mendonça, F., Oliveira, C., & Carneiro, F. (2021). Proteomics analysis of gastric cancer patients with diabetes

mellitus. *Journal of Clinical Medicine*, *10*(3), 1–14. https://doi.org/10.3390/jcm10030407

Panja, D., Vedeler, C. A., & Schubert, M. (2019). Paraneoplastic cerebellar degeneration: Yo antibody alters mitochondrial calcium buffering capacity. *Neuropathology and Applied Neurobiology*, *45*(2), 141–156. https://doi.org/10.1111/nan.12492

Park, S. H., & Blackstone, C. (2010). Further assembly required: Construction and dynamics of the endoplasmic reticulum network. *EMBO Reports*, *11*(7), 515–521. https://doi.org/10.1038/embor.2010.92

Paschal, B. M., Shpetner, H. S., & Vallee, R. (1987). MAP 1C is a microtubule-activated ATPase which translocates microtubules in vitro and has dynein-like properties. *The Journal of Cell Biology*, *105*(3), 1273–1282. https://doi.org/10.1083/jcb.105.3.1273

Perkins, H. T., & Allan, V. (2021). Intertwined and Finely Balanced: Endoplasmic Reticulum Morphology, Dynamics, Function, and Diseases. *Cells*, *10*(9), 2341. https://doi.org/10.3390/cells10092341

Perkins, H. T., Allan, V. J., & Waigh, T. A. (2021). Network organisation and the dynamics of tubules in the endoplasmic reticulum. *Scientific Reports*, *11*(1). https://doi.org/10.1038/s41598-021-94901-2

Pettersen, E. F., Goddard, T. D., Huang, C. C., Meng, E. C., Couch, G. S., Croll, T. I., Morris, J. H., & Ferrin, T. E. (2021). UCSF ChimeraX: Structure visualization for researchers, educators, and developers. *Protein Science*, *30*(1), 70–82. https://doi.org/10.1002/pro.3943

Plitz, T., & Pfeffer, K. (2001). Intact Lysosome Transport and Phagosome Function Despite Kinectin Deficiency. *Molecular and Cellular Biology*, *21*(17), 6044–6055. https://doi.org/10.1128/mcb.21.17.6044-6055.2001

Pollard, T. D., & Goldman, R. D. (2018). Overview of the Cytoskeleton from an Evolutionary Perspective. *Cold Spring Harbor Perspectives in Biology*, *11(3)*. https://doi.org/10.1101/cshperspect.a030288

Porter, K. R. (1953). OBSERVATIONS ON A SUBMICROSCOPIC BASOPHILIC COMPONENT OF CYTOPLASM. *Journal of Experimental Medicine*, *97*(5), 727–750. https://doi.org/10.1084/jem.97.5.727

Porter, K. R., Claude, A., & Fullam, E. (1945). A study of tissue culture cells by electron microscopy. *Journal of Experimental Medicine*, *86*, 233–246. https://doi.org/doi:10.1084/jem.81.3.233

Porter, K. R., & Palade, G. E. (1957). STUDIES ON THE ENDOPLASMIC RETICULUM. *The Journal of Cell Biology*, *3*(2), 269–300. https://doi.org/10.1083/jcb.3.2.269

Puhka, M., Vihinen, H., Joensuu, M., & Jokitalo, E. (2007). Endoplasmic reticulum remains continuous and undergoes sheet-to-tubule transformation during cell division in

mammalian cells. *Journal of Cell Biology*, *179*(5), 895–909. https://doi.org/10.1083/jcb.200705112

Radulescu, A. E., & Cleveland, D. W. (2010). NuMA after 30 years: the matrix revisited. *Trends in Cell Biology*, *20*(4), 214–222. https://doi.org/10.1016/j.tcb.2010.01.003

Raspotnig, M., Haugen, M., Thorsteinsdottir, M., Stefansson, · Ingunn, Salvesen, H. B., Storstein, A., & Vedeler, C. A. (2017). Cerebellar degeneration-related proteins 2 and 2-like are present in ovarian cancer in patients with and without Yo antibodies. *Cancer Immunology, Immunotherapy*, *66*, 1463–1471. https://doi.org/10.1007/s00262-017-2041-8

Raspotnig, M., Kråkenes, T., Herdlevær, I., Haugen, M., & Vedeler, C. (2022). Expression of cerebellar degeneration-related proteins CDR2 and CDR2L in human and rat brain tissue. *Journal of Neuroimmunology*, *362*. https://doi.org/10.1016/j.jneuroim.2021.577766

Reck-Peterson, S. L., Redwine, W. B., Vale, R. D., & Carter, A. P. (2018). The cytoplasmic dynein transport machinery and its many cargoes. *Nature Reviews Molecular Cell Biology*, *19*(6), 382–398. https://doi.org/10.1038/s41580-018-0004-3

Redwine, W. B., DeSantis, M. E., Hollyer, I., Htet, Z. M., Tran, P. T., Swanson, S. K., Florens, L., Washburn, M. P., & Reck-Peterson, S. L. (2017). The human cytoplasmic dynein interactome reveals novel activators of motility. *ELife*, *6*(e28257). https://doi.org/10.7554/eLife.28257

Renna, C., Rizzelli, F., Carminati, M., Gaddoni, C., Pirovano, L., Cecatiello, V., Pasqualato, S., & Mapelli, M. (2020). Organizational Principles of the NuMA-Dynein Interaction Interface and Implications for Mitotic Spindle Functions. *Structure*, *28*(7), 820-829.e6. https://doi.org/10.1016/j.str.2020.04.017

Renvoisé, B., & Blackstone, C. (2010). Emerging themes of ER organization in the development and maintenance of axons. *Current Opinion in Neurobiology*, *20*, 531–537. https://doi.org/10.1016/j.conb.2010.07.001

Richter, J. D., & Zhao, X. (2021). The molecular biology of FMRP: new insights into fragile X syndrome. *Nature Reviews Neuroscience*, *22*(4), 209–222. https://doi.org/10.1038/s41583-021-00432-0

Roberts, A. J. (2018). Emerging mechanisms of dynein transport in the cytoplasm versus the cilium. *Biochemical Society Transactions*, *46*, 967–982. https://doi.org/10.1042/BST20170568

Roberts, A. J., Kon, T., Knight, P. J., Sutoh, K., & Burgess, S. A. (2013). Functions and mechanics of dynein motor proteins. *Nature Reviews Molecular Cell Biology*, *14*, 713–726. https://doi.org/10.1038/nrm3667

Rodriguez, M., Truh, L. I., O'Neill, B. P., & Lennon, V. A. (1988). Autoimmune paraneoplastic cerebellar degeneration: Ultrastructural localization of antibody-binding sites in Purkinje cells. *Neurology*, *38*(9), 1380–1380. https://doi.org/10.1212/WNL.38.9.1380

Rogers, G. W., Richter, N. J., Lima, W. F., & Merrick, W. C. (2001). Modulation of the Helicase Activity of eIF4A by eIF4B, eIF4H, and eIF4F. *Journal of Biological Chemistry*, *276*(33), 30914–30922. https://doi.org/10.1074/jbc.M100157200

Ross, J. L., Wallace, K., Shuman, H., Goldman, Y. E., & Holzbaur, E. L. F. (2006). Processive bidirectional motion of dynein-dynactin complexes in vitro. *Nature Cell Biology*, *8*(6), 562–570. https://doi.org/10.1038/ncb1421

Ryder, P. V., Fang, J., & Lerit, D. A. (2020). Centrocortin RNA localization to centrosomes is regulated by FMRP and facilitates error-free mitosis. *Journal of Cell Biology*, *219*(12). https://doi.org/10.1083/JCB.202004101

Sacristan, C., Ahmad, M. U. D., Keller, J., Fermie, J., Groenewold, V., Tromer, E., Fish, A., Melero, R., Carazo, J. M., Klumperman, J., Musacchio, A., Perrakis, A., & Kops, G. J. (2018). Dynamic kinetochore size regulation promotes microtubule capture and chromosome biorientation in mitosis. *Nature Cell Biology*, *20*(7), 800–810. https://doi.org/10.1038/s41556-018-0130-3

Sakai, K., Kitagawa, Y., Saiki, S., Saiki, M., & Hirose, G. (2004). Effect of a paraneoplastic cerebellar degeneration-associated neural protein on B-myb promoter activity. *Neurobiology of Disease*, *15*, 529–533. https://doi.org/10.1016/j.nbd.2003.11.003

Sakai, K., Mitchell, D. J., Tsukamoto, T., & Steinman, L. (1990). Isolation of a complementary DNA clone encoding an autoantigen recognized by an anti-neuronal cell antibody from a patient with paraneoplastic cerebellar degeneration. *Annals of Neurology*, *28*(5), 692–698. https://doi.org/10.1002/ana.410280515

Sakai, K., Ogasawara, T., Hirose, G., Jaeckle, K. A., & Greenlee, J. E. (1993). Analysis of autoantibody binding to 52-kd paraneoplastic cerebellar degeneration–associated antigen expressed in recombinant proteins. *Annals of Neurology*, *33*(4), 373–380. https://doi.org/10.1002/ana.410330407

Sakai, K., Shirakawa, T., Li, Y., Kitagawa, Y., & Hirose, G. (2002). Interaction of a Paraneoplastic Cerebellar Degeneration-Associated Neuronal Protein with the Nuclear Helix-Loop-Helix Leucine Zipper Protein MRG X. *Molecular and Cellular Neuroscience*, *19*(4), 477–484. https://doi.org/10.1006/mcne.2001.1059

Sanjana, N. E., Shalem, O., & Zhang, F. (2014). Improved vectors and genome-wide libraries for CRISPR screening. In *Nature Methods* (Vol. 11, Issue 8, pp. 783–784). Nature Publishing Group. https://doi.org/10.1038/nmeth.3047

Santama, N., Er, C. P. N., Ong, L. L., & Yu, H. (2004). Distribution and functions of kinectin isoforms. *Journal of Cell Science*, *117*(19), 4537–4549. https://doi.org/10.1242/jcs.01326

Sawyer, E. M., Jensen, L. E., Meehl, J. B., Larsen, K. P., Petito, D. A., Hurley, J. H., & Voeltz, G. K. (2024). SigmaR1 shapes rough endoplasmic reticulum membrane sheets. *Developmental Cell*. https://doi.org/10.1016/j.devcel.2024.06.005

Scherer, J., Yi, J., & Vallee, R. B. (2014). PKA-dependent dynein switching from lysosomes to adenovirus: A novel form of host-virus competition. *Journal of Cell Biology*, *205*(2), 163–177. https://doi.org/10.1083/jcb.201307116

Schlager, M. A., Hoang, H. T., Urnavicius, L., Bullock, S. L., & Carter, A. P. (2014). In vitro reconstitution of a highly processive recombinant human dynein complex. *The EMBO Journal*, *33*, 1855–1868. https://doi.org/10.15252/embj.201488792

Schlager, M. A., Kapitein, L. C., Grigoriev, I., Burzynski, G. M., Wulf, P. S., Keijzer, N., de Graaff, E., Fukuda, M., Shepherd, I. T., Akhmanova, A., & Hoogenraad, C. C. (2010). Pericentrosomal targeting of Rab6 secretory vesicles by Bicaudal-D-related protein 1 (BICDR-1) regulates neuritogenesis. *The EMBO Journal*, *29*(10), 1637–1651. https://doi.org/10.1038/emboj.2010.51

Schlager, M. A., Serra-Marques, A., Grigoriev, I., Gumy, L. F., Esteves da Silva, M., Wulf, P. S., Akhmanova, A., & Hoogenraad, C. C. (2014). Bicaudal D Family Adaptor Proteins Control the Velocity of Dynein-Based Movements. *Cell Reports*, *8*(5), 1248–1256. https://doi.org/10.1016/j.celrep.2014.07.052

Schroeder, C. M., & Vale, R. D. (2016). Assembly and activation of dynein–dynactin by the cargo adaptor protein Hook3. *Journal of Cell Biology*, *214*(3), 309–318. https://doi.org/10.1083/jcb.201604002

Schroeder, L. K., Barentine, A. E. S., Merta, H., Schweighofer, S., Zhang, Y., Baddeley, D., Bewersdorf, J., & Bahmanyar, S. (2019). Dynamic nanoscale morphology of the ER surveyed by STED microscopy. *Journal of Cell Biology*, *218*(1), 83–96. https://doi.org/10.1083/jcb.201809107

Schroer, T. A. (2004). DYNACTIN. *Annual Review of Cell and Developmental Biology*, *20*, 759–779. https://doi.org/10.1146/annurev.cellbio.20.012103.094623

Schroer, T. A., & Sheetz, M. P. (1991). Two activators of microtubule-based vesicle transport. *The Journal of Cell Biology*, *115*(5), 1309–1318. https://doi.org/10.1083/jcb.115.5.1309

Schubert, M., Panja, D., Haugen, M., Bramham, C. R., & Vedeler, C. A. (2014). Paraneoplastic CDR2 and CDR2L antibodies affect Purkinje cell calcium homeostasis. *Acta Neuropathologica*, *128*(6), 835–852. https://doi.org/10.1007/s00401-014-1351-6

Schwaller, B. (2012). The use of transgenic mouse models to reveal the functions of Ca2+ buffer proteins in excitable cells. *Biochimica et Biophysica Acta (BBA) - General Subjects*, *1820*(8), 1294–1303. https://doi.org/10.1016/j.bbagen.2011.11.008

Schwarz, D. S., & Blower, M. D. (2016). The endoplasmic reticulum: structure, function and response to cellular signaling. *Cellular and Molecular Life Sciences*, *73*, 79–94. https://doi.org/10.1007/s00018-015-2052-6

Shalem, O., Sanjana, N. E., Hartenian, E., Shi, X., Scott, D. A., Mikkelsen, T. S., Heckl, D., Ebert, B. L., Root, D. E., Doench, J. G., & Zhang, F. (2014). Genome-scale CRISPR-Cas9 knockout screening in human cells. *Science*, *343*(6166), 84–87. https://doi.org/10.1126/science.1247005

Shams'Ili, S., Grefkens, J., De Leeuw, B., Van den Bent, M., Hooijkaas, H., Van der Holt, B., Vecht, C., & Sillevis Smitt, P. (2003). Paraneoplastic cerebellar degeneration associated with antineuronal antibodies: analysis of 50 patients. *Brain*, *126*(6), 1409–1418. https://doi.org/10.1093/BRAIN/AWG133

Shemesh, T., Klemm, R. W., Romano, F. B., Wang, S., Vaughan, J., Zhuang, X., Tukachinsky, H., Kozlov, M. M., & Rapoport, T. A. (2014). A model for the generation and interconversion of ER morphologies. *Proceedings of the National Academy of Sciences of the United States of America*, *111*(49), E5243–E5251. https://doi.org/10.1073/pnas.1419997111

Shibata, Y., Hu, J., Kozlov, M. M., & Rapoport, T. A. (2009). Mechanisms Shaping the Membranes of Cellular Organelles. *Annual Review of Cell and Developmental Biology*, *25*(1), 329–354. https://doi.org/10.1146/annurev.cellbio.042308.113324

Shibata, Y., Shemesh, T., Prinz, W. A., Palazzo, A. F., Kozlov, M. M., & Rapoport, T. A. (2010). Mechanisms Determining the Morphology of the Peripheral ER. *Cell*, *143*, 774–788. https://doi.org/10.1016/j.cell.2010.11.007

Shibata, Y., Voeltz, G. K., & Rapoport, T. A. (2006). Rough Sheets and Smooth Tubules. In *Cell* (Vol. 126, Issue 3, pp. 435–439). Elsevier B.V. https://doi.org/10.1016/j.cell.2006.07.019

Singh, G., Kucukural, A., Cenik, C., Leszyk, J. D., Shaffer, S. A., Weng, Z., & Moore, M. J. (2012). The cellular EJC interactome reveals higher-order mRNP structure and an EJC-SR protein nexus. *Cell*, *151*(4), 750–764. https://doi.org/10.1016/j.cell.2012.10.007

Singh, K., Lau, C. K., Manigrasso, G., Gama, J. B., Gassmann, R., & Carter, A. P. (2024). Molecular mechanism of dynein-dynactin complex assembly by LIS1. *Science*, *383*(6690). https://doi.org/10.1126/science.adk8544

Solheim, E. T., Gerking, Y., Kråkenes, T., Herdlevær, I., Birkeland, E., Totland, C., Dick, F., & Vedeler, C. A. (2024). Multi-omics profiling reveals dysregulated ribosome

biogenesis and impaired cell proliferation following knockout of CDR2L. *BMC Cancer*, *24*(1), 645. https://doi.org/10.1186/s12885-024-12399-z

Splinter, D., Tanenbaum, M. E., Lindqvist, A., Jaarsma, D., Flotho, A., Yu, K. Lou, Grigoriev, I., Engelsma, D., Haasdijk, E. D., Keijzer, N., Demmers, J., Fornerod, M., Melchior, F., Hoogenraad, C. C., Medema, R. H., & Akhmanova, A. (2010). Bicaudal D2, dynein, and kinesin-1 associate with nuclear pore complexes and regulate centrosome and nuclear positioning during mitotic entry. *PLoS Biology*, *8*(4). https://doi.org/10.1371/journal.pbio.1000350

Sweeney, H. L., & Holzbaur, E. L. F. (2018). Motor Proteins. *Cold Spring Harbor Perspectives in Biology*, *10:a021931*. https://doi.org/10.1101/cshperspect.a021931

Szebenyi, G., Wigley, W. C., Hall, B., Didier, A., Yu, M., Thomas, P., & Krämer, H. (2007). Hook2 contributes to aggresome formation. *BMC Cell Biology*, *8*. https://doi.org/10.1186/1471-2121-8-19

Takanaga, H., Mukai, H., Shibata, H., Toshimori, M., & Ono, Y. (1998). PKN Interacts with a Paraneoplastic Cerebellar Degeneration-Associated Antigen, Which Is a Potential Transcription Factor. *Experimental Cell Research*, *241*(2), 363–372. https://doi.org/10.1006/excr.1998.4060

Tanaka, Y., Kanai, Y., Okada, Y., Nonaka, S., Takeda, S., Harada, A., & Hirokawa, N. (1998). Targeted Disruption of Mouse Conventional Kinesin Heavy Chain kif5B, Results in Abnormal Perinuclear Clustering of Mitochondria. *Cell*, *93*(7), 1147–1158. https://doi.org/10.1016/S0092-8674(00)81459-2

Teixeira, V., Singh, K., Gama, J. B., Moreira, M., Celestino, R., Xavier Carvalho, A., Pereira, P. S., Abreu, C. M. C., Dantas, T. J., Carter, A. P., & Gassmann, R. (2025). CDR2 is a dynein adaptor recruited by kinectin to regulate ER sheet organization. *Journal of Cell Biology*, *224*(9). https://doi.org/10.1083/jcb.202411034

Terasaki, M., Shemesh, T., Kasthuri, N., Klemm, R. W., Schalek, R., Hayworth, K. J., Hand, A. R., Yankova, M., Huber, G., Lichtman, J. W., Rapoport, T. A., & Kozlov, M. M. (2013). Stacked Endoplasmic Reticulum Sheets Are Connected by Helicoidal Membrane Motifs. *Cell*, *154*, 285–296. https://doi.org/10.1016/j.cell.2013.06.031

Thawani, A., & Petry, S. (2021). Molecular insight into how γ-TuRC makes microtubules. *Journal of Cell Biology*, *134 (14): jcs245464*. https://doi.org/10.1242/jcs.245464

Todorov, B., Kros, L., Shyti, R., Plak, P., Haasdijk, E. D., Raike, R. S., Frants, R. R., Hess, E. J., Hoebeek, F. E., De Zeeuw, C. I., & Van Den Maagdenberg, A. M. J. M. (2012). Purkinje cell-specific ablation of CaV2.1 Channels is sufficient to cause cerebellar ataxia in mice. *Cerebellum*, *11*(1), 246–258. https://doi.org/10.1007/s12311-011-0302-1

Totland, C., Aarskog, N. K., Eichler, T. W., Haugen, M., Nøstbakken, J. K., Sissel, •, Monstad, E., Salvesen, H. B., Mørk, S., Bjørn, •, Haukanes, I., & Vedeler, C. A. (2011). CDR2 antigen and Yo antibodies. *Cancer Immunology, Immunotherapy*, *60*, 283–289. https://doi.org/10.1007/s00262-010-0943-9

Totland, C., Kråkenes, T., Mazengia, K., Haugen, M., & Vedeler, C. (2018). Expression of the onconeural protein CDR1 in cerebellum and ovarian cancer. *Oncotarget*, *9*(35), 23975–23986. https://doi.org/10.18632/oncotarget.25252

Totland, C., Ying, M., Haugen, M., Kibret Mazengia, •, Storstein, A., Aarseth, J., Martinez, A., & Vedeler, C. (2013). Avidity of onconeural antibodies is of clinical relevance. *Cancer Immunology, Immunotherapy*, *62*, 1393–1396. https://doi.org/10.1007/s00262-013-1442-6

Toyoshima, I., Yu, H., Steuer, E. R., & Sheetz, M. P. (1992). Kinectin, a Major Kinesin-binding Protein on ER. *The Journal of Cell Biology*, *118*, 1121–1131. http://rupress.org/jcb/article-pdf/118/5/1121/1063429/1121.pdf

Tripathy, S. K., Weil, S. J., Chen, C., Anand, P., Vallee, R. B., & Gross, S. P. (2014). Autoregulatory mechanism for dynactin control of processive and diffusive dynein transport. *Nature Cell Biology*, *16*(12), 1192–1201. https://doi.org/10.1038/ncb3063

Trokter, M., Mučkec, N., & Surrey, T. (2012). Reconstitution of the human cytoplasmic dynein complex. *Proceedings of the National Academy of Sciences of the United States of America*, *109*(51), 20895–20900. https://doi.org/10.1073/pnas.1210573110

Urnavicius, L., Lau, clinton K., Elshenawy, M. M., Morales-Rios, E., Motz, carina, Yildiz, A., & Carter, A. P. (2018). Cryo-EM shows how dynactin recruits two dyneins for faster movement. *Nature*, *554*, 202–206. https://doi.org/10.1038/nature25462

Urnavicius, L., Zhang, K., Diamant, A. G., Motz, C., Schlager, M. A., Yu, M., Patel, N. A., Robinson, C. V., & Carter, A. P. (2015). The structure of the dynactin complex and its interaction with dynein. *Science*, *347*(6229), 1441–1446. https://doi.org/10.1126/science.aaa4080

van Spronsen, M., Mikhaylova, M., Lipka, J., Schlager, M. A., van den Heuvel, D. J., Kuijpers, M., Wulf, P. S., Keijzer, N., Demmers, J., Kapitein, L. C., Jaarsma, D., Gerritsen, H. C., Akhmanova, A., & Hoogenraad, C. C. (2013). TRAK/Milton Motor-Adaptor Proteins Steer Mitochondrial Trafficking to Axons and Dendrites. *Neuron*, *77*(3), 485–502. https://doi.org/10.1016/j.neuron.2012.11.027

Venkatraman, A., & Opal, P. (2016). Paraneoplastic cerebellar degeneration with anti-Yo antibodies – a review. *Annals of Clinical and Translational Neurology*, *3*(8), 655–663. https://doi.org/10.1002/acn3.328

Voeltz, G. K., Prinz, W. A., Shibata, Y., Rist, J. M., & Rapoport, T. A. (2006). A class of membrane proteins shaping the tubular endoplasmic reticulum. *Cell*, *124*(3), 573–586. https://doi.org/10.1016/j.cell.2005.11.047

Walenta, J. H., Didier, A. J., Liu, X., & Krämer, H. (2001). The Golgi-Associated Hook3 Protein Is a Member of a Novel Family of Microtubule-Binding Proteins. *The Journal of Cell Biology*, *152*(5), 923–934. https://doi.org/10.1083/jcb.152.5.923

Wang, Y., Huynh, W., Skokan, T. D., Lu, W., Weiss, A., & Vale, R. D. (2019). CRACR2a is a calcium-activated dynein adaptor protein that regulates endocytic traffic. *Journal of Cell Biology*, *218*(5), 1619–1633. https://doi.org/10.1083/jcb.201806097

Wedlich-Söldner, R., Schulz, I., Straube, A., & Steinberg, G. (2002). Dynein Supports Motility of Endoplasmic Reticulum in the Fungus *Ustilago maydis*. *Molecular Biology of the Cell*, *13*(3), 965–977. https://doi.org/10.1091/mbc.01-10-0475

Westrate, L. M., Lee, J. E., Prinz, W. A., & Voeltz, G. K. (2015). Form Follows Function: The Importance of Endoplasmic Reticulum Shape. *Annual Reviews*, *84*, 791–811. https://doi.org/10.1146/annurev-biochem-072711-163501

Wickstead, B., & Gull, K. (2007). Dyneins Across Eukaryotes: A Comparative Genomic Analysis. *Traffic*, *8*, 1708–1721. https://doi.org/10.1111/j.1600-0854.2007.00646.x

Woźniak, M. J., & Allan, V. J. (2006). Cargo selection by specific kinesin light chain 1 isoforms. *The EMBO Journal*, *25*(23), 5457–5468. https://doi.org/10.1038/sj.emboj.7601427

Woźniak, M. J., Bola, B., Brownhill, K., Yang, Y.-C., Levakova, V., & Allan, V. J. (2009). Role of kinesin-1 and cytoplasmic dynein in endoplasmic reticulum movement in VERO cells. *The Journal of Cell Biology*, *122*(12), 1979–1989. https://doi.org/10.1242/jcs.041962

Wright, B. D., Terasaki, M., & Scholey, J. M. (1993). Roles of kinesin and kinesin-like proteins in sea urchin embryonic cell division: evaluation using antibody microinjection. *The Journal of Cell Biology*, *123*(3), 681–689. https://doi.org/10.1083/jcb.123.3.681

Xu, H., Yu, S., Peng, K., Gao, L., Chen, S., Shen, Z., Han, Z., Chen, M., Lin, J., Chen, S., & Kang, M. (2021). The role of EEF1D in disease pathogenesis: a narrative review. *Annals of Translational Medicine*, *9*(20), 1600–1600. https://doi.org/10.21037/atm-21-5025

Yeh, T.-Y., Quintyne, N. J., Scipioni, B. R., Eckley, D. M., & Schroer, T. A. (2012). Dynactin's pointed-end complex is a cargo-targeting module. *Molecular Biology of the Cell*, *23*(19), 3827–3837. https://doi.org/10.1091/mbc.e12-07-0496

Zein-Sabatto, H., Brockett, J. S., Husbands, C. A., Lee, J., Fang, J., Buehler, J., Bullock, S. L., & Lerit, D. A. (2024). Centrocortin potentiates co-translational localization of its

mRNA to the centrosome via dynein. *BioRxiv*. https://doi.org/10.1101/2024.08.09.607365

Zhang, H., & Hu, J. (2016). Shaping the Endoplasmic Reticulum into a Social Network. *Trends in Cell Biology*, *26*(12), 934–943. https://doi.org/10.1016/j.tcb.2016.06.002

Zhang, K., Foster, H. E., Rondelet, A., Lacey, S. E., Bahi-Buisson, N., Bird, A. W., & Carter, A. P. (2017). Cryo-EM Reveals How Human Cytoplasmic Dynein Is Auto-inhibited and Activated. *Cell*, *169*(7), 1303-1314.e18. https://doi.org/10.1016/j.cell.2017.05.025

Zhang, X., Tee, Y. H., Heng, J. K., Zhu, Y., Hu, X., Margadant, F., Ballestrem, C., Bershadsky, A., Griffiths, G., & Yu, H. (2010). Kinectin-mediated endoplasmic reticulum dynamics supports focal adhesion growth in the cellular lamella. *Journal of Cell Science*, *123*(22), 3901–3912. https://doi.org/10.1242/jcs.069153

Zheng, P., Obara, C. J., Szczesna, E., Nixon-Abell, J., Mahalingan, K. K., Roll-Mecak, A., Lippincott-Schwartz, J., & Blackstone, C. (2022). ER proteins decipher the tubulin code to regulate organelle distribution. *Nature*, *601*(7891), 132–138. https://doi.org/10.1038/s41586-021-04204-9

Zucker, B., & Kozlov, M. M. (2022). Mechanism of shaping membrane nanostructures of endoplasmic reticulum. *Proceedings of the National Academy of Sciences*, *119*(1). https://doi.org/10.1073/pnas.2116142119

CHAPTER VIII.

SUPPLEMENTARY MATERIAL

SUPPLEMENTARY MATERIAL

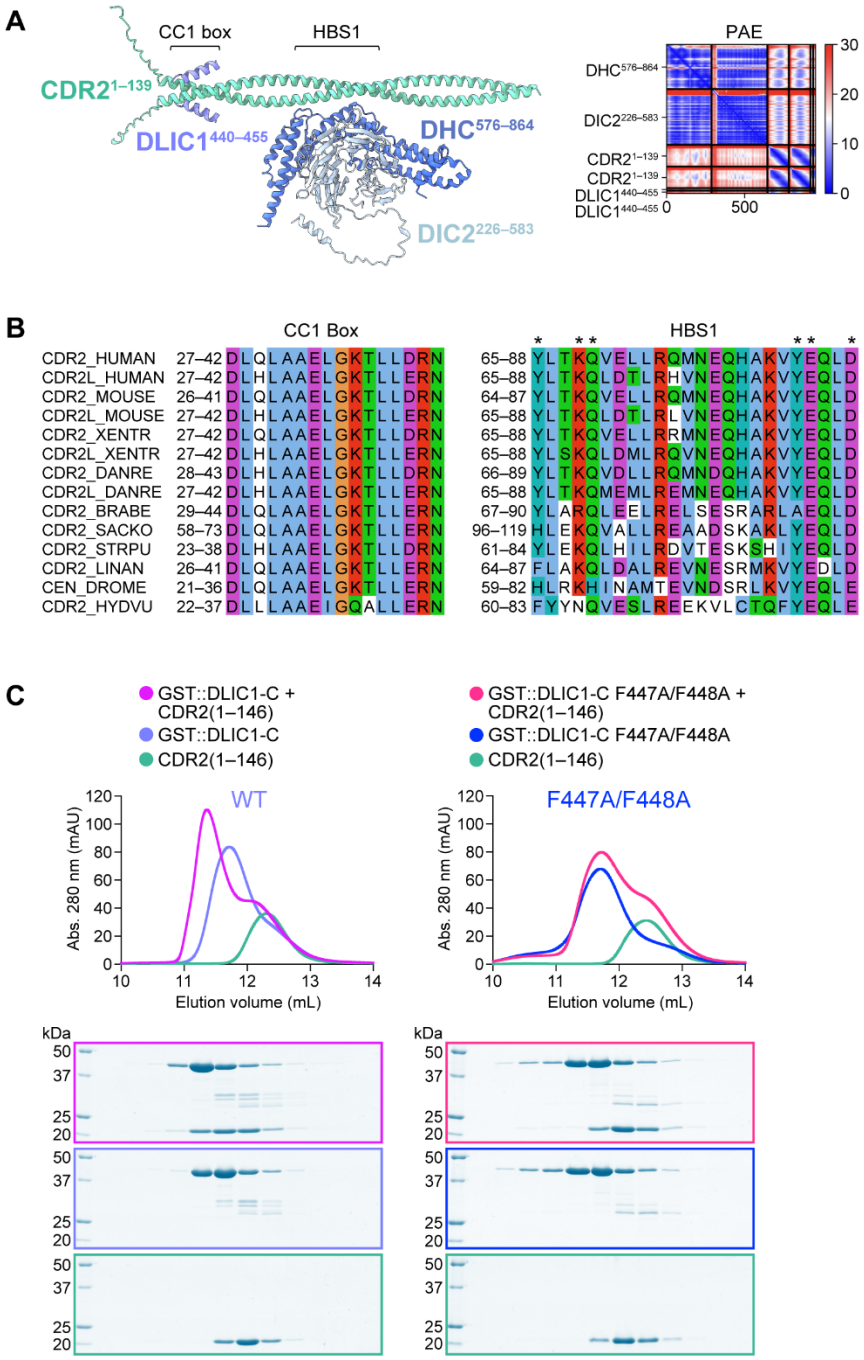

Figure S1 – Related to Figure 7 (CDR2's interaction with dynein).

(A) AF2 model and PAE plot of the CDR2 N-terminal coiled-coil in complex with the DLIC1 C-terminal helix and an N-terminal DHC fragment, which in turn is bound to the WD40 domain of DIC2. *(continued on the next page)*

Figure S1 *(continued)* – Related to Figure 7 (CDR2's interaction with dynein).

(B) Sequence alignment of the CC1 box and the dynein heavy chain binding site 1 (HBS1) in CDR2 and CDR2L proteins from different species (invertebrates possess a single CDR2/CDR2L homolog). The HBS1 sequence is divergent from that of other adaptors but the interaction is predicted at the correct distance from the CC1 box. 6 residues, marked with asterisks, were mutated to alanine (HBS1_6A mutant) based on sequence conservation among CDR2 proteins and their position in the predicted structure. Accession numbers: CDR2_HUMAN (UniProt Q01850), CDR2L_HUMAN (UniProt Q86X02), CDR2_MOUSE (UniProt P97817), CDR2L_MOUSE (UniProt A2A6T1), CDR2_XENTR (UniProt F6R4S1), CDR2L_XENTR (UniProt A0A803JSM3), CDR2_DANRE (UniProt E7FC97), CDR2L_DANRE (UniProt Q6NZT2), CDR2_BRABE (UniProt A0A6P4ZS94), CDR2_SACKO (NCBI Reference Sequence XP_002736317.2), CDR2_STRPU (UniProt A0A7M7NRE1), CDR2_LINAN (NCBI Reference Sequence XP_013392376.1), CEN_DROME (UniProt Q9VIK6), CDR2_HYDVU (UniProt A0A8B6XII3). Species key (Phylum): HUMAN, *Homo sapiens* (Chordata); MOUSE, *Mus musculus* (Chordata); XENTR, *Xenopus tropicalis* (Chordata); DANRE, *Danio rerio* (Chordata); BRABE, *Branchiostoma belcheri* (Chordata); SACKO, *Saccoglossus kowalevskii* (Hemichordata); STRPU, *Strongylocentrotus purpuratus* (Echinodermata); LINAN, *Lingula anatina* (Brachiopoda); DROME, *Drosophila melanogaster* (Arthropoda); HYDVU, *Hydra vulgaris* (Cnidaria). **(C)** Elution profiles and BlueSafe-stained SDS-PAGE gels of purified recombinant human CDR2 and DLIC1 fragments after SEC. DLIC1-C corresponds to residues 388-523. The elution profile and gel for CDR2 are shown on both left and right to facilitate comparison between wild-type DLIC1-C and the F447A/F448A mutant. Molecular weight is indicated in kDa.

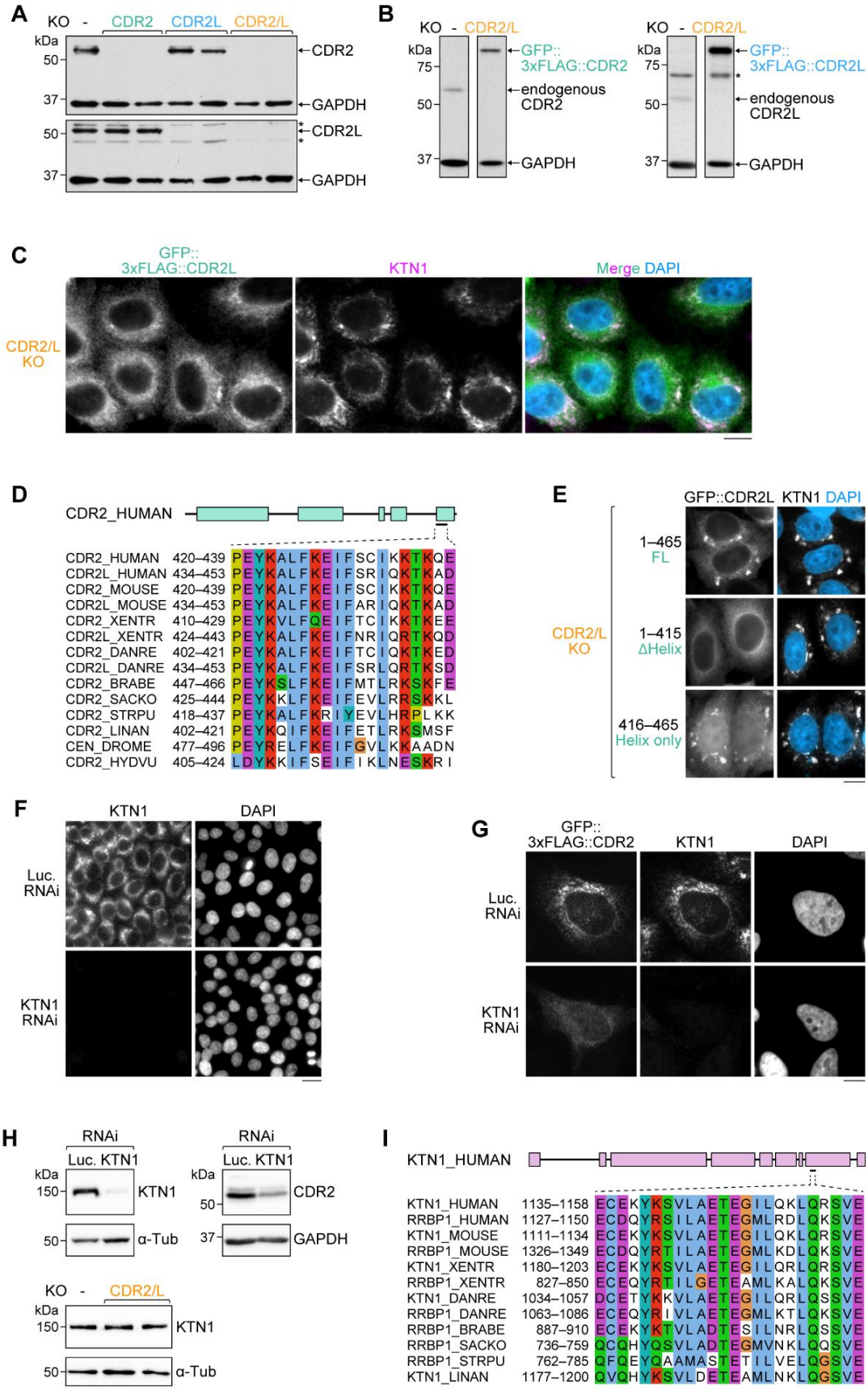

Figure S2 – Related to Figure 8 (generation of KO cell lines, CDR2L localization, sequence alignments of CDR2/CDR2L's C-terminal helix and its binding site in KTN1/p180, and decreased stability of CDR2 after KTN1 knockdown). *(continued on the next page)*

Figure S2 *(continued)* – Related to Figure 8 (generation of KO cell lines, CDR2L localization, sequence alignments of CDR2/CDR2L's C-terminal helix and its binding site in KTN1/p180, and decreased stability of CDR2 after KTN1 knockdown).

(A) Immunoblots of HeLa cells harboring single and double KOs of CDR2 and CDR2L. Two independently derived cell lines were analyzed for each condition. GAPDH serves as the loading control. Molecular weight is indicated in kDa. **(B)** Immunoblots of CDR2/L double KO cells stably expressing GFP::3xFLAG::CDR2 or CDR2L, used for the experiments in *Figure 7A*. GAPDH serves as the loading control. Molecular weight is indicated in kDa. **(C)** Immunofluorescence of CDR2/L double KO cells stably expressing GFP::3xFLAG::CDR2L, showing co-localization with KTN1 and diffuse cytoplasmic signal. Note that while average expression levels of transgene-encoded CDR2L are significantly higher than those of endogenous CDR2L, as shown in *(B)*, expression in individual cells is variable. The cells shown here have relatively low expression levels. Scale bar, 10 µm. **(D)** Sequence alignment of the C-terminal helix in CDR2 and CDR2L proteins from different species. Accession numbers and species key as in *Figure 13B*. **(E)** Immunofluorescence images of CDR2/L double KO cells transiently expressing full-length (FL) GFP::CDR2L, GFP::CDR2L without its C-terminal helix, or the GFP-tagged C-terminal helix on its own, showing that the C-terminal helix is necessary and sufficient for co-localization with KTN1. Scale bar, 10 µm. **(F)–(H)** Immunofluorescence images and immunoblots showing knockdown of KTN1 by RNAi and the resulting delocalization/destabilization of CDR2 in HeLa cells. By contrast, KTN1 levels remain unaffected in CDR2/L double KO cells (two independently derived KO cell lines were analyzed). Scale bars, 20 µm *(F)* and 10 µm *(G)*. Molecular weight is indicated in kDa. α-Tubulin (Tub) and GAPDH serve as loading controls. **(I)** Sequence alignment of the CDR2/eEF1Bβ binding site in KTN1 and its paralog RRBP1 (p180) from different species (invertebrates possess a single KTN1/RRBP1 homolog). Accession numbers: KTN1_HUMAN (UniProt Q86UP2), RRBP1_HUMAN (Q9P2E9), KTN1_MOUSE (UniProt Q61595), RRBP1_MOUSE (UniProt Q99PL5), KTN1_XENTR (UniProt B3DL66), RRBP1_XENTR (UniProt F7A6K6), KTN1_DANRE (UniProt E7F049), RRBP1_DANRE (UniProt B8A4D7), RRBP1_BRABE (UniProt A0A6P5A3T7), RRBP1_SACKO (NCBI Reference Sequence XP_002741373.1), RRBP1_STRPU (A0A7M7LVI4), KTN1_LINAN (NCBI Reference Sequence XP_013397491.1). Species key as in Figure S1B. No CDR2 binding site could be identified for the KTN1/RRBP1 homologs of DROME and HYDVU (UniProt Q960Y8 and T2M451, respectively), despite the presence of a well-conserved CDR2 helix, as shown in *(D)*.

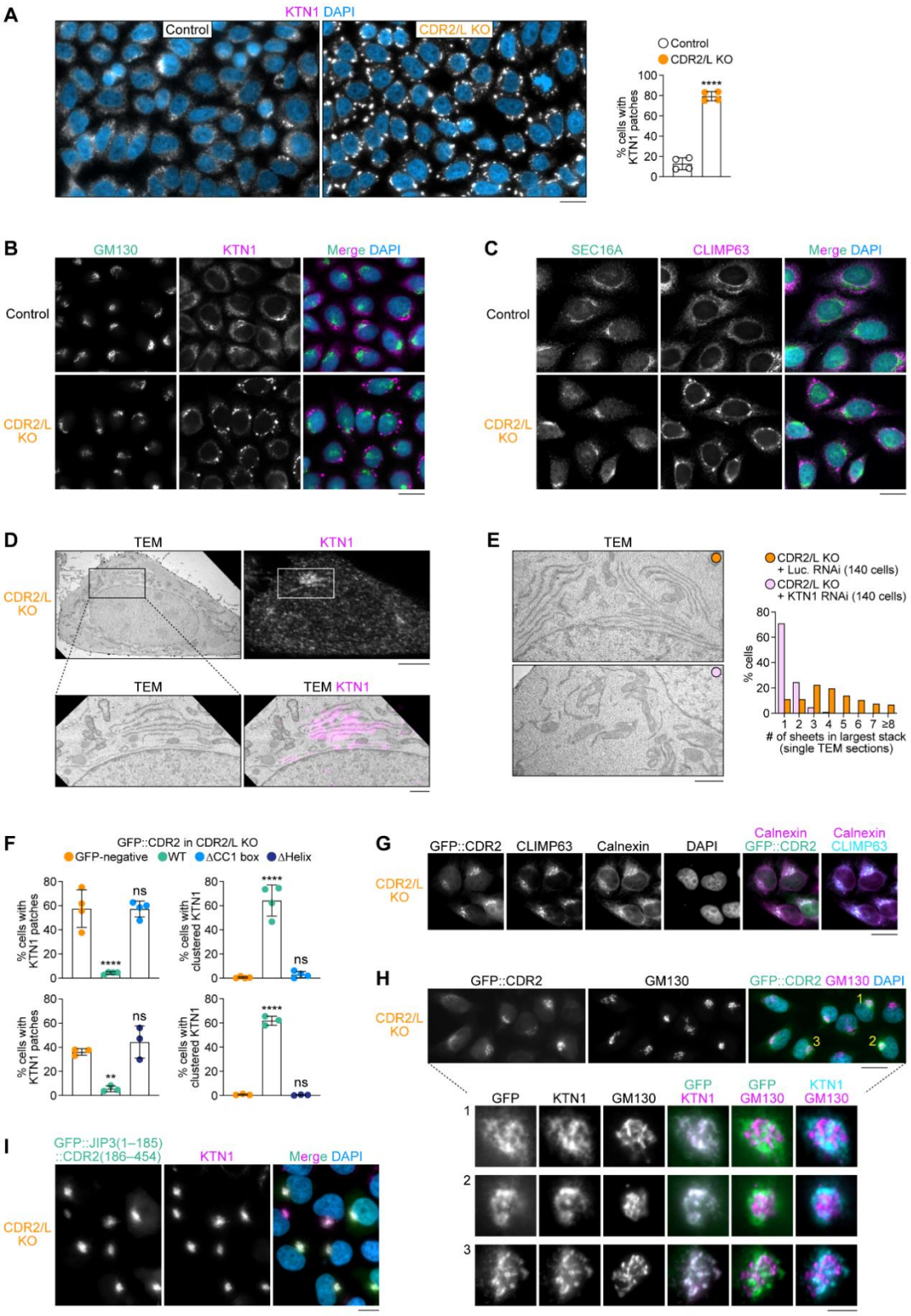

Figure S3 – Related to Figure 9 (characterization of ER organization in CDR2/L double KO cells). *(continued on the next page).*

Figure S3 *(continued)* – Related to Figure 9 (characterization of ER organization in CDR2/L double KO cells).

(A) *(left)* Immunofluorescence images showing exacerbated patchy distribution of KTN1 in HeLa CDR2/L double KO cells. Scale bar, 20 µm. *(right)* Fraction of cells with prominent KTN1 patches, plotted as mean ± SD (4 independent experiments, >1000 cells scored in total per condition). Statistical significance was determined using a two-tailed t test. ****$P < 0.0001$. These cells were treated with siRNA against Luciferase, which further enhances KTN1 patch formation in CDR2/L double KO cells relative to untreated cells (compare with quantification in *Figure 8A*). **(B), (C)** Immunofluorescence images showing unaltered distribution of the Golgi apparatus *(B)* and ER exit sites *(C)* in CDR2/L double KO cells. Scale bars, 20 µm. **(D)** Correlative light–electron microscopy images of CDR2/L double KO cells showing that the KTN1 patches observed by immunofluorescence correspond to stacked ER sheets. Scale bars, 5 µm *(top)* and 1 µm *(bottom)*. **(E)** *(left)* TEM images of ER sheets in CDR2/L double KO cells with and without knockdown of KTN1. Scale bar, 1 µm. *(right)* Number of ER sheets in the largest stack per cell, determined as described in *Figure 8B*. The CDR2/L double KO data is the same as in *Figure 8B*. **(F)** Fraction of cells (mean ± SD, 4 and 3 independent experiments for ΔCC1 box and ΔHelix, respectively; > 580 cells scored in total per condition) with prominent KTN1 patches *(left)* or centrosome-proximal KTN1 clustering *(right)* in the conditions shown in *Figure 8E*, using a second independently derived CDR2/L double KO cell line. ΔCC1 box and ΔHelix experiments each have their own WT and GFP-negative controls. Statistical significance was determined using ordinary one-way ANOVA followed by Tukey's multiple comparisons test. ****$P < 0.0001$; **$P < 0.01$; *ns* = not significant, $P > 0.05$. **(G)** Immunofluorescence images showing centrosome-proximal clustering of Calnexin and CLIMP63 in CDR2/L double KO cells transiently expressing GFP::CDR2. Scale bar, 20 µm. **(H)** Immunofluorescence images showing that centrosome-proximal GFP::CDR2 and KTN1 signals are distinct from that of the Golgi apparatus marker GM130. Scale bar, 20 µm. **(I)** Immunofluorescence image showing penetrant and tight clustering of KTN1 in the presence of JIP3(1–185)::CDR2(186–454). Scale bar, 10 µm.

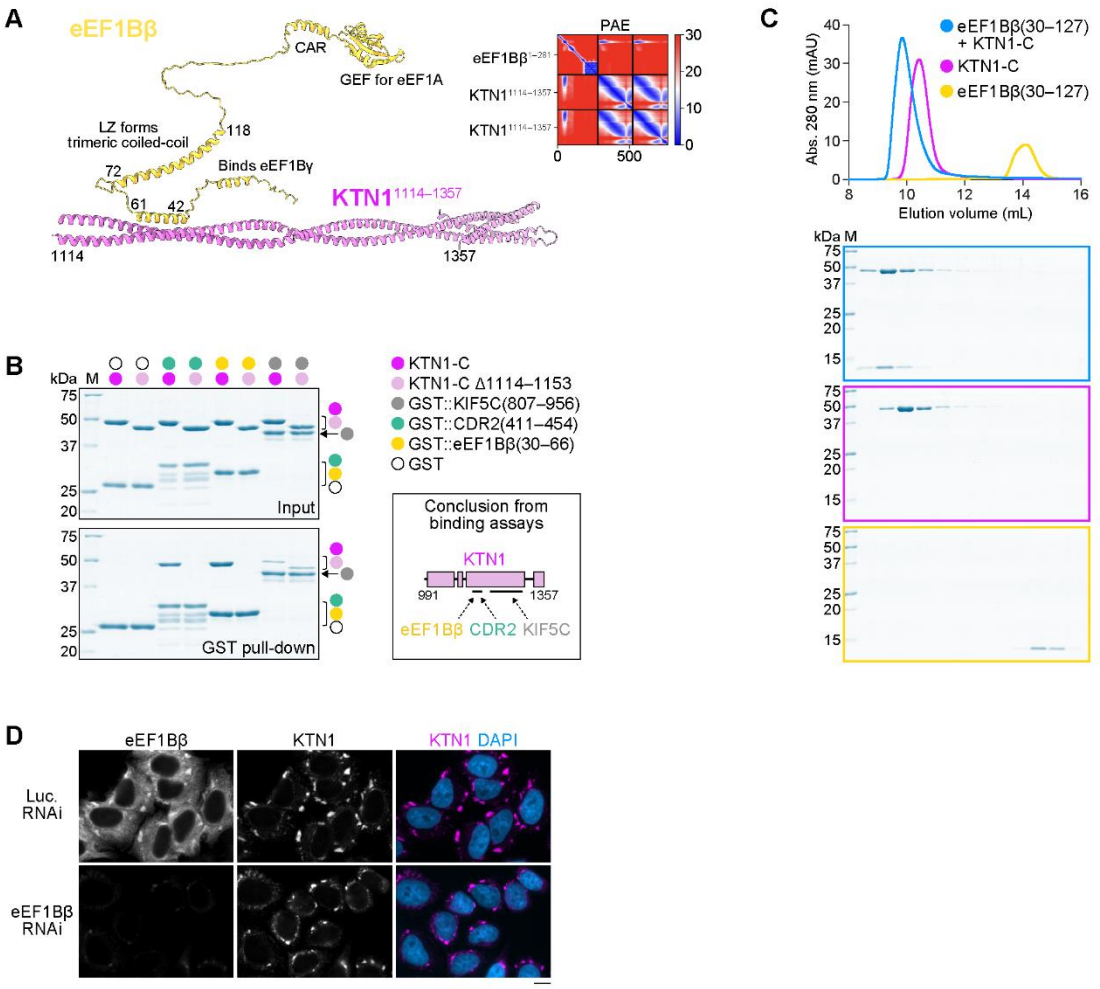

Figure S4 – Related to Figures 11 and 12 (eEF1Bβ's interaction with KTN1).

(A) AF2 model and PAE plot of full-length eEF1Bβ in complex with the KTN1 C-terminus. One copy of eEF1Bβ was used for the prediction, but note that eEF1Bβ can form a trimer through its LZ domain (Bondarchuk *et al.*, 2022). **(B)** BlueSafe-stained SDS-PAGE gels of purified recombinant proteins prior to addition of glutathione agarose resin (Input) and after elution from the resin (GST pull-down), showing that the binding site of KIF5C on KTN1 is distinct from that of CDR2/eEF1Bβ. Schematic summarizes the results of binding assays. Dotted line indicates the KIF5C binding site on KTN1 mapped by Ong *et al.* (2000). **(C)** Elution profiles and BlueSafe-stained SDS-PAGE gels of purified recombinant human eEF1Bβ and KTN1 fragments after SEC. eEF1Bβ(30–127) was used for the competition experiments of *Figure 11C*. Molecular weight is indicated in kDa. (D) Immunofluorescence images (maximum intensity projection of z-stack) showing that eEF1Bβ knockdown in CDR2/L double KO cells does not alter KTN1 distribution (see corresponding quantification in *Figure 12C*). Scale bar, 10 µm.

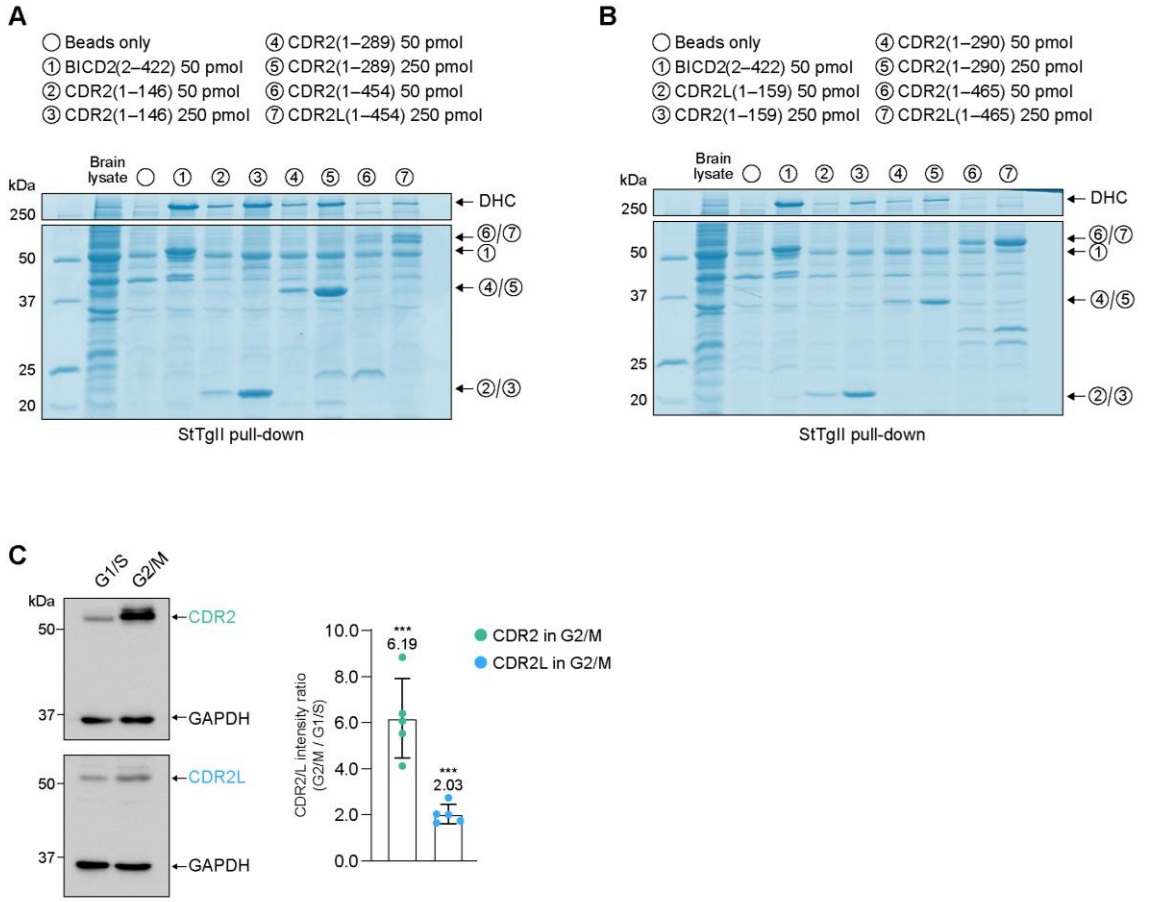

Figure S5 – Full-length CDR2 and CDR2L constructs are less efficient at pulling down DHC, and CDR2/L are more highly expressed in mitosis (related to *Discussion* section).

(A), (B) StTgII pull-downs from brain lysates using different amounts (50 and 250 pmol) and truncations of *(A)* CDR2 and *(B)* CDR2L constructs, stained with BlueSafe. Full-length constructs (samples 6–7) show reduced DHC pull-down compared to shorter truncations (samples 2–5) and to control (sample 1). BICD2(2–422) was used as a positive control. **(C)** *(left)* Immunoblot of control cells synchronized at the G1/S boundary using a double thymidine block, or at G2/M using nocodazole treatment following thymidine synchronization. *(right)* Quantification of CDR2 and CDR2L levels (mean ± SD, 4 independent experiments), normalized to GAPDH. Data were plotted as the ratio of CDR2/L band intensities in G2/M *vs.* G1/S. Statistical significance was determined using a two-tailed t-test. ***P < 0.0007.

Table S1 – Dynein, dynactin, and kinesin-1 subunits co-purifying with CDR2(1–146)::StTgII from pig brain lysates (Related to *Discussion* section).

Elution of StTgII pulldowns from pig brain lysates were subjected to mass spectrometry. Listed are subunits of the dynein, dynactin, and kinesin-1 complexes identified in the eluates.

Subunit	Coverage (%)	Nr of unique peptides	Abundance ratio (relative to control IP)
Dynein			
DHC	66	260	24
DIC1	63	27	14
DIC2	71	24	25
DLIC1	64	28	25
DLIC2	62	20	27
DLC1	49	3	26
DLC2	38	4	17
DLC RobI	83	7	18
DLC Tctex	80	5	19
Dynactin			
p150	55	49	3
p62	55	15	4
p50	65	17	5
p27	9	2	3
p25	49	5	4
p24	41	5	4
CapZA	59	10	2
CapZB	65	16	7
ARP10	35	9	3
Kinesin-1			
KIF5A	25	9	4
KIF5B	52	32	18
KIF5C	55	35	17
KLC1	59	22	20
KLC2	57	26	47

Table S2 – Most enriched proteins in immunoprecipitations from cells expressing GFP::3xFLAG::CDR2 or GFP::3xFLAG::CDR2L, identified by mass spectrometry in two experimental replicates (related to *Discussion* section).

Cells expressing GFP::3xFLAG-tagged CDR2 or CDR2L were used for affinity purification followed by mass spectrometry. Proteins are ordered from most to least abundant according to the mean abundance ratio of experiments 1 and 2. Only proteins consistently detected in both replicates were considered. KTN1 and p180 are highlighted in pink, and ribosomal proteins are highlighted in yellow.

Protein	Coverage (%)		Nr of unique peptides		Abundance ratio (relative to control IP)	
	Exp1	Exp2	Exp1	Exp2	Exp1	Exp2
GFP::3xFLAG::CDR2						
KTN1	55	61	67	77	25	23
RPL7	52	57	15	19	3	3
RPL7A	42	44	13	15	3	3
CKAP5	19	10	28	15	3	3
GCN1	22	18	43	36	2	3
RPL4	47	55	26	30	2	3
RPL6	48	55	14	25	2	3
RPS9	39	51	12	19	2	3
RPS2	72	57	10	20	3	2
HNRNPM	58	63	33	36	3	2
DSP	35	26	83	63	3	2
CHD4	18	14	27	15	3	2
RPL3	47	58	16	25	2	2
AIMP1	71	71	17	19	2	2
PARP1	21	19	17	15	2	2
SRRM2	20	22	34	40	3	2
GFP::3xFLAG::CDR2L						
PSME3	72	74	19	20	19	65
RRBP1/p180	36	38	43	47	20	10
YWHAQ	65	72	12	16	6	16
YWHAE	78	88	21	36	7	14
KTN1	55	61	67	77	12	7
YWHAZ	70	80	19	24	5	12
YWHAH	68	73	13	18	4	12
YWHAB	67	72	12	14	5	11
YWHAG	69	84	12	19	5	10
DAPK1	29	34	29	36	6	4
KRT1	92	62	112	36	2	6
KRT9	57	73	27	36	0.3	7
KRT10	58	51	23	21	0.63	4